Óbuda University

PhD Thesis

Model-based investigation of physiological systems and signals

by
Máté Siket

Supervisors:
Dr. György Eigner
Prof. Dr. Levente Kovács

Applied Informatics and Applied Mathematics Doctoral School
Budapest, 2023

Contents

List of Figures

List of abbreviations

Abbreviation	**Meaning**
MHE	Moving Horizon Estimation
IVP	Identifiable Virtual Patient
MPC	Model Predictive Control
BG	Blood glucose
KF	Kalman filter
NSMO	Nonlinear sliding mode observer
EGP	endogenous glucose production
LPV	Linear Parameter Varying
LHS	Latin Hypercube Sampling
NRMSE	Normalized root-mean-square error
CGMS	Continuous Glucose Monitoring System
CHO	Carbohydrate
LSCI	Laser Speckle Contrast Imaging
TVI	Time varied illumination
CW	Continuous wave
ROI	Region of interest

1

Introduction

> Every theory of the course of events in nature is necessarily based on some process of simplification of the phenomena and is to some extent therefore a fairy tale.
>
> *Sir Napier Shaw: Manual of Meteorology: I, 123.*

Complexity and diversity of biological processes can be inspirational and daunting at the same time. During my studies I had the opportunity to delve deeper into two tasks, which are both connected to physiological signals and have their merits on their own. First, I will introduce the two larger topics of my dissertation and since they may seem as a bit distant scientific fields, I also wish to highlight the common threads that run along them. The beauty of mathematical modeling is that describing the dynamics of the blood glucose level and fitting models of laser speckle contrast imaging require very similar set of tools and methods. Throughout the different physiological processes, I was mainly dealing with model creation, parameter estimation and what surrounds these topics: identifiability, parameter sensitivity, signal processing and optimization. First part of my dissertation describes my research related to providing better personalizations in diabetes therapy and explaining patient dynamics with a focus on simpler mathematical models. In the second part, I aimed to extend the current mathematical models of laser speckle imaging and improve the method through various optimizations.

Diabetes is a chronic disease that is estimated to affect 537 millions of people worldwide [R1]. Type 1 diabetes is a specifically dangerous form of the disease, since the ceasing of insulin hormone production requires a constant exogenous insulin intake. The constant insulin is needed to keep the patient's blood glucose level in a healthy range; without it, the insulin dependent cells cannot withdraw glucose from the plasma, and the high blood glucose level (hyperglycemia) leads to various physiological complications such as retinopathy, nephropathy, neuropathy, macrovascular complications [R2]. Also, insulin cannot be injected or infused arbitrarily as increased levels of plasma insulin can lead to low glucose values (hypoglycemia), which creates life-threatening condition by not providing fuel to the brain, whose main nutrition is glucose.

Type 1 diabetes management have come a long way since the invention of insulin [R3]. Insulin delivery moves from multiple daily injections to continuous infusion, from insulin pens to insulin pumps. Glucose measurement moves from intermittent sampling to continuous measurement, from finger prick to minimal invasive sensors. Lastly, but not least automated delivery systems gain popularity by utilizing the continuous manner both in the

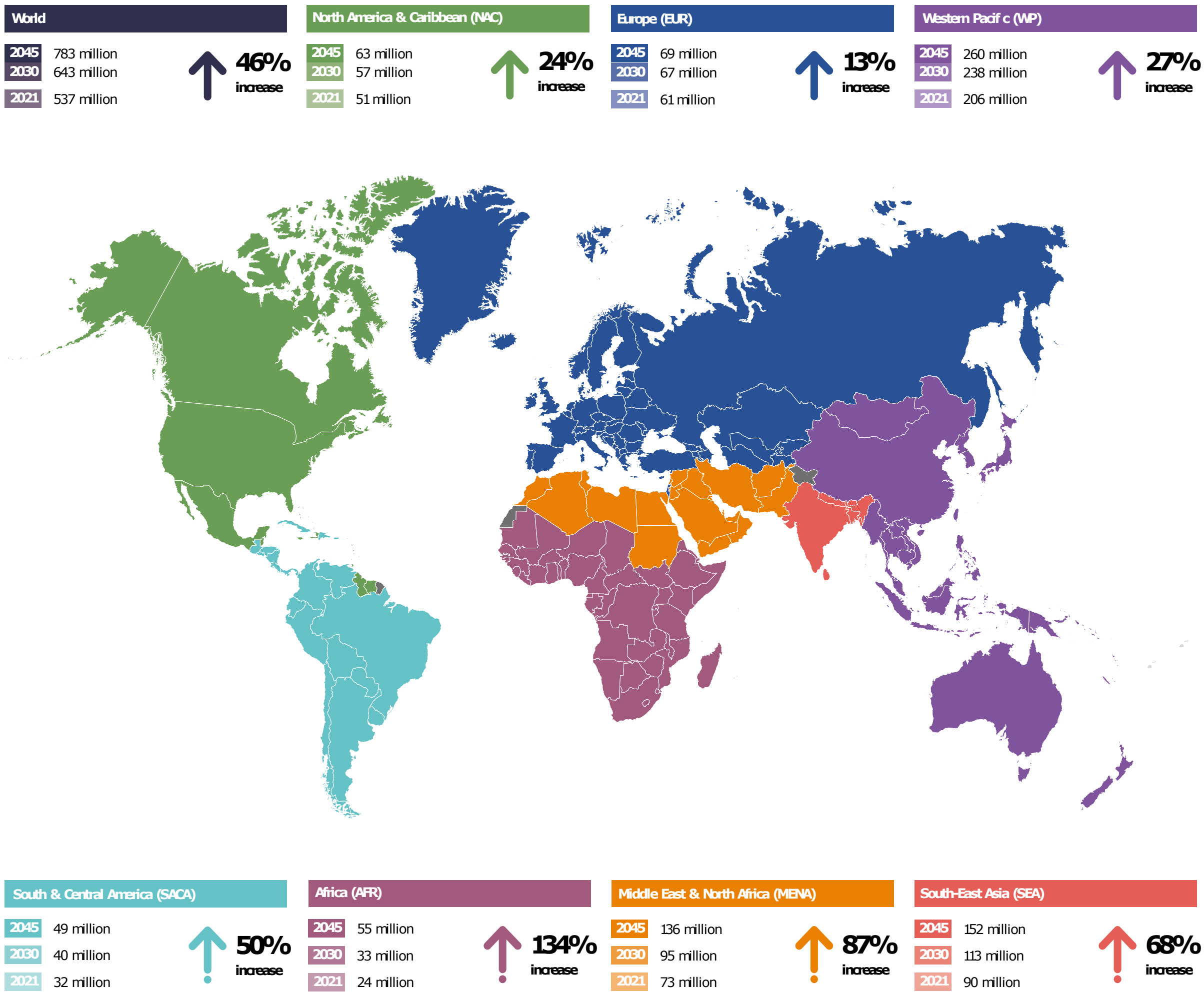

Figure 1.1: Number of people with diabetes worldwide and per IDF Region in 2021-2045 (20-79 years)[R1].

input and the measurement. An automated delivery system (or artificial pancreas) aims to alleviate the burden of constant monitoring and controlling of blood glucose by assigning the task to an algorithm. In the last decade or so four such systems got the approval of the Food and Drug Administration of the United States [R4, R5, R6, R7].

The control algorithms of automated insulin delivery systems take into account the past values of the blood glucose concentration, and try to calculate an insulin amount which will – based on the information the system has – keep the blood glucose in a healthy range. The calculation is a difficult task for several reasons, few important ones are as follows: 1) The algorithm has to face interpatient variability. (Physiology of the patients can differ greatly, making it difficult for a single algorithm to handle a heterogeneous group of people.) 2) Variability also occurs during the day, due to the circadian rhythm of the patient – usually referred to as intrapatient variability. 3) Carbohydrate intakes, physical activity, stress and such introduce disturbances which need a constant compensation. So that the algorithm could make informed decisions, one approach is to provide additional information about the dynamics of the patient and disturbances. My journey joins this path, where I started off with different Kalman filters for state and disturbance estimation; I continued my way through moving horizon estimation based methods. I relied heavily on optimization and applied various constraints to achieve better results without sacrificing on the altar of overparametrization. Usually model predictive controllers are considered as today's state-of-the-art algorithms; they can take into account constraints and provide good disturbance rejection [R8, R9]. Also, they can be fine-tuned to the patient by setting the parameters of the underlying mathematical model. This also means that usually the performance of the controller relies heavily on the accuracy of the parameters, which implies the requirement of accurate patient parameter estimation.

Laser speckle contrast imaging (LSCI) is situated on the other side of the medical workflow of diabetes; so far I described the tools that I investigated and related to diabetes treatment. On the other hand, LSCI is tied to the diagnosis part by the possibility to monitor microcirculation in diabetic feet. Diabetic foot ulcers are one of the main complications of diabetes. A significant factor in causing diabetic foot ulcers is the microvascular dysfunction which leads to impaired perfusion (ischemia). The early and accurate evaluation of the severity of the microcirculation deficiency is essential in clinical decision making. Current techniques lack the ability to quantify the severity of the ischemia and have poor prognostic values. There are studies suggesting that LSCI can be a method to quantify the ischemia in a diabetic foot in a non-invasive manner [R10, R11]. However, the technique have some shortcomings which I focused on in my research.

LSCI is a noninvasive imaging technique, and mainly used for generating blood flow or perfusion maps. The working principle is based on the interference pattern caused by the reflection of coherent light from a medium with static and dynamic scatterers. Scattering coherent light gets amplified and attenuated depending on the structure of the medium, which leads to a random pattern the so-called speckles. In the specific case when the reflective medium is completely static, the imaging device observes a frozen pattern of the so-called speckles. However, if motion occurs (e.g. blood flows) the pattern changes and decorrelates in time, and the exposed image turns out to be blurry. The local level of decorrelation (or blurriness) can be quantified by calculating the contrast in a region of interest. Carrying out the calculation using a sliding window results in a contrast map, which tells us about the relative flow speeds in vessels with various sizes, the progression of diabetes-induced vascular complications [R10] or regeneration of a burned tissue [R13, R14]. Disadvantages of the technique is the relatively low dynamic range, under- or overexposure can also greatly affect the observed contrast values.

During my studies I modeled different aspects of LSCI or aimed to improve the technique. In both cases my methodologies relied heavily on optimization, either to improve the dynamic range by optimizing the laser pulse sequence, or by validating the models when fitted to simulated and/or real world data. In summary, the recurring themes in my dissertation are model development, simulations and parameter estimation by using optimization methods.

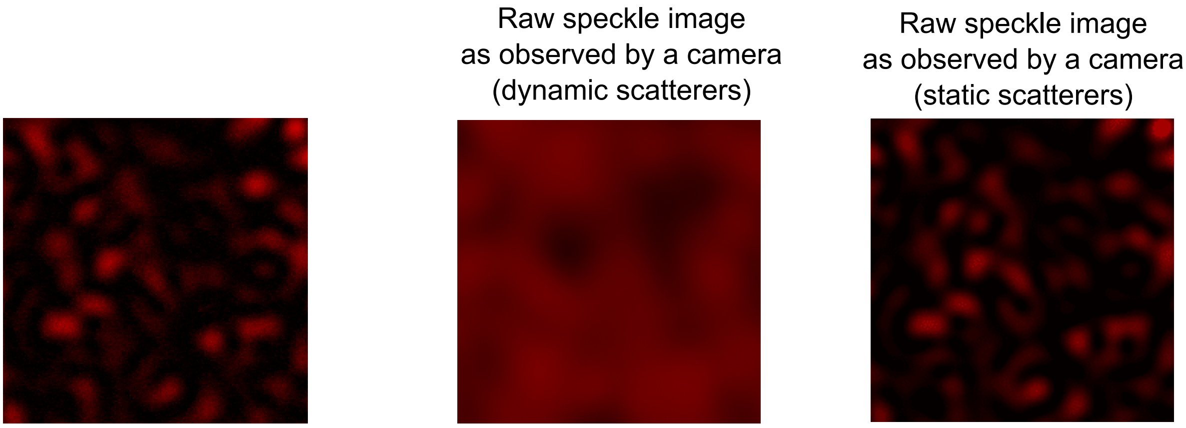

(a) Images of changing speckle patterns caused by dynamic scatterers.

(b) Exposed images of speckle patterns with finite exposure length.

Figure 1.2: Illustration of projected speckle patterns and exposed images with static and dynamic scatterers [R12].

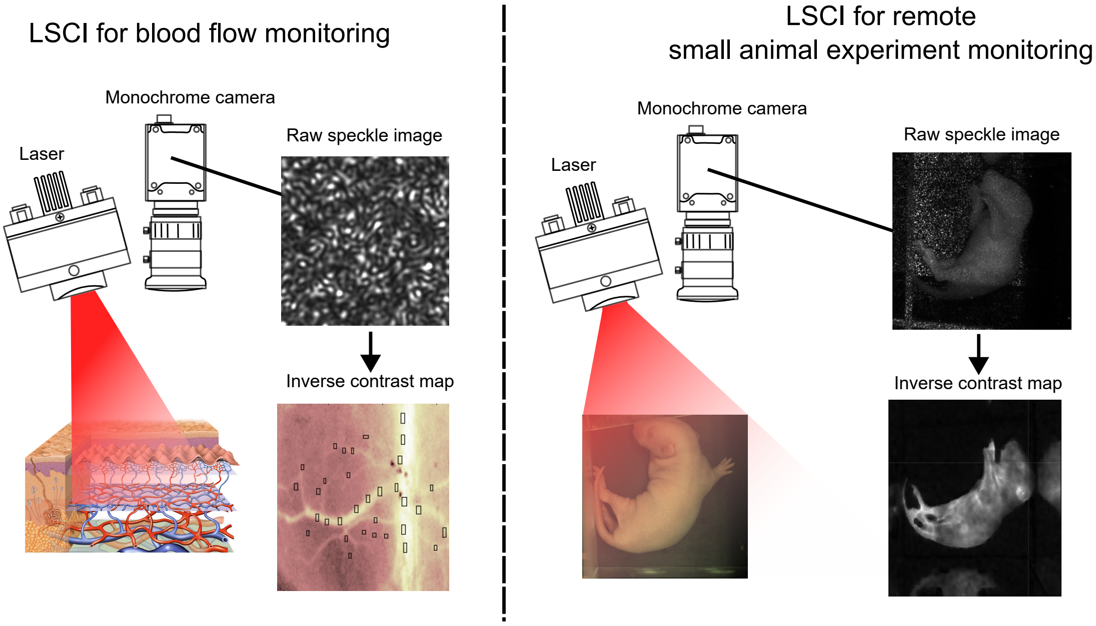

Figure 1.3: Application areas of LSCI. The raw speckle image for the blood flow monitoring is for illustration purposes [R15]. In the inverse contrast maps brighter pixels correspond to more movement/higher blood perfusion. On the left hand side the rectangles show vessels with different diameter and flow speed.

2

Kalman filter

Thesis group 1: State and disturbance estimation in Artificial Pancreas using Kalman filters

Thesis 1
I developed and investigated Kalman filters for state/parameter and disturbance estimation in Artificial Pancreas applications. My focus was on developing extended Kalman filters based on linear parameter varying methodology.

Thesis 1.1
I have developed Joint and Dual Kalman filters for state and disturbance estimation using linear parameter varying methodology. I analyzed different linear parameter varying discretization methods and scheduling parameter selections.

Thesis 1.2
I developed a Kalman filter tuning method to acquire consistent results and outcomes in the evaluated scenarios. I contributed to the comparison of the developed filters. The filters were compared across different models, estimated variables and to a sliding mode observer.

Publications relevant to the theses: [C1, C2, J1, J2].

2.1 Introduction

A major hurdle in artificial pancreas applications is data scarcity. In practice, the typically utilized information is the Continuous Glucose Monitoring Sensor (CGMS) measurements and demographic data such as body weight. As the physiology and processes of a human organism is a complex system – a network of multitudinous interconnected subsystems – it is cumbersome to describe them with a limited number of measurable variables. The most well-known of the observers in the field are the different realizations of the Kalman filter (KF) [R16]; their performance is evaluated on different terms (general, fault detection, insulin estimation) in [R17, R18, R19], respectively. A crucial element in the observer design is the model. The medium-complexity Hovorka model [R20] has been widely used to design observers for glucose control [R21, R22]. However, its large number of parameters could complicate model identification and observer tuning. For this reason, the use of simpler models might be desirable. Extensions of the Bergman's minimal model [R23], such as the Identifiable Virtual Patient model (IVP) [R24] might be an appealing option in this regard, as shown in [R25] and [R18]. Necessarily, a price to pay for model simplification is a loss of accuracy in modelling certain physiological behaviours. For example, while renal glucose clearance is considered in the Hovorka model, the IVP does not.

One goal of this research was to determine how the model complexity affects the performance of the observer. To this end, the well-accepted Hovorka model in [R20] was compared to IVP presented in [R24].

2.2 Investigated models

2.2.1 Identifiable Virtual Patient Model

The IVP model [R24] is a compromise between Bergman's model [R23] and the Hovorka model regarding structural complexity and accuracy. Its equations are described below:

$$\dot{I}_{SC}(t) = -\frac{1}{\tau_1} \cdot I_{SC}(t) + \frac{1}{\tau_1 C_I} \cdot u(t) \tag{2.1}$$

$$\dot{I}_{P}(t) = -\frac{1}{\tau_2} \cdot I_{P}(t) + \frac{1}{\tau_2} \cdot I_{SC}(t) \tag{2.2}$$

$$\dot{I}_{EFF}(t) = -p_2 \cdot I_{EFF}(t) + p_2 \cdot S_I \cdot I_P(t) \tag{2.3}$$

$$\begin{aligned}\dot{G}(t) = &-(GEZI + I_{EFF}(t)) \cdot G(t) + \\ &+ EPG + R_A(t)\end{aligned} \tag{2.4}$$

where $I_{SC}(t)$ and $I_P(t)$ represent the subcutaneous and plasma insulin concentrations $(\mathrm{mU/L})$, respectively. $I_{EFF}(t)$ is the insulin effect $\left(\mathrm{min}^{-1}\right)$ and $G(t)$ is the plasma glucose concentration $(\mathrm{mg/dL})$. The inputs of the model are the subcutaneous insulin infusion $u(t)$ $(\mu\mathrm{U/min})$, and the rate of glucose appearance $R_A(t)$ $(\mathrm{mg/dL/min})$ from the meal absorption. Note that the $R_A(t)$ is generally unknown due to the complexity of meal absorption dynamics, influencing factors like nutritional composition and alcohol intake. Hence, the $R_A(t)$ will be estimated in this work. Lastly, τ_1 and τ_2 (min) refer to the insulin absorption time constants, p_2 is the kinetic rate for insulin action $\left(\mathrm{min}^{-1}\right)$, S_I is the insulin sensitivity $(\mathrm{mL}/\mu\mathrm{U/min})$, EGP is the hepatic glucose production, $GEZI$ is the glucose effectiveness at zero insulin $\left(\mathrm{min}^{-1}\right)$ and C_I denotes the insulin clearance $(\mathrm{mL/min})$.

2.2.2 Hovorka model

The Hovorka or Cambridge model is considered a medium complexity model by the artificial pancreas scientific community. The model consists of 8 dynamic states and a couple of additional algebraic equations if the carbohydrate absorption sub-model is lumped, and replaced with the $R_A(t)$ term, as in the IVP model previously described. The dynamic equations are given by [R20]:

$$\begin{aligned}
\dot{Q}_1(t) &= -F_{01c}(t) - F_R(t) - x_1(t)Q_1(t) + k_{12}Q_2(t) \\
&\quad + EGP_0(1 - x_3(t)) + R_A(t),
\end{aligned} \tag{2.5}$$

$$\dot{Q}_2(t) = Q_1(t)x_1(t) - (k_{12} + x_2(t))Q_2(t), \tag{2.6}$$

$$\dot{I}(t) = \frac{S_2(t)}{\tau_S V_I} - k_e I(t), \tag{2.7}$$

$$\dot{x}_1(t) = -k_{a1}x_1(t) + k_{b1}I(t), \tag{2.8}$$

$$\dot{x}_2(t) = -k_{a2}x_2(t) + k_{b2}I(t), \tag{2.9}$$

$$\dot{x}_3(t) = -k_{a3}x_3(t) + k_{b3}I(t), \tag{2.10}$$

$$\dot{S}_1(t) = u(t) - \frac{S_1(t)}{\tau_S}, \tag{2.11}$$

$$\dot{S}_2(t) = \frac{S_1(t)}{\tau_S} - \frac{S_2(t)}{\tau_S}, \tag{2.12}$$

where $Q_1(t)$ $(\mathrm{mmol/kg})$ is the glucose content in the accessible compartment, $Q_2(t)$ $(\mathrm{mmol/kg})$ is the glucose content in the non-accessible compartment, $R_A(t)$ $(\mathrm{mmol/kg/min})$ is the rate of glucose appearance, $I(t)$ $(\mathrm{mU/L})$ is the plasma insulin concentration. $x_1(t)$ $\left(\mathrm{min}^{-1}\right)$ is the remote effect of insulin on glucose distribution, $x_2(t)$ $\left(\mathrm{min}^{-1}\right)$ is the remote effect of insulin on glucose disposal, $x_3(t)$ (1) is the remote effect of insulin on endogenous glucose production in the liver. $S_1(t)$ $(\mathrm{mU/kg})$ is the insulin in the accessible compartment and $S_2(t)$ $(\mathrm{mU/kg})$ is the insulin in the non-accessible compartment. Input of the system $u(t)$ $(\mathrm{mU/kg/min})$ is the insulin infusion. The parameters: k_{12} $\left(\mathrm{min}^{-1}\right)$ is the transfer rate from the non-accessible compartment to the accessible, EGP_0 $(\mathrm{mmol/kg/min})$ is the endogenous glucose production in case of zero insulin level, k_e $\left(\mathrm{min}^{-1}\right)$ is the insulin clearance. The patient's insulin sensitivities on transport, disposal and, glucose production are determined by the $k_{a1,2,3}$ $\left(\mathrm{min}^{-1}\right)$ and $k_{b1,2}$ $(\mathrm{L/mU/min/min})$, k_{b3} $(\mathrm{L/mU/min})$ parameters. The insulin absorption time constant is denoted by τ_S (min) [R20].

Supplementary algebraic equations are defined by:

$$F_{01c}(t) = \begin{cases} F_{01}, & \text{if } G(t) \geq 4.5 \text{ mmol/L} \\ F_{01}G(t)/4.5, & \text{otherwise} \end{cases}, \tag{2.13}$$

$$F_R(t) = \begin{cases} 0.003V_G(G(t) - 9), & \text{if } G(t) \geq 9 \text{ mmol/L} \\ 0, & \text{otherwise} \end{cases}, \tag{2.14}$$

$$G(t) = \frac{Q_1(t)}{V_G}, \tag{2.15}$$

where F_{01c} $(\mathrm{mmol/kg/min})$ is the glucose consumption of the central nervous system, while F_{01} represents the consumption at ambient glucose concentration, F_R $(\mathrm{mmol/kg/min})$ is the renal excretion of glucose in the kidneys, $G(t)$ $(\mathrm{mmol/L})$ is the actual output of the system: blood glucose concentration, V_G $(\mathrm{L/kg})$ is the glucose distribution volume [R20].

The units of the models can be converted in the following way: $1\,(\mathrm{mmol/L}) = 18\,(\mathrm{mg/dL})$ for the blood glucose level, $1\,(\mathrm{mmol/kg/min}) = 180/V_g\,(\mathrm{mg/dL/min})$ for the rate of appearance, where $V_g(\mathrm{dL/kg})$ is the glucose distribution volume. The conversion between the insulin infusion is $1\,(\mathrm{mU/kg/min}) = 1000/BW\,(\mu\mathrm{U/min})$, where $BW\,(\mathrm{kg})$ is the body weight. Note that the IVP model expresses the variables relative to the volumes, while the Hovorka model, relative to the body weight.

The UVa-Padova simulator was selected to identify the models. The simulator received the approval of the Food and Drug Administration to be used as a substitute for preclinical trials with animals [R26]. Also, the simulator model could fit glucose profiles from clinical data [R27], and its meal model reconstructed the R_A with more accuracy than other models in the literature [R28]. Finally, it includes a realistic cohort of virtual subjects [R29].

We identified two parameter sets: a population value parameter set (or average model) and individualized parameter set. The population value parameter set was determined from the average subject in the simulator. The individualized parameter sets were obtained by identifying two of the most sensitive parameters for each of the 10 individuals in the adult cohort (of the academic version of the simulator), while the remaining parameters were set to their corresponding values in the average model. The identification procedure followed the pathway of [R30]: checking the structural identifiability, ranking the sensitive parameters, and identifying the parameters.

2.3 Methods

2.3.1 Identifiability analysis

Structural identifiability defines the possibility of determining under ideal conditions (e.g. absence of noise) a unique value (structurally globally identifiable) or a finite set of values (structurally locally identifiable) for model unknown parameters, with the only information of the inputs and outputs [R31]. To analyse the structural identifiability, the generating series approach was used since it is a trade-off method between computational cost and provided information regarding other techniques in the literature [R31]. The analysis was performed with the GenSSI 2.0 software described in [R32].

The inputs considered in the identifiability analysis were the insulin infusion and R_A. Since the R_A was available for the identification, parameters related to the carbohydrate absorption dynamics – the glucose distribution volume in the IVP model [R24] and the parameters D_G (amount of carbohydrates digested), A_G (carbohydrate bioavailability), t_{maxG} (maximum time for the rate of glucose appearance) in the Hovorka model [R20] – were excluded from the analysis. In addition, the weight BW in the Hovorka model is known, thus it was neither considered in the identification.

2.3.2 Sensitivity analysis

A global sensitivity analysis was performed with a twofold purpose: 1) to reduce the number of parameters to be identified in the Hovorka average model, and 2) to select the two parameters to be individualized in the personalized IVP and Hovorka models. The same parameters included in the identifiability analysis were considered in the sensitivity analysis.

For the sensitivity analysis, the AMIGO2 Matlab toolbox was utilized [R33]. The sensitivity is calculated by changing the parameters which result in various trajectories. Different measures can be applied to these trajectories, the most common ones are the root-mean-square deviation and the mean absolute deviation. In order to get a more robust result, several steps were taken. The simulations of the trajectories were repeated with different initial conditions or input schemes. The sensitivity values were normalized at each time instance for all the parameters. The toolbox utilized the Latin Hypercube Sampling (LHS). The LHS method provides an even distribution of all the parameters in the given range, with a relatively low amount of necessary samples. The parameter bounds were calculated by applying to the nominal values in [R34] and [R24] a deviation of $\pm 5\sigma$, where σ denotes the standard deviation provided in the referred articles, but saturating to 0 if negative values appeared. The simulation of a given parameter set was only considered in the calculation of the sensitivity if the BG remained in the following range: $1.8 < BG < 25$ mmol/L in order to avoid entirely unrealistic trajectories.

If a general nonlinear system is defined in the form of $0 = f(\dot{x}, x, p, u, t)$, where p are the parameters, then the sensitivities $s_p = \frac{\partial x}{\partial p}$ can be given with the Jacobians: $\frac{\partial s_p}{\partial t} = \frac{\partial f}{\partial x} s_p + \frac{\partial f}{\partial p}$ s.t. $s_p(0) = 0$.

The toolbox normalizes with the value of the parameter and with the value of the output in the given discrete step:

$$S_{p,k} = \frac{p_i}{y(k)} s_{p,k} \tag{2.16}$$

where $S_{p,k}$ is the normalized or relative sensitivity of the parameter p in the $k-th$ discrete step, $y(k)$ is the output and p_i is the $i-th$ sample from the LHS. The ranking of the parameters is based on the final measure defined by:

$$\delta_p^{msqr} = \frac{1}{n_e n_{lhs} n_k} \sqrt{\sum_{e=1}^{n_e} \sum_{i=1}^{n_{lhs}} \sum_{k=1}^{n_k} (S_{p,k})^2} \tag{2.17}$$

where n_e is the number of different setups for experiments (initial conditions or input schemes), n_{lhs} is the number of sampled values of the parameters, n_k is the number of discrete points at which the system is evaluated.

2.3.3 Identification

On the one hand, in the identification of the average models, all the sensitive and mildly sensitive parameters were considered, as suggested in [R30]. The insensitive parameters were set to the nominal parameters in [R20] for the Hovorka model, and the means of the parameters listed in [R24] were considered for the IVP model. On the other hand, two parameters in the sensitive group were individualized for the personalized models. The remaining parameters were fixed to the corresponding values in the average model. To identify the Hovorka model, the parametrization of the model in terms of insulin sensitivities ($S_{i1} = k_{b1}/k_{a1}$, $S_{i2} = k_{b2}/k_{a2}$ and $S_{i3} = k_{b3}/k_{a3}$) was utilized as in [R20].

The identification consisted of two optimization problems: one that identifies insulin-related states by minimizing the normalized root-mean-square error (NRMSE) of the plasma insulin; and another one that identifies the insulin effect and glucose-related parameters by minimizing the NRMSE of the glucose measurement. The NRMSE is defined by:

$$NRMSE(x) = \sqrt{\frac{\sum_{i=1}^{N} (x_{model} - x_{UVa})^2}{N}} \cdot \frac{1}{x_{UVa}^{max} - x_{UVa}^{min}}, \tag{2.18}$$

where x_{model} represents the glucose or plasma insulin obtained by the IVP or Hovorka models. x_{UVa} denotes the “real" measurements, whereas the superscripts max and min refers to the maximum and minimum values of these measurements, respectively. This two-step optimization procedure targets a better identification of the insulin pharmacokinetics, as discussed in [R24]. The inputs to the optimization problem were the glucose, the plasma insulin, the insulin infusion, and the meal disturbance. We generated these inputs from a 3-meal simulation of the average adult patient (for average models) or the adult cohort (for personalized models). Of note, the full knowledge of these inputs is impractical for real applications, but they were used in this study to ensure accurate identification of the parameters.

The genetic algorithm in the Global Optimization Toolbox of Matlab 2018b (*ga* function) was utilized to solve the above-described optimization problem. The algorithm was configured with its default settings [R35].

Finally, the identification of the models was assessed in terms of the NRMSE using, as in the identification, a 3-meal scenario, but with different instances of variability.

2.3.4 Kalman filters

Besides the estimation of the state variables, our goal was to estimate the R_A as well. To do so in the case of KFs, the engineer has two main options. The most straightforward and largely applied technique is the augmentation of the state vector with the parameter or disturbance term, giving rise to the joint KF (JKF) [R36]. Another possibility is to use separate KF for the state and parameter/disturbance estimation problem; this observer is called the dual KF (DKF) [R36]. Both observers hypothesize that the parameters are static: in the prediction phase, the parameter in the next step holds the value of the previous step. For the application of the observers, the models are either discretized by the Euler or Complete method. In addition, the benefits of linear parameter varying (LPV) formulation were exploited in this article to handle non-linearities in KFs design. Consequently, more complex KF-based algorithms (such as Extended KF or Unscented KF) were avoided [R17].

LPV modeling technique is an approach to handle the nonlinearities of the given system. If one the parameters is not a free signal such as an inner state variable, then it is called quasi-LPV or qLPV. The continuous time qLPV state-space representation (qLPV-SS) is defined as follows [R37]:

$$\dot{\mathbf{x}}(t) = \mathbf{A}(\mathbf{p}(t))\mathbf{x}(t) + \mathbf{B}(\mathbf{p}(t))\mathbf{u}(t) \ , \tag{2.19a}$$

$$\mathbf{y}(t) = \mathbf{C}(\mathbf{p}(t))\mathbf{x}(t) + \mathbf{D}(\mathbf{p}(t))\mathbf{u}(t) \ , \tag{2.19b}$$

where the $\mathbf{p}(t) = [p_1(t) \dots p_R(t)]$ parameter vector consists of the so-called scheduling parameters $p_i(t)$. $\mathbf{p}(t) \in \mathbf{\Omega}^R \subset \mathbb{R}^R$ is an R-dimensional real vector within the set $\mathbf{\Omega} = [p_{1,min}, p_{1,max}] \times [p_{2,min}, p_{2,max}] \times \dots \times [p_{R,min}, p_{R,max}]$.

Either the IVP or the Hovorka model accept a qLPV-SS representation:

- **IVP model**. Selecting $\mathbf{p}(t) = G(t)$ as scheduling parameter leads to the following qLPV representation:

$$\mathbf{A}\big(p(t)\big) = \begin{bmatrix} -GEZI + \frac{EGP}{p(t)} & -p(t) & 0 & 0 & 1 \\ 0 & -p_2 & p_2 S_I & 0 & 0 \\ 0 & 0 & -\frac{1}{\tau_2} & \frac{1}{\tau_2} & 0 \\ 0 & 0 & 0 & -\frac{1}{\tau_1} & 0 \\ 0 & 0 & 0 & 0 & 0 \end{bmatrix}, \tag{2.20}$$

$$\mathbf{B} = \begin{bmatrix} 0 & 0 & 0 & \frac{1}{\tau_1 C_I} & 0 \end{bmatrix}^T, \tag{2.21}$$

$$\mathbf{C} = \begin{bmatrix} 1 & 0 & 0 & 0 & 0 \end{bmatrix}, \tag{2.22}$$

$$\mathbf{D} = [0], \tag{2.23}$$

where the additional 5th state variable is the estimated disturbance, namely the R_A:

- **Hovorka model**. Taking:

$$\mathbf{p}(t) = [\frac{EGP_0 - F_{01c}(t) - F_R(t)}{Q_1(t)}, Q_1(t), Q_2(t)]$$

the qLPV representation is as follows:

$$\mathbf{A}\big(\mathbf{p}(t)\big) = \begin{bmatrix} p_1(t) & k_{12} & 0 & -p_2(t) & 0 & -EGP_0 & 0 & 0 & 1 \\ 0 & -k_{12} & 0 & p_2(t) & -p_3(t) & 0 & 0 & 0 & 0 \\ 0 & 0 & -k_e & 0 & 0 & 0 & 0 & \frac{1}{\tau_S V_I} & 0 \\ 0 & 0 & k_{b1} & -k_{a1} & 0 & 0 & 0 & 0 & 0 \\ 0 & 0 & k_{b2} & 0 & -k_{a2} & 0 & 0 & 0 & 0 \\ 0 & 0 & k_{b1} & 0 & 0 & -k_{a3} & 0 & 0 & 0 \\ 0 & 0 & 0 & 0 & 0 & 0 & -\frac{1}{\tau_S} & 0 & 0 \\ 0 & 0 & 0 & 0 & 0 & 0 & \frac{1}{\tau_S} & -\frac{1}{\tau_S} & 0 \\ 0 & 0 & 0 & 0 & 0 & 0 & 0 & 0 & 0 \end{bmatrix}, \tag{2.24}$$

$$\mathbf{B} = \begin{bmatrix} 0 & 0 & 0 & 0 & 0 & 0 & 1 & 0 & 0 \end{bmatrix}^T, \tag{2.25}$$

$$\mathbf{C} = \begin{bmatrix} \frac{1}{V_G} & 0 & 0 & 0 & 0 & 0 & 0 & 0 & 0 \end{bmatrix}, \tag{2.26}$$

$$\mathbf{D} = [0], \tag{2.27}$$

Since the selected parameters are not directly measurable, they have to be estimated by the observer and can introduce additional inaccuracies compared to an LPV model where the parameters are measurable. The additional 9th state variable is the estimated disturbance, namely the $R_A(t)$.

Utilizing the benefits of the discretized LPV representation, a linear discrete Kalman filter can be applied to the nonlinear system [R38, R39]. In the case of the JKF, the dimension of the covariance matrix is extended by the number of parameters. In this case, because of the supposition of the parameters, the exact discretization method cannot be applied. This is due to the arising singularity issue, thus explicit Euler method is applied:

$$\mathbf{A}\big[\mathbf{p}[k]\big] = \mathbf{I} + T_s\mathbf{A}\big(\mathbf{p}(kT_s)\big), \tag{2.28}$$

$$\mathbf{B}\big[\mathbf{p}[k]\big] = T_s\mathbf{B}\big(\mathbf{p}(kT_s)\big), \tag{2.29}$$

$$\mathbf{C}\big[\mathbf{p}[k]\big] = \mathbf{C}\big(\mathbf{p}(kT_s)\big), \tag{2.30}$$

$$\mathbf{D}\big[\mathbf{p}[k]\big] = \mathbf{D}\big(\mathbf{p}(kT_s)\big), \tag{2.31}$$

where the parentheses indicate the continuous LPV representations of state-space matrices, while the brackets the discretized ones of the corresponding model. Sample time is denoted by T_s, while the discrete step by k.

On the contrary, the DKF can be implemented using the exact discretization given by:

$$\mathbf{A}\big[\mathbf{p}[k]\big] = e^{\mathbf{A}\left(\mathbf{p}(kT_s)\right)T_s}, \tag{2.32}$$

$$\mathbf{B}\big[\mathbf{p}[k]\big] = \mathbf{A}^{-1}\big(\mathbf{p}(kT_s)\big)\left(e^{\mathbf{A}(\mathbf{p}(kT_s))T_s} - \mathbf{I}\right) \cdot \mathbf{B}\big(\mathbf{p}(kT_s)\big), \tag{2.33}$$

$$\mathbf{C}\big[\mathbf{p}[k]\big] = \mathbf{C}\big(\mathbf{p}(kT_s)\big), \tag{2.34}$$

$$\mathbf{D}\big[\mathbf{p}[k]\big] = \mathbf{D}\big(\mathbf{p}(kT_s)\big), \tag{2.35}$$

As a result of the LPV discretization, the discrete propagation can be expressed in the following state-space form:

$$\hat{\mathbf{x}}^-[k] = \mathbf{A}\big[\mathbf{p}[k]\big]\hat{\mathbf{x}}[k-1] + \mathbf{B}\big[\mathbf{p}[k]\big]\mathbf{u}[k-1], \tag{2.36}$$

$$\mathbf{P}^-[k] = \mathbf{A}\big[\mathbf{p}[k]\big]\mathbf{P}[k-1]\mathbf{A}^T\big[\mathbf{p}[k]\big] + \mathbf{Q}, \tag{2.37}$$

$$\mathbf{P}_{\mathbf{p}}^-[k] = \mathbf{P}_{\mathbf{p}}[k-1]\lambda^{-1}, \tag{2.38}$$

	JKF	DKF
state vector	$[\mathbf{x}_s\ \mathbf{x}_p]^T$	$\mathbf{x}_s$, $\mathbf{x}_p$
state vector dim.	$(n+p)$ x 1	n x 1, p x 1
state matrix dim.	$(n+p)$ x $(n+p)$	n x n
error covariance matrix dim.	$(n+p)$ x $(n+p)$	n x n, p x p
Kalman gain dim.	$(n+p)$ x 1	n x 1, p x 1

Table 2.1: Comparison of JKF and DKF

where $\mathbf{u}[k-1]$ is the integral of the continuous input from $(k-1)T_s$ to kT_s. The $\hat{\mathrm{x}}^-$ and $\mathbf{P}^-$ are the predicted state variables and error covariance, respectively, while $\hat{\mathrm{x}}$ and $\mathbf{P}$ are the posteriori state estimate and posteriori error covariance. The $\mathbf{Q}$ process noise covariance matrix is the tuning parameter and the λ is the forgetting factor.

In the update phase, the predicted values are corrected with the new measurements:

$$\mathbf{K}[k] = \mathbf{P}^-[k]\mathbf{C}^T \cdot \left[\mathbf{p}[k]\right]\left(\mathbf{C}\left[\mathbf{p}[k]\right]\mathbf{P}^-[k]\mathbf{C}^T\left[\mathbf{p}[k]\right] + \mathbf{R}\right)^{-1}, \tag{2.39}$$

$$\hat{\mathrm{x}}[k] = \hat{\mathrm{x}}^-[k] + \mathbf{K}[k]\Big(\mathbf{y}[k] - \mathbf{C}\left[\mathbf{p}[k]\right]\hat{\mathrm{x}}^-[k]\Big), \tag{2.40}$$

$$\mathbf{P}[k] = \Big(\mathbf{I} - \mathbf{K}[k]\mathbf{C}\left[\mathbf{p}[k]\right]\Big)\mathbf{P}^-[k]. \tag{2.41}$$

The main differences between the filters are summarized in Table 2.1, where n is the number of state variables and p is the number of parameters.

The study included 4 different KFs. The filters can be categorized by type and utilized model. A specific filter is identified by a consequent notation: the model name (IVP or Hovorka), followed by the abbreviation of the filter type (DKF or JKF). During the tuning process, the virtual patient and the observer utilized the same model, either the IVP or the Hovorka; dissimilarity between them was caused by a fixed +30% variability in all the model parameters. This amount of variability is in physiologically relevant ranges according to [R34, R24]. The Q covariance matrix had non-zero elements only in the main diagonal.

To lessen the human factor, and make the comparison between observers fairer, we tuned the Q matrix with Matlab GA. The optimization was done on a 24-hour-long BG trajectory of a virtual patient with parameter variability. The optimization was driven by a cost function where only the transients were considered, as we observed in previous simulations that the filters cannot compensate for the steady-state offset. If the whole trajectory would be taken into account, the optimizer would adjust the transient to reduce the cost function; however, it can result in distorted, unfavourable responses, as shown in Fig. 2.1. The result of a tuning considering only the transient is denoted by "A", while a tuning taking into account the steady-state also is denoted by "B". Although "B" yields a lower NRMSE compared to "A", the latter one is preferred, since it provides a more realistic waveform.

The elements lying in the main diagonal of the Q covariance matrix were the tuning parameters, also known as genes of an individual. The lower bounds of the parameters were set to zero. The upper bounds were set to a value at least as large, as if this value would be the only non-zero element in the Q matrix, the filter would still converge to the measurements. The numerical results are shown in Table 2.2.

Since this tuning method utilizes all the state variables, it can be applied only in-silico, due to the non-measurable variables in clinical practice. This was a reasonable compromise to make since our main goal was to provide uniform settings during the investigations. There is a significant difference in the number of state variables between the models, the Dalla Man model (used by the UVa-Padova simulator) has 20 state variables, the Hovorka

	DKF		JKF	
Not.	IVP	Hovorka	IVP	Hovorka
1,1	18000	0.2418	17990	0.5814
2,2	$2.993{\cdot}10^{-6}$	2.498	$2.909{\cdot}10^{-6}$	0.1831
3,3	5	$8.377{\cdot}10^{-5}$	4.986	$1.252{\cdot}10^{-5}$
4,4	48.13	$1.867{\cdot}10^{-4}$	49.99	0.005
5,5	18000	$1.974{\cdot}10^{-5}$	18010	0
6,6	0.75	$2.199{\cdot}10^{-3}$	-	0.0186
7,7	-	$4.861{\cdot}10^{-5}$	-	$9.967{\cdot}10^{-4}$
8,8	-	$4.986{\cdot}10^{-5}$	-	$9.150{\cdot}10^{-4}$
9,9	-	-	-	9.951
Q_p	-	1000	-	-
λ	-	0.8742	-	-

Table 2.2: KF tuning table. The notations indicate the element of the Q matrix. As an example 2,2 is the element in the second row and in the second column

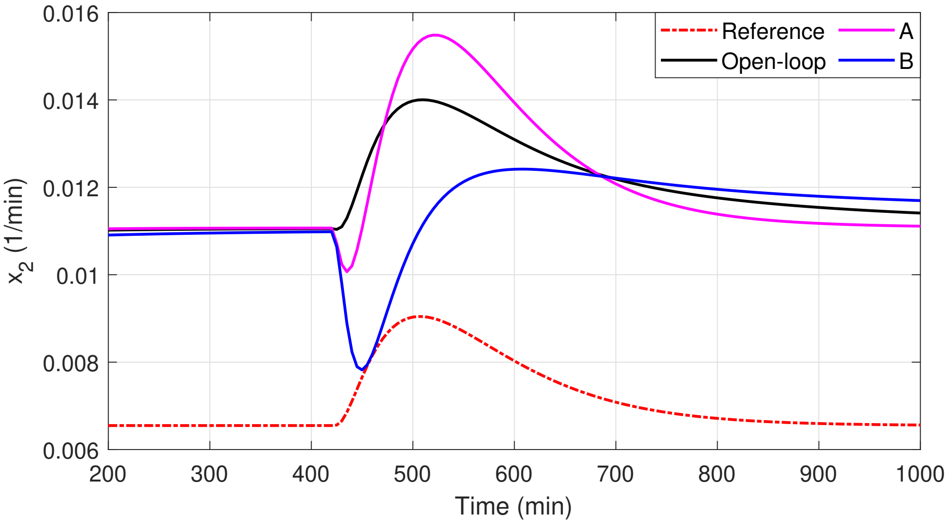

Figure 2.1: Effect of not compensating the steady state offset.

model has 8 state variables and the IVP model has 4 state variables. There are three equivalent variables between the models (with different units of measurement), namely the BG, Ip, and R_A. To achieve that these common variables are presented with the same weights in the cost functions (2.44)-(2.45), two coefficients are introduced. By applying the weights $\frac{9}{5}$ and $\frac{3}{5}$ in (2.45), the error in the BG, Ip and R_A yields the same amount of cost in the Hovorka and the IVP model independently of their corresponding system order.

During the tuning process, it has been observed that the genetic algorithm could overfit the optimization scenario and small-amplitude oscillations could appear or the shape of the trajectory can be unrealistic as shown in Fig. 2.1. To avoid this artefact, a measure of oscillation was formulated and penalized in the cost function. The penalizing coefficient, x_{osc}, is calculated in the following way:

$$x_{osc} = \sum_{i=3}^{n} \mid sgn(x_i - x_{i-1}) - sgn(x_{i-1} - x_{i-2}) \mid, \tag{2.42}$$

$$k = \begin{cases} 10, & \text{if } x_{osc} > threshold \\ 1, & \text{otherwise} \end{cases} \tag{2.43}$$

where x is the state vector of the applied models, n is the number of samples, and the thresholds were dependent on the direction changes of the reference trajectory. These numbers were determined in a way, to ensure that the estimated trajectory has the same number of direction changes as the reference. The k penalizing coefficient increases the cost by an order of magnitude, enforcing the genetic algorithm to find a solution under the threshold. We found that the CGMS noise does not affect significantly the final result, thus the generated measurement data was the true blood glucose values of one of the models. Taking into account the aforementioned factors, the cost functions J_{IVP} and $J_{Hovorka}$ have been developed for each virtual patient model:

$$J_{IVP} = k(e_G + e_{I_{eff}} + e_{I_p} + e_{I_{sc}} + e_{R_A}) \tag{2.44}$$

$$J_{Hovorka} = k\Big(\frac{9}{5}(e_G + e_{I_p} + e_{R_A}) + \frac{3}{5}(e_{Q_2} + e_{x_1} + e_{x_2} + e_{x_3} + e_{S_1} + e_{S_2})\Big) \tag{2.45}$$

where e denotes the NRMSE of the given state variable (see the corresponding notations in [R20] and [R24]) and k is the penalizing coefficient.

2.3.5 General description

The purpose of the comparison is to study the impact on the estimation performance of the following factors:

- “Model": the structure of the model was considered by comparing the IVP model.
- “Observer": the observers were assessed with the comparison of the NSMO.

We performed 6 simulations – one for each combination of models and observers – with the academic version of the UVa-Padova simulator [R40], which was extended with added features for intra-patient variability generation. The scenario consisted in a 24-h simulation including three meals (45 g at 7 h, 70 g at 14 h, and 60 g at 21 h) and multiple sources of variability, namely, CGMS error according to the default model in the simulator; sinusoidal-based circadian insulin variation with uniformly-distributed amplitude of $\pm 30\%$; and, variability of subcutaneous insulin absorption according to a uniform distribution of $\pm 30\%$. For each of the 10 virtual adults, we repeated the simulation three times with different variability instances.

Remark that when comparing different types of observers, tuning may bias the results. For the fairness of the comparison, we tuned the three observers for them to perform similarly under the same tuning scenario. To this end, we set the Q matrix of the KFs by optimization, and the disturbance bound of the NSMO by exhaustive simulations.

2.3.6 Statistical analysis

We used the root-mean-square error (RMSE), the median absolute error (MAE), and the maximum absolute error (MaxAE) to study the estimation accuracy of the BG, I_p, and R_A. To avoid influencing the metrics with the initial condition transient, we neglected the first 30 min of the simulation when computing the metrics.

For each signal, a multifactorial ANOVA determined whether the factors “Model" and “Observer" and their interaction explained the variability found in the performance metrics. Since all the simulations shared the cohort of patients and the meals, the hypothesis of independence was unmet[R41]. For this reason, we considered as new covariates the factor “Subject" – the identifiers for each of the virtual subjects – together with the interactions “Subject:Model" and “Subject:Observer".

When a factor (or interaction) was significant, a pairwise comparison was performed to determine which level (or combination of levels in the interaction) cause the factor (or interaction) to be significant. Given the skewness of the distribution, the sign test was selected to determine if the median difference between the performance metrics of the groups is significantly different from 0 at a 0.05 confidence level [R42]. The Benjamini-Hochberg p-value correction approach [R43] was applied to control the false discovery rate in the case of multiple comparisons.

The ANOVA and sign test only inform whether the observed differences among the levels of a factor are non-random (statistically significant difference) or they originated from the randomness of the simulations. However, these tests do not inform about the magnitude of these differences or their practical relevance. To analyse this information, we calculated two metrics: the eta-squared (η^2) – which measures the proportion of variance associated with each factor [R44] –, and the 95% confidence interval around the median difference (with the correction in[R45] to control the false coverage rate).

2.3.7 Virtual Patient Model

The analysis of the structural identifiability of the IVP model determines that all the parameters are structurally locally identifiable when the plasma insulin is measured, which is coherent with the results in [R24]. The sensitive parameters are S_I, EGP, C_I, and $GEZI$; whereas, parameters τ_1, and p_2 are mildly sensitive. The only insensitive parameter is τ_2; its nominal value was used instead of being identified.

Among the sensitive parameters, we individualized S_I and C_I because they are related to the steady state conditions of all the state variables. Table **??** shows the identified parameters for the 10 virtual adults in the UVa-Padova simulator.

2.3.8 Hovorka model

Likewise the IVP model, the Hovorka model parameters are structurally locally identifiable if the plasma insulin is known. The sensitive parameters of this model are V_i, k_e, S_{i1}, k_{12}, S_{i2}, F_{01}, S_{i3}; the mildly sensitive are EGP, τ_s and V_g and finally, the insensitive parameters are the remaining ones. The sensitive and mildly sensitive parameters were included in the identification of the average model, while the insensitive ones were fixed to the nominal values in [R20]. Parameters V_i and S_{i1} were selected to be individualized, since they are the most sensitive gains of the insulin subsystem and glucose subsystem, respectively. Table **??** includes the identified parameters.

2.4 Identification assessment

The identified parameters of the average models (Tables **??** and **??**) accurately fitted the glucose; they achieved an NRMSE of 9.87% for the IVP model and 6.32% for the Hovorka model.

Both models achieved a low NRMSE for the plasma insulin. However, the IVP model fits the plasma insulin better (3.69% vs. 6.38%). The main difference between the models

Parameter	Average patient	Individual
S_I (mL/μU/min)	$7.03 \cdot 10^{-4}$	$6.95 \cdot 10^{-4}$
		$6.19 \cdot 10^{-4}$
		$6.34 \cdot 10^{-4}$
		$7.88 \cdot 10^{-4}$
		$7.25 \cdot 10^{-4}$
		$4.59 \cdot 10^{-4}$
		$6.77 \cdot 10^{-4}$
		$6.79 \cdot 10^{-4}$
		$7.35 \cdot 10^{-4}$
		$7.74 \cdot 10^{-4}$
EGP (mg/dL/min)	1.49	-
C_I (mL/min)	$1.11 \cdot 10^{3}$	$1.16 \cdot 10^{3}$
		$1.13 \cdot 10^{3}$
		$1.28 \cdot 10^{3}$
		$1.02 \cdot 10^{3}$
		$9.31 \cdot 10^{2}$
		$1.15 \cdot 10^{3}$
		$1.09 \cdot 10^{3}$
		$1.09 \cdot 10^{3}$
		$9.06 \cdot 10^{3}$
		$1.18 \cdot 10^{3}$
$GEZI$ $\left(\text{min}^{-1}\right)$	$3.03 \cdot 10^{-8}$	-
τ_1 (min)	52.71	-
τ_2 (min)	45.41	-
p_2 $\left(\text{min}^{-1}\right)$	$2.85 \cdot 10^{-2}$	-

Table 2.3: Virtual Patient model parameters. The parameter τ_2 was obtained as the mean of the values included in [R24]

Parameter	Average patient	Individual
τ_s (min)	43.00	-
$k_e\ \left(\mathrm{min}^{-1}\right)$	$1.36 \cdot 10^{-1}$	-
V_i (L/kg)	$1.18 \cdot 10^{-1}$	$1.09 \cdot 10^{-1}$
		$1.04 \cdot 10^{-1}$
		$1.36 \cdot 10^{-1}$
		$1.16 \cdot 10^{-1}$
		$1.05 \cdot 10^{-1}$
		$1.19 \cdot 10^{-1}$
		$1.74 \cdot 10^{-1}$
		$8.41 \cdot 10^{-2}$
		$1.00 \cdot 10^{-1}$
		$1.09 \cdot 10^{-1}$
V_g (L/kg)	$2.22 \cdot 10^{-2}$	-
$k_{12}\ \left(\mathrm{min}^{-1}\right)$	$9.11 \cdot 10^{-2}$	-
$S_{i1}\ \left(\mathrm{min}^{-1}\ \text{per}\ \mathrm{mUL}^{-1}\right)$	$2.13 \cdot 10^{-3}$	$2.20 \cdot 10^{-3}$
		$1.65 \cdot 10^{-3}$
		$1.84 \cdot 10^{-3}$
		$3.02 \cdot 10^{-3}$
		$2.62 \cdot 10^{-3}$
		$9.45 \cdot 10^{-4}$
		$1.90 \cdot 10^{-3}$
		$2.52 \cdot 10^{-3}$
		$2.42 \cdot 10^{-3}$
		$2.35 \cdot 10^{-3}$
$S_{i2}\ \left(\mathrm{min}^{-1}\ \text{per}\ \mathrm{mUL}^{-1}\right)$	$1.02 \cdot 10^{-3}$	-
S_{i3} (L/mU)	$3.92 \cdot 10^{-3}$	-
$k_{a1}\ \left(\mathrm{min}^{-1}\right)$	$2.35 \cdot 10^{-3}$	-
$F01\ \left(\mathrm{mmol} \cdot \mathrm{kg}^{-1}\mathrm{min}^{-1}\right)$	$1.28 \cdot 10^{-2}$	-
$EGP\ \left(\mathrm{mmol} \cdot \mathrm{kg}^{-1}\mathrm{min}^{-1}\right)$	$2.37 \cdot 10^{-2}$	-

Table 2.4: Hovorka's model parameters

is that the Hovorka model has a slower response due to a higher order in the insulin pharmacokinetics model.

Moreover, fit degraded when the average models were used for the different adult subjects in the cohort (see Fig. 2.2), specially for the BG fit provided by the Hovorka model. The larger degradation of the fit in the Hovorka model might be related to an over-parametrization of the insulin effect subsystem: Whereas the simulator model uses two compartments to describe the insulin effect [R40], the Hovorka model adds an additional compartment to describe the insulin effect on the glucose transport, *i.e.* the state variable $x_1(t)$. Also, it turned out that S_{i1} is a sensitive parameter that was chosen to individualize the model. This denotes a structural deficiency of the Hovorka model concerning the Dalla Man model. This over-parametrization could cause some overfitting problems, which make the model sensitive to different patients.

Model individualization improved the fit and reduced the difference in terms of NRMSE between both models. No statistically significant evidence existed to consider that the median difference in the NRMSE of the glucose between both models is different from 0, according to the sign test, at a confidence level of 0.05. Model individualization also reduced the variability of the plasma insulin, but the IVP model improved the accuracy of the Hovorka model.

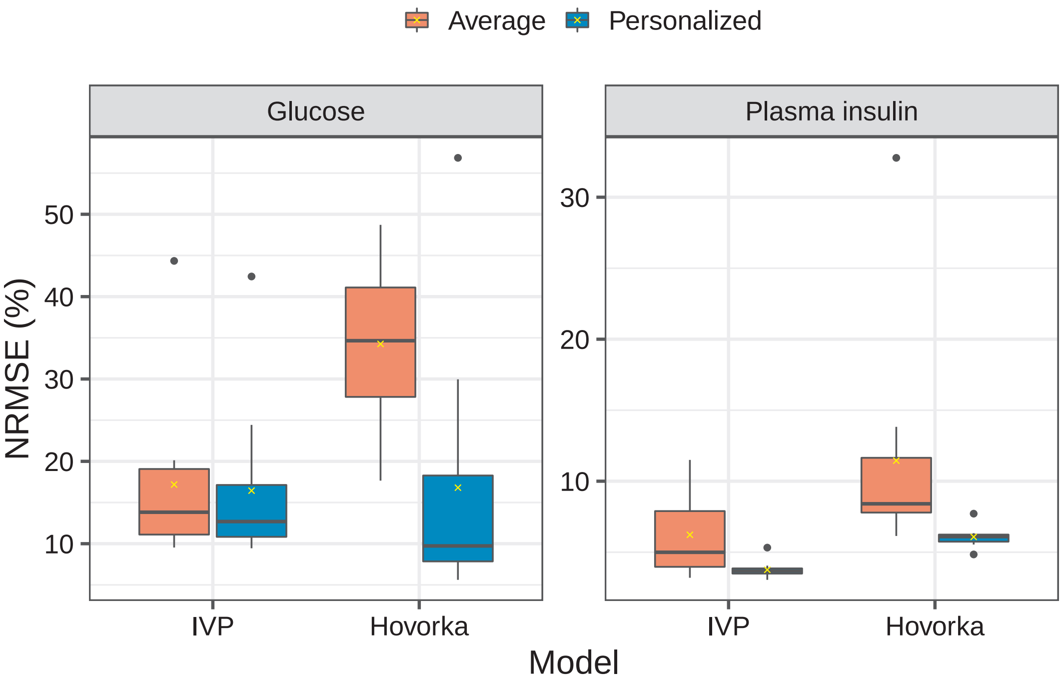

Figure 2.2: Evaluation of the NRMSE for the identificated IVP and Hovorka models

Since the individualized models fitted the plasma insulin and the plasma glucose better than the average model, we used the individualized models to design the observers.

	RMSE		MAE		MaxAE	
	η^2	P	η^2	P	η^2	P
Model	0.40	0.00*	0.50	0.00*	0.00	0.97
Observer	0.30	0.05	0.90	0.00*	0.00	0.83
Subject	89.20	0.00*	86.60	0.00*	85.10	0.00*
Model:Observer	0.20	0.21	0.10	0.37	0.70	0.02*
Model:Subject	2.20	0.00*	3.90	0.00*	1.10	0.14
Observer:Subject	0.50	0.96	0.20	1.00	1.70	0.34
Residuals						

Table 2.5: Summary of ANOVA results of rate of glucose appearance. It summarizes three metrics: the root-mean-square error (RMSE), the mean absolute error (MAE) and the maximum absolute error (MaxAE). Terms "η^2" and "P" denote the eta squared effect size measurement and the P-value of the ANOVA F-statistics, respectively. The asterisk (*) indicates a P-Value lower than 0.05.

2.5 Results

2.5.1 Rate of glucose appearance

Overall, observers imprecisely estimated the R_A, since the CGMS noise and model uncertainties are coupled with the estimation. For example, in Fig. 2.3, the estimated R_A has negative values: an unphysiological behaviour for a scenario without exercise.

The type of model significantly contributed to the variability of RMSE and MAE (Table

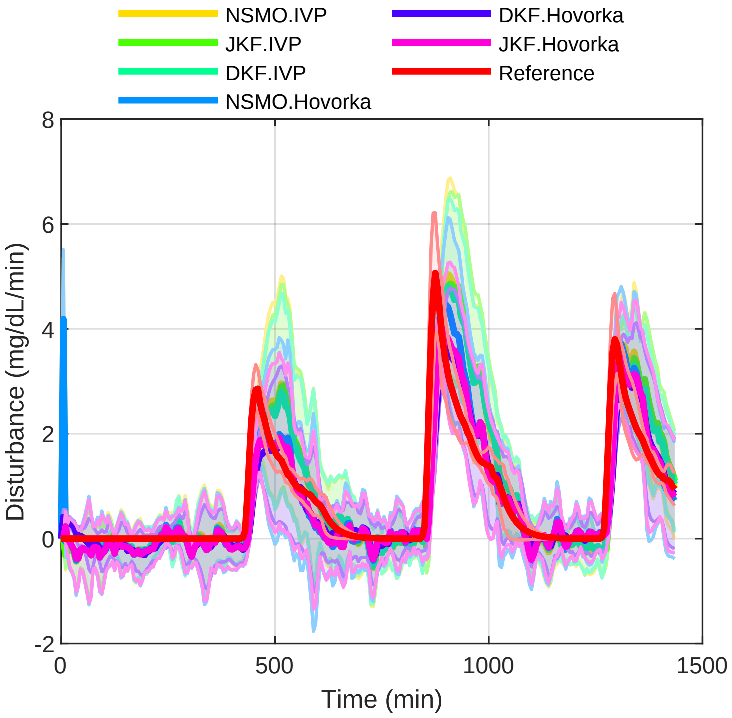

Figure 2.3: Population plot of the estimation of the rate of glucose appearance. Thick lines represent the median of the estimation for the 10 patients and the shaded areas represent the median absolute deviation

	Difference	CI
IVP-Hovorka	0.04 (0.14)	[0.01 , 0.07] *
JKF-DKF	0.05 (0.06)	[0.03 , 0.07] *
NSMO-DKF	0.04 (0.05)	[0.03 , 0.05] *
NSMO-JKF	-0.01 (0.04)	[-0.02 , 0]

Table 2.6: Pairwise comparison of the median difference of the root-mean-square error for the rate of glucose appearance (in $\mathrm{mg/dL/min}$) between the levels of the significant factors. Values are expressed as median (mean absolute deviation). The P-values and confidence intervals (CI) corresponded to the sign test with corrections of false discovery rate and false coverage rate. An asterisk indicates a significant result at 0.05 level

2.5) in the statistical sense (P-value<0.05). Observers designed with the IVP model underperformed the observers designed with the Hovorka model (Fig. 2.4) in terms of RMSE and MAE because the former overestimated the R_A after the postprandial peak and underestimated it in the steady-state (Fig. 2.3). The pairwise comparisons also confirmed the superiority of Hovorka-based observers (Table 2.6 and Table 2.7). However, the median difference was 0.04 $\mathrm{mg/dL/min}$ for both RMSE and MAE, which might be negligible from the application side.

The observer structure also had a statistically significant effect on MAE (the influence on RMSE was not statistically significant). Specifically, DKF observers overperformed NSMO and JKF in 0.04 $\mathrm{mg/dL/min}$ in the median for the MAE (Fig. 2.7) and in 0.05 $\mathrm{mg/dL}$ for the RMSE (Fig. 2.6). Conversely, NSMO and JKF behaved similarly, although the NSMO observers had a higher peak during the transient (Fig. 2.3), not considered in the calculation of the metrics (see Section 2.3.6).

Unlike the analysis of RMSE and MAE, ANOVA of MaxAE identified a statistically significant effect of the interaction between the model and the observer (Table 2.5). The DKF

	Difference	CI	
IVP-Hovorka	0.04 (0.09)	[0.02 , 0.06]	*
JKF-DKF	0.04 (0.03)	[0.03 , 0.05]	*
NSMO-DKF	0.04 (0.02)	[0.03 , 0.05]	*
NSMO-JKF	0 (0.02)	[-0.01 , 0.01]	

Table 2.7: Pairwise comparison of the median difference of the mean absolute error for the rate of glucose appearance (in $\mathrm{mg/dL/min}$) between the levels of the significant factors. Values are expressed as median (mean absolute deviation). The P-values and confidence intervals (CI) corresponded to the sign test with corrections of false discovery rate and false coverage rate. An asterisk indicates a significant result at 0.05 level

	RMSE		MAE		MaxAE	
	η^2	P	η^2	P	η^2	P
Model	8.50	0.00*	10.50	0.00*	11.80	0.00*
Observer	2.40	0.00*	1.60	0.00*	3.60	0.00*
Subject	66.60	0.00*	65.60	0.00*	60.80	0.00*
Model:Observer	0.20	0.54	0.10	0.63	0.30	0.35
Model:Subject	1.20	0.53	2.00	0.13	1.40	0.46
Observer:Subject	0.40	1.00	0.40	1.00	0.50	1.00
Residuals						

Table 2.8: Summary of ANOVA results of plasma insulin. It summarizes three metrics: the root-mean-square error (RMSE), the mean absolute error (MAE) and the maximum absolute error (MaxAE). Terms “η^2” and “P-value” denote the eta squared effect size measurement and the P-value of the ANOVA F-statistics, respectively. The asterisk (*) indicates a P-Value lower than 0.05.

observer designed with the Hovorka model illustrated the importance of this interaction since it had the largest MaxAE (Fig. 2.4); it even underperformed the observers designed with the IVP, which differed from the conclusions of RMSE and MAE.

Finally, although the ANOVA identified the type of model, the observer structure, or its interaction as statistically significant factors, the analysis of the η^2 determined that these factors contributed less than 1% to the variability of the metrics (Table 2.5). In contrast, “Subject" and “Model:Subject" explained more than 90% of the variability, evincing that no observer technique managed to cope with the large inter-patient variability of the simulation. In addition, this result unveiled the limitations of the personalized models used to design the observer, even though we identified these models with the knowledge of the plasma insulin and meal rate of appearance.

2.5.2 Plasma insulin estimation

Model structure and observer type caused remarkable differences in the RMSE, MAE, and MaxAE (Fig. 2.5). Indeed, ANOVA supported for the three metrics significant differences between the IVP and Hovorka models on the one side and between the DKF, JKF, and NSMO on the other side (Table 2.8).

The post-hoc analyses in Tables 2.9 - 2.11 determined that no significant differences between the NSMO and the JKF existed, which agreed with Fig. 2.6, where the responses of both observers mostly overlap. DKF observers were the only ones that statistically differ; they lower, in the median, the RMSE in 0.5 $\mathrm{mU/L}$, the MAE in 0.3 $\mathrm{mU/L}$, and the MaxAE in 2.92 $\mathrm{mU/L}$. Since the gain related to the I_p in the KFs was near 0 and, it was exactly 0 for

	Difference	CI	
IVP-Hovorka	-0.92 (0.4)	[-1.05 , -0.83]	*
JKF - DKF	0.52 (0.3)	[0.45 , 0.65]	*
NSMO - DKF	0.52 (0.3)	[0.65 , 0.45]	*
NSMO - JFK	0 (0)	[0 , 0]	

Table 2.9: Pairwise comparison of the median difference of the root-mean-square error for the plasma insulin (in $\mathrm{mU/L}$) between the levels of the significant factors. Values are expressed as median (mean absolute deviation). The P-values and confidence intervals (CI) corresponded to the sign test with corrections of false discovery rate and false coverage rate. An asterisk indicates a significant result at 0.05 level

	Difference	CI	
IVP-Hovorka	-0.74 (0.32)	[-0.82 , -0.62]	*
JKF-DKF	0.3 (0.21)	[0.24 , 0.36]	*
NSMO-DKF	0.3 (0.21)	[0.24 , 0.36]	*
NSMO-JKF	0 (0)	[0 , 0]	

Table 2.10: Pairwise comparison of the median difference of the mean absolute error for the plasma insulin (in $\mathrm{mL/U}$) between the levels of the significant factors. Values are expressed as median (mean absolute deviation). The P-values and confidence intervals (CI) corresponded to the sign test with corrections of false discovery rate and false coverage rate. An asterisk indicates a significant result at 0.05 level

the NSMO, the only difference between observers was the discretization method: whereas the NSMO and the JFK were based, respectively, on an implicit and explicit Euler method, the DKF employed a zero-order hold discretization that lead to more accurate results.

The IVP model significantly improveed the performance of the estimation compared to the observers designed with the Hovorka model – with median reductions of 0.92, 0.72, and 5 $\mathrm{mU/L}$ in the RMSE, the MAE, and the MaxAE, respectively. In Section 2.4, we already observed these differences between models when analysing the fit of the identified models, indicating that the use of the observer could not cope with the deficiencies of the models. The superiority of the IVP was related to a quicker response in the I_p dynamics than the Hovorka model (Fig. 2.6). The slower dynamics of the Hovorka model might be explained by the 2-compartment model that describes the subcutaneous absorption with an equal transfer rate between compartments.

The interaction between the type of model and the observer structure was not significant. This result agrees with Fig. 2.5, where the DKF always reduces the RMSE compared to the JKF and NSMO, regardless of the utilized model.

The type of model contributed more to the performance of the observer than the observer structure did (Table 2.8). However, as observed in the analysis of the R_A, the variability explained by “Subject” and the interactions “Model:Subject” and “Observer:Subject” – 67.6% of the RMSE, 68.0% of the MAE, and 62.7% of the MaxAE – was much larger than the sum of type of model, observer structure and interaction – 11.1% of the RMSE, 12.2% of the MAE, and 15.7% of the MaxAE. Again, this revealed the limitation of the observers to overcome the inter-patient variability.

2.5.3 Glucose measurement

The ANOVA in Table 2.12 determined that the type of model, the observer structure, and its interaction significantly explained the variance of the RMSE, the MAE, and the MaxAE. Although all the levels in the interaction between the type of model and the observer struc-

	Difference	CI	
IVP-Hovorka	-5.79 (3.26)	[-6.53 , -4.73]	*
JKF-DKF	2.92 (1.73)	[2.68 , 3.85]	*
NSMO-DKF	2.92 (1.73)	[2.68 , 3.85]	*
NSMO-JKF	0 (0)	[0 , 0]	

Table 2.11: Pairwise comparison of the median difference of the maximum absolute error for the plasma insulin (in mL/U) between the levels of the significant factors. Values are expressed as median (mean absolute deviation). The P-values and confidence intervals (CI) corresponded to the sign test with corrections of false discovery rate and false coverage rate. An asterisk indicates a significant result at 0.05 level

	RMSE		MAE		MaxAE	
	η^2	P	η^2	P	η^2	P
Model	19.50	0.00*	19.50	0.00*	19.30	0.00*
Observer	40.50	0.00*	40.60	0.00*	40.00	0.00*
Subject	0.10	0.02*	0.10	0.14	0.10	0.47
Model:Observer	38.70	0.00*	38.80	0.00*	38.30	0.00*
Model:Subject	0.10	0.02*	0.10	0.16	0.10	0.49
Observer:Subject	0.20	0.00*	0.20	0.09	0.30	0.51
Residuals						

Table 2.12: Summary of ANOVA results of CGMS. It summarizes three metrics: the root-mean-square error (RMSE), the mean absolute error (MAE) and the maximum absolute error (MaxAE). Terms "η^2" and "P" denote the eta squared effect size measurement and the P-value of the ANOVA F-statistics, respectively. The asterisk (*) indicates a P-Value lower than 0.05.

ture were statistically different, the median differences were, at most, 0.10 $\mathrm{mg/dL}$ for the RMSE, 0.07 $\mathrm{mg/dL}$ for the MAE, and 0.4 $\mathrm{mg/dL}$ for the MaxAE. Such minor differences are negligible from the clinical point of view.

Unlike the analysis of the R_A and the I_p, the type of model, the observer structure, and its interaction fully explained the variability of the performance metrics – 98.7% of the RMSE, 98.9% of the MAE, and 97.6% of the MaxAE. Since glucose was the only signal available online, the observers handle the inter-patient variability, which contributed less than 1% to the variability.

2.6 Thesis summary

Tackling nonlinearity is an essential part in designing control algorithms for artificial pancreas. Physiological systems are highly nonlinear and time varying, thus designing efficient algorithms that can handle them are important aspects of the field. My goal was to design discretized Kalman filters based on linear parameter varying methodologies as they proved to be an efficient method to tackle state estimation problem in nonlinear systems. Also, my aim was to evaluate how the method compares to different estimation methods, and how the underlying mathematical models affect the performance. In [C1] I designed Dual Kalman filters based on linear parameter varying methodology, in [J1] a Kalman filter has been applied in simulations for closed-loop blood glucose control. Then in [C2, J2], the Kalman filters were analyzed based on different models, disturbance estimation and state estimation capabilities. Also, the tuning process of the filters were standardized.

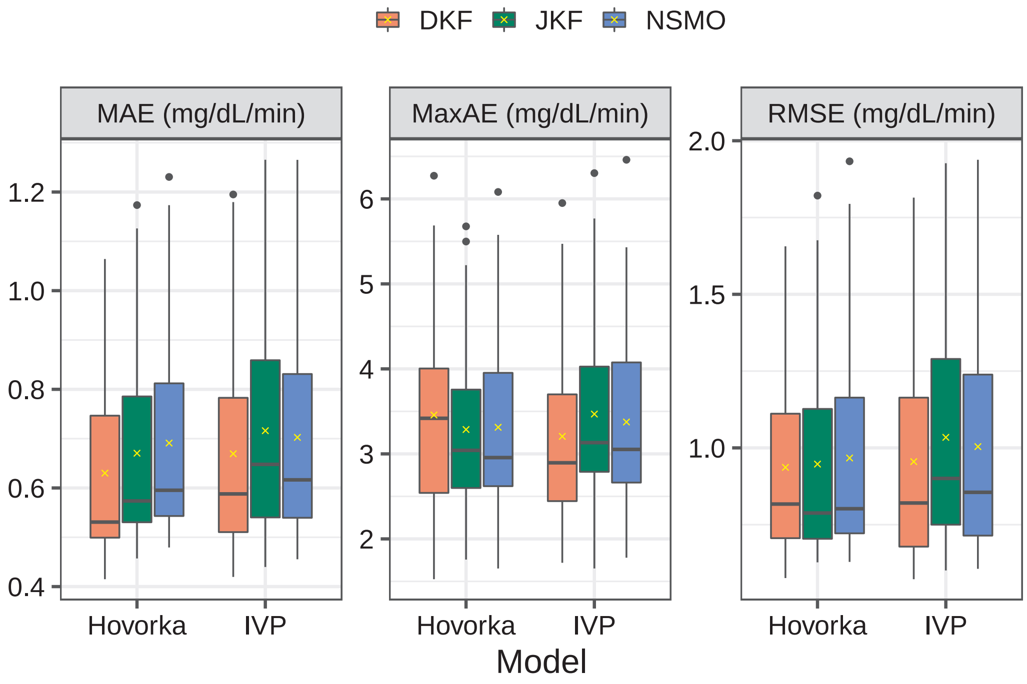

Figure 2.4: Grouped boxplot for the rate of glucose appearance. It represents the mean absolute error (MAE), maximum absolute error (MaxAE) and the root-mean-square error (RMSE) of the rate of glucose appearance (in $\mathrm{mg/dL/min}$). The length of the box corresponds to the interquartile range, the black solid line is the median and the yellow cross is the mean.

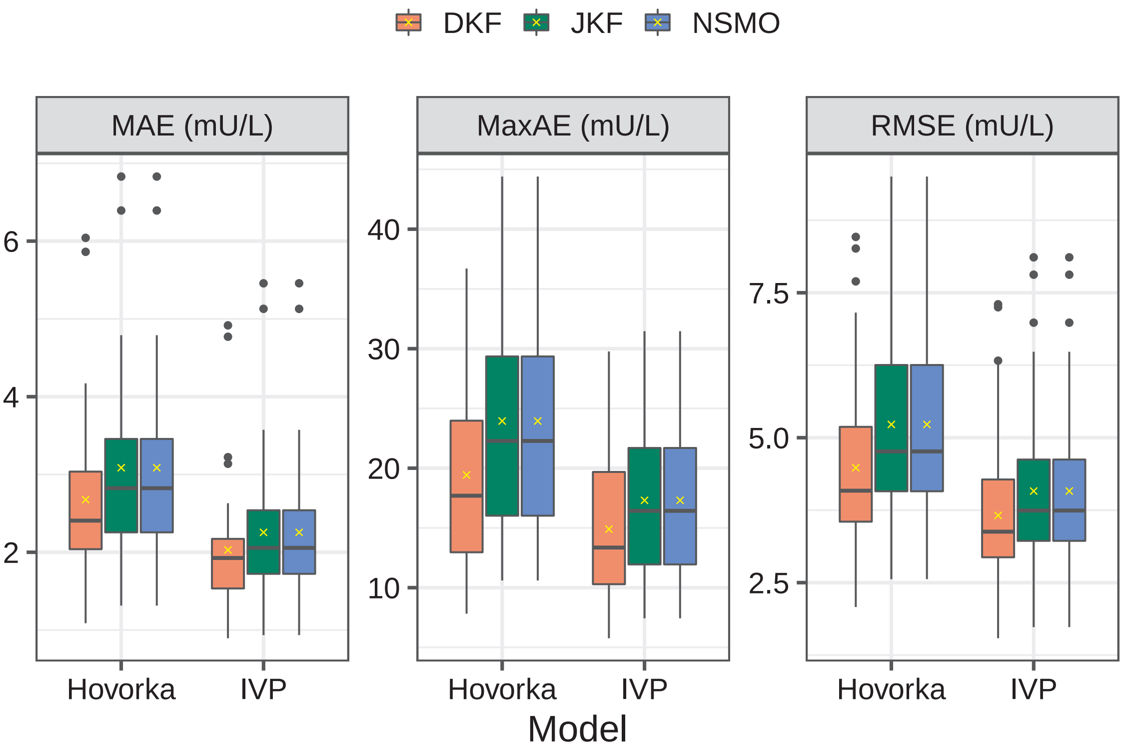

Figure 2.5: Grouped boxplot for the plasma insulin. It represents the mean absolute error (MAE), maximum absolute error (MaxAE) and the root-mean-square error (RMSE) of the plasma insulin (in mU/L). The length of the box corresponds to the interquartile range, the black solid line is the median and the yellow cross is the mean.

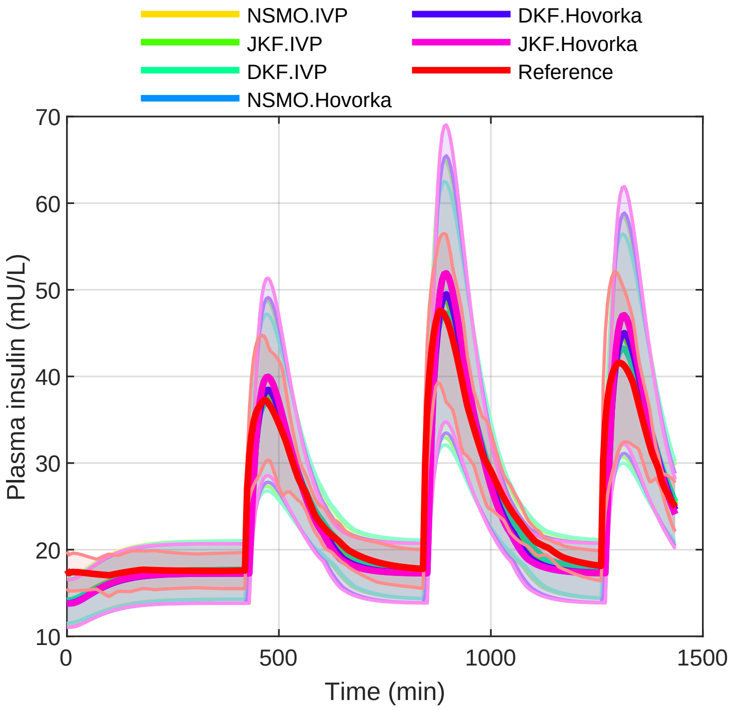

Figure 2.6: Population plot for the estimation of the plasma insulin. Thick lines represent the median for the 10 subjects in the cohort, and the shaded area the mean absolute deviation.

3

Digital twin in Artificial Pancreas

Thesis group 2: Moving horizon estimation-based digital twin in artificial pancreas

Thesis 2
I developed and investigated moving horizon estimation-based digital twin methodologies to represent the patient's glucose metabolism and trace intrapatient variability.

Thesis 2.1
I have developed moving horizon estimation based methodology to trace parameter variability of the patient with a strong focus on constraining the parameters to represent the physiologically relevant values.

Thesis 2.2
I developed and investigated meal estimation accuracy in a moving horizon estimation-model predictive control scenario.

Thesis 2.3
I implemented the moving horizon estimation as just-in-compiled functions and on the graphical processing unit to make the method scalable for large patient populations.

Publications relevant to the theses: [C3, C4, C5, C6].

Findings in my first thesis led to the conclusion that the structure of the mathematical model and the accuracy of the patient parameters can have greater impact on the estimation accuracy than the state observer algorithm itself. Thus, I focused on parameter estimation methods, with a particular focus on constraining the free parameter space to improve the speed, convergence and consistency. Also, the estimated parameters can be of great use in various applications such as blood glucose prediction, replaying different insulin and meal scenarios, also observing daily or long-term trends in insulin sensitivity. The method and its use-cases fall under the umbrella of digital twins. In [C3], I developed moving horizon estimation based methodology to track intrapatient variability. In [C4], the focus was on the estimation of the endgenous glucose production and extending the model with heart rate as a potential, easy-to-access parameter to describe physical activity. In [C5], the estimation algorithm was extended with a model predictive controller and its performance was evaluated in a simulation environment. In [C6], I optimized the parameter estimation algorithm for tackling large populations as a cloud-based service.

3.1 Parameter estimation to track intrapatient variability

In the first part, the measurements and logged data from an approximately 3-day-long session are used. For the BG concentration measurements a Medtronic Enlite® CGM sensor was used with a sampling frequency of 5 minutes. The subject logged the BG measurements (fingertip glucometer DCont Nemere®), the meal intakes, insulin administrations and physical activities. The heart rate was tracked with a Mi band 5 with a sampling frequency of 1 minute. The subject was on a basal-bolus insulin therapy, with a total daily insulin around 50 Units. A daily long-acting Tresiba and rapid-acting NovoRapid insulin boluses were administered based on the meal intakes. Based on the characteristics of the experimental data and the properties of the model, several considerations have to be made during the identification of the model parameters.

We used the previously introduced IVP model, but extended with the equation describing the rate of appearance as:

$$\begin{aligned}\dot{G}(t) &= -(GEZI + I_{EFF}(t)) \cdot G(t) + EGP \\ &\quad + R_A(t),\end{aligned} \tag{3.1}$$

$$\dot{I}_{EFF}(t) = -p_2 \cdot I_{EFF}(t) + p_2 \cdot S_I \cdot I_P(t) \tag{3.2}$$

$$\dot{I}_P(t) = -\frac{1}{\tau_2} I_P(t) + \frac{1}{\tau_2} I_{SC}(t) \tag{3.3}$$

$$\dot{I}_{SC}(t) = -\frac{1}{\tau_1} I_{SC}(t) + \frac{1}{\tau_1 C_I} u(t) \tag{3.4}$$

$$R_A(t) = \sum_i^m \frac{d_i}{V_G \cdot \tau_{D_i}^2} t_i \cdot e^{-\frac{t_i}{\tau_{D_i}}} \tag{3.5}$$

where $G(t)$ mg/dl is the blood glucose level at time instant t, $I_{EFF}(t)$ min^{-1} is the insulin effect on glucose, $I_{SC}(t)$ and $I_P(t)$ $\mu U/mL$ represent the subcutaneous and plasma insulin concentrations, respectively. The input is the insulin infusion $u(t)$ $\mu U/min$. The infused insulin $u(t)$ $\mu U/min$ serves as the input. Parameters of the insulin submodel: τ_1 min and τ_2 min are time constants of the subcutaneous and plasma insulin compartments, p_2 min^{-1} is the kinetic rate for insulin action, C_I mL/min is the insulin clearance and S_I $mL/\mu U/min$ is the insulin sensitivity. The endogenous glucose production EGP $mg/dl/min$ is modeled by a constant term and $GEZI$ is the glucose effectiveness at zero insulin level, V_G dl is the glucose distribution volume of the patient and A_g $-$ is the carbohydrate utilization constant. A given meal is the disturbance d_i g (carbohydrate content of the meal). The CHO absorption submodel is lumped into the $R_A(t)$ $mg/dl/min$ term, which is the sum of the impulse responses characterized by two first order processes in series with τ_D min time constants.

First, the model (3.1)-(3.5) was mainly developed on experiments with insulin pumps, which differs from the basal-bolus therapy in a key aspect. With insulin pumps, a single type of short-acting insulin is injected in micro boluses. On a theoretical level, when there is no intrapatient variability and the injection site is fixed, a constant set of τ_1, τ_2 and p_2 parameters ought to accurately approximate the insulin absorption profile of the patient. However, in the case of the basal-bolus therapy the long-acting insulin was taken into account as a constant insulin input by assuming that the daily dose was equally absorbed throughout the day. Using this assumption, a constant 1.28 $U/hour$ input was calculated based on the size of the long-acting bolus insulin. For the NovoRapid insulin, an onset of 10-20 min, maximum effect between 1 and 3 hours and duration of 3-5 hours is given [R46]. These information served as the basis for the definition of the bounds for the parameters $\tau_1 \in [30, 50]$, $\tau_2 \in [30, 50]$ and $p_2 \in [1/50, 1/30]$. The given ranges constrained the profiles to represent the properties of the administered insulin. In Fig. 3.1 a tangible example of the feasible profiles with respect to the parameters of the insulin is given. Since here we were interested only in the pharmacokinetics of the insulin, the gains (S_I,C_I) could be neglected, and normalized profiles are visualized.

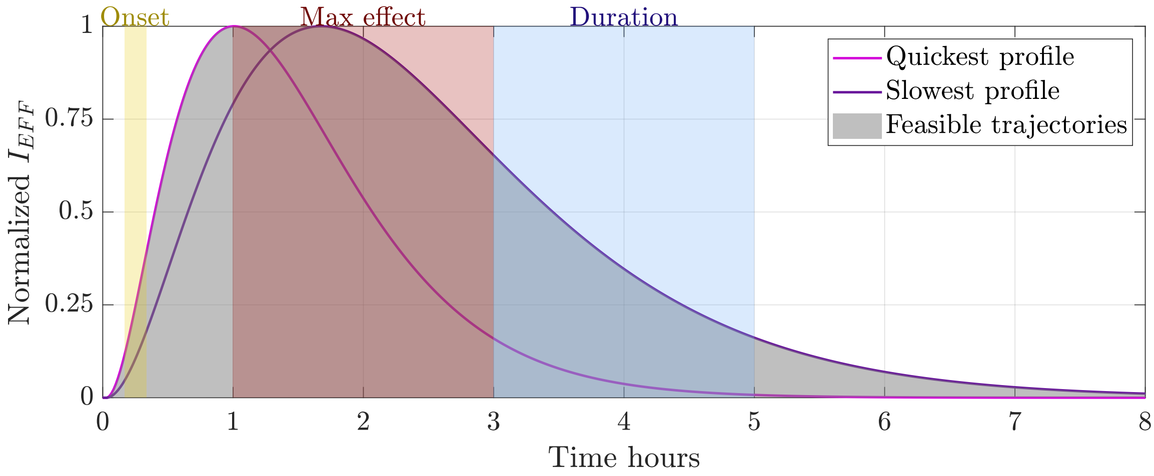

Figure 3.1: Responses to a bolus insulin at $t = 0$. The shaded region defines the approximate trajectories given that a NovoRapid short-acting insulin is used.

The basal glucose concentration is determined by the parameters and the basal insulin infusion. It can be calculated from the steady state of the system ((3.1)-(3.4)) as follows:

$$\bar{G} = \frac{EGP}{GEZI + \frac{S_I}{C_I}\bar{u}}, \tag{3.6}$$

where $\bar{u}$ is the basal insulin infusion and $\bar{G}$ is the basal BG level.

A further restriction was made in the sense of the BG basal levels. To avoid either unrealistically low or high basal levels, a nonlinear constraint was applied based on (3.6). The basal BG level was assumed to be in the range of 80 mg/dl and 120 mg/dl, this assumption correlates well with the BG levels observed in the morning in Fig. 3.3, when the the last meal intake and bolus insulin from the previous day already lost its effect.

The identification was constructed as an optimization problem, where the cost function was defined to be the root-mean-square error (RMSE) between the measured CGMS signal and the simulated BG trajectory. The optimization problem was formulated as

$$\begin{aligned} \min_{\boldsymbol{p} \in \mathbb{R}^n} \quad & J = \sqrt{\frac{1}{L}\sum_{k=1}^{L} \Delta G_k^2} \\ \text{s.t.} \quad & \boldsymbol{p} \in [\boldsymbol{lb}, \boldsymbol{ub}], \\ & 80 \leq \bar{G}_k \leq 120 \quad \forall k, \\ & \boldsymbol{x}_0 = \bar{\boldsymbol{x}} \qquad\qquad \text{(Initial condition)} \end{aligned} \tag{3.7}$$

where L is the number of CGMS measurements evaluated, $\Delta G_k = CGMS_k - G_k$ where G_k is the output of the system at the discrete step k using the forward Euler method. The optimized variable is the n-dimensional $\boldsymbol{p}$ parameter vector with lower and upper bounds defined by $\boldsymbol{lb}$ and $\boldsymbol{ub}$. The dimensionality of the problem depends on the window size, but can be given as $n = n_c + w \cdot n_v + n_m$ where $n_c = 5$ is the number of constant parameters, while $n_v = 3$ is the number of parameters which vary between the windows. Depending on the window size $w \in \{3, 6, 8\}$ and lastly $n_m = 16$ is the number of meals. The initial condition of the x state vector was defined as the steady-state of the system assuming that $d = 0$ and $u = \bar{u}$.

	Constant parameters				
	C_I	p_2	V_g	τ_1	τ_2
lb	372	$1/50$	100	30	50
ub	3350	$1/30$	260	30	50

	Varied parameters			Meal
	EGP	$GEZI$	S_I	τ_D
lb	0.062	$5 \cdot 10^{-4}$	$2.35 \cdot 10^{-5}$	5
ub	2.32	$6 \cdot 10^{-3}$	$2.11 \cdot 10^{-3}$	60

Table 3.1: Lower and upper bounds used during the identification.

Parameter sensitivities were calculated in order to quantify the effect of variabilities on the accuracy of the prediction. The parameter sensitivities are defined by:

$$s_p^{ij} = \frac{\Delta \Psi}{\Delta p} \tag{3.8}$$

$$S_p^{ij} = \frac{p^j}{\Psi_{pred.}^j} s_p^{ij}, \tag{3.9}$$

$$S_p^{msqr} = \sqrt{\frac{1}{n} \sum_{l=1}^{n} \left(S_p^{ij} \right)^2}, \tag{3.10}$$

where $\Delta \Psi = \Psi_{ident.}^i - \Psi_{pred.}^j$ is the cost difference observed by using the identified p of window i for the prediction of window j, $\Delta p = p^i - p^j$. The relative or normalized parameter sensitivity is denoted by S_p^{ij}. The sensitivity of a given p parameter can be quantified in different ways [R47], for our purposes we applied the root-mean-square metric (3.10). The effect of variability was assessed based on the BLD intervals, which means $i, j \in [1, 8]$ s.t. $i < j$. In other words, for the current prediction window only parameters identified beforehand were evaluated. The n total number of i, j pairs is 28 for the EGP, S_I and C_I parameters and 56 for the τ_D, since in the BLD case a window contains two separate meal intakes. The optimization was done by the **fmincon** algorithm of the MATLAB 2020a software package. 500 initial points were generated using the Latin hypercube sampling in order to explore large parameter space, and counteract the drawback of local optimizers.

3.2 Results of tracking intrapatient variability

During the evaluation of the results two major scenarios were distinguished. The first one was an identification of the model where the parameters were grouped based on [R24] into constant and variable categories. The second one was the evaluation of the predictive capabilities of the model and the identified parameter sets. These major scenarios were then further subdivided based on the specified number of meals a window should contain. The number of meals (and insulin boluses) were either 2, 3 or 6. A window length of 2 meals coincided with the more generally used (breakfast (B), lunch (L), dinner (D)) BLD partitioning in the literature [R48, R49].

The parameters which affects the basal glucose level are the S_I, C_I, EGP and $GEZI$, where S_I and C_I can be lumped together – if plasma insulin is not measured –, resulting

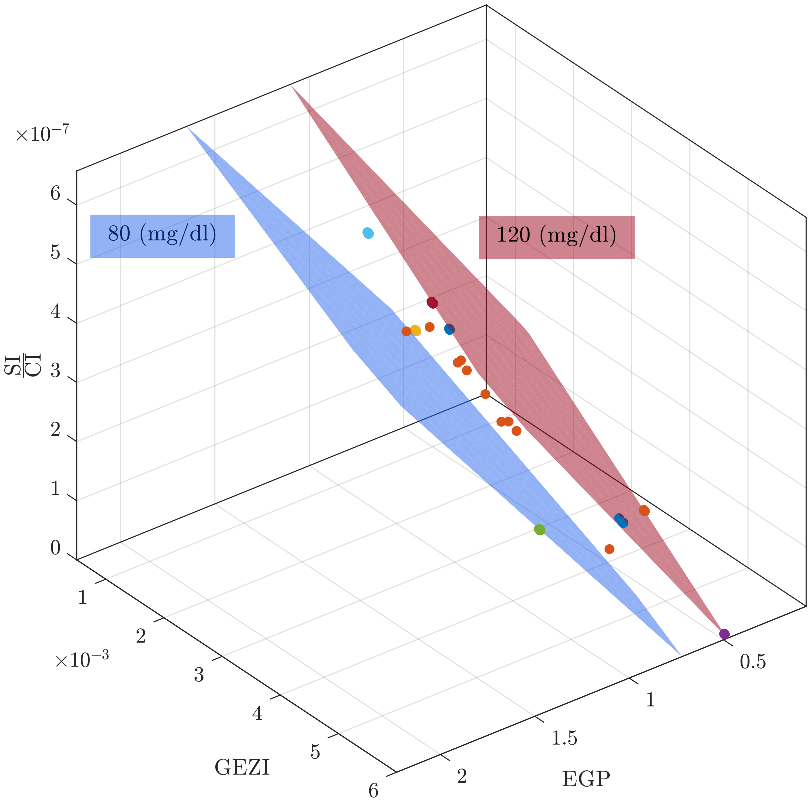

Figure 3.2: Colored points are identified parameter sets lying in the reduced parameter space constrained by the basal levels.

in three parameters overall. The nonlinear constraint restricts the feasible 3-dimensional parameter space to lie in between two planes. The planes and identified parameter sets are represented in Fig 3.2.

3.2.1 Identification scenario

In Fig. 3.3, for the identification scenario, the initial condition of a window equals to the arrival condition of the previous one. Generally, it can be stated that a good average fit was achieved, larger errors occurred around the postprandial peaks. In reality, the differences around the peaks should be even larger, since the blood-interstitial interaction acts as a low-pass filter [R50]. The accuracy has a potential limit due to the model complexity, as from the large amount of initial points the best 10-20 optimizations achieved the same RMSE, and the resulting parameters were rarely on the bounds. The identification accuracy degraded only in a modest way, when from the BLD setup the window increased to 3 meals. This indicates that with the extension of approximately 2-3 hours of the identification window the physiological variability is not major. However, stepping up to a window of 6 meals (roughly 24 hours) the accuracy degrades to a great extent, and, while the peaks on a relative term remained accurate, the trends of the baseline were missed. A lowered basal BG level and subdued peaks were observed following the second, larger session of physical activity.

In Fig. 3.4, the relative peaks quantify the glycemic state of the patient in the given interval. The relative peak was calculated by applying a typical 30 g, 3 U impulse in a steady state condition. This method gives a condensed representation, and was used for the evaluation of the intrapatient variability instead of analyzing the parameters individually. The relative peak correlates well with the inverse of the insulin sensitivity. In the morning, larger relative peaks and lower insulin sensitivity compared to L and D periods are common. This pattern of the circadian rhythm was broken between day 2 and 3, where a larger session of physical activity could cause the insulin sensitivity to raise.

3.2.2 Effect of variability on prediction

In the prediction scenario, the initial condition was set to the initial condition of the identification scenario, with the exception of G, which was the measured BG. It is important to note that during the predictive phase, future events of meal intakes and bolus insulin were considered known, since the focus was to investigate the effect of intraday variation. In Fig. 3.3, for each predicted trajectory, the parameter set of the previous window is used. This means that the constant parameters contained information from the current window and from the future windows as well, but as the constant parameters are expected to be valid for longer horizons this assumption can be made. It can be seen that two larger deviations happened in the morning period, both with the shorter horizons, which indicates that larger change in the physiology take place between the evening and morning periods. This change was attenuated with the larger windows (blue line) since it incorporates data from a longer horizon. Despite the fact that using the largest window greatly degraded the identification, this was not true for the prediction where data from a longer horizon gave attenuated behavior which was more valid on an average.

Table 3.2 gives an overview of the performance of an identified parameter set. It is visible that the lowest values in each column appear in the main diagonal, which happens because the identification results in a lower RMSE compared to using any other parameter sets from the past. The largest errors occured when an identification during the B interval was used for the prediction of the L interval. Although, this was not completely true for the last column, which can be explained by the longer session of physical activity done during the previous afternoon. These findings are coherent with Fig. 3.4.

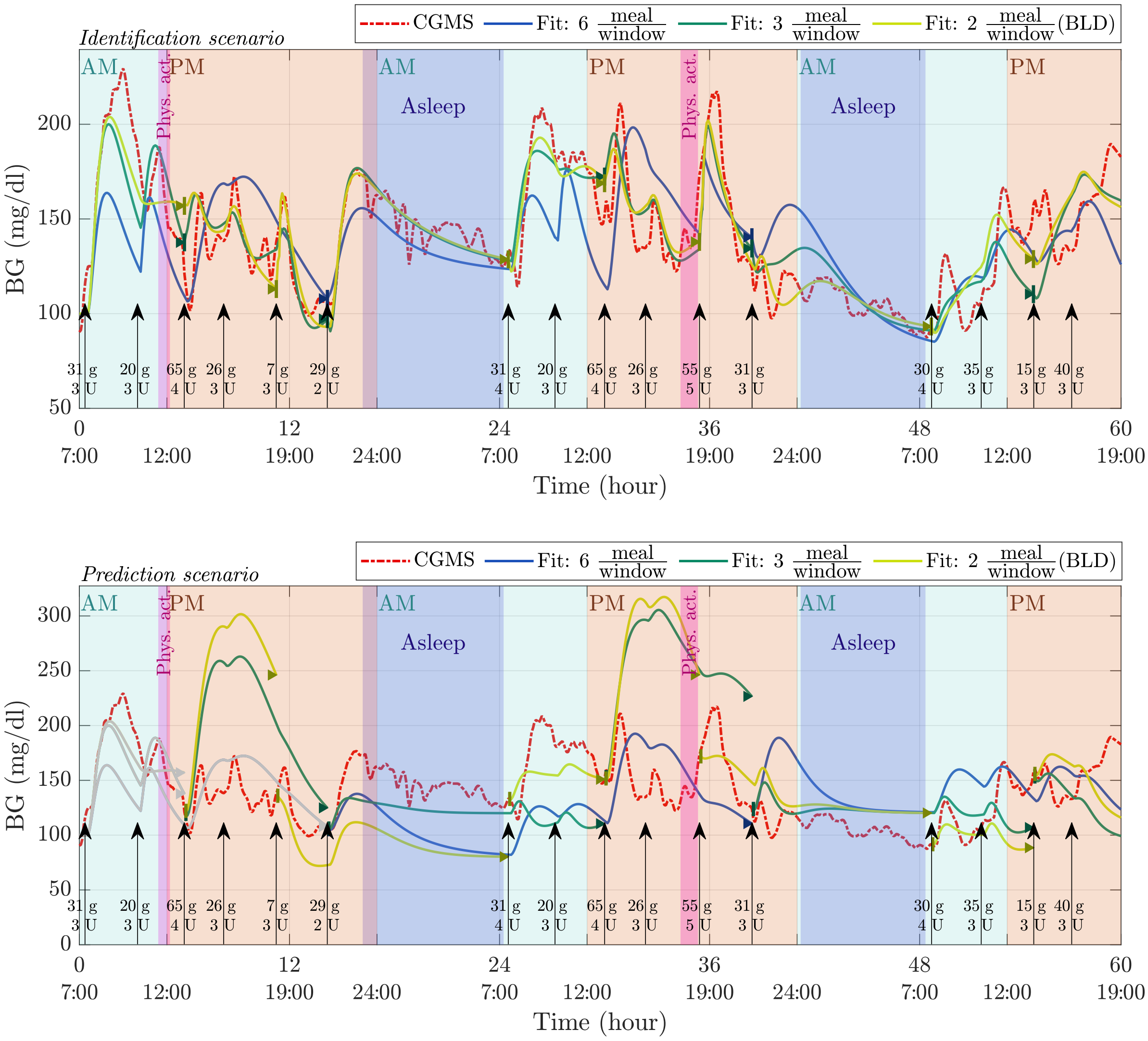

Figure 3.3: Two scenarios are depicted. In the top, the result of the identification is shown, while in the bottom, predicted BG trajectories that use the parameter set of the previous window. The measured CGMS is denoted by a dashed red line, while the simulated trajectories are highlighted by different colors depending on the window size. The grey lines in the first window of the prediction scenario indicate that the starting window is an identification, and the prediction is available in the consecutive intervals. The injected bolus insulin and meal intakes are indicated by arrows ↑. The timescale is given in a relative manner and in a 24-hour scale, as well. Four distinct periods or events are represented with different zones, namely AM, PM, Asleep and physical activity. The arrowheads ▶ indicate the endpoint of the window and the lines | indicate the start point.

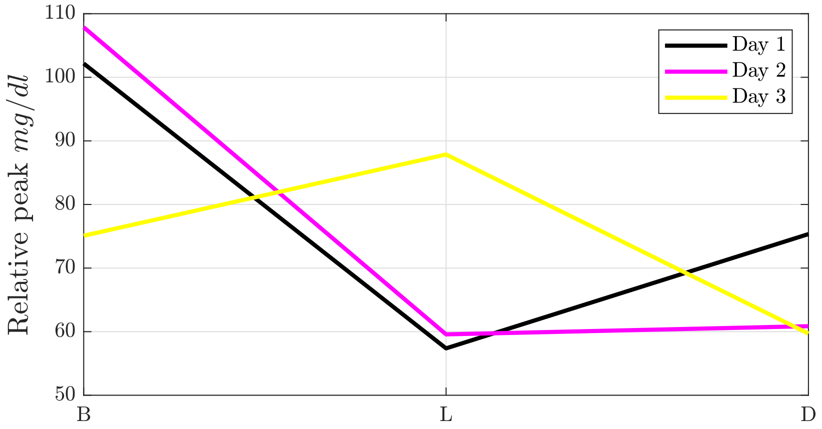

Figure 3.4: Simulated relative peak to a typical 30 g, 3 U impulse.

Pred. Id.	B	L	D	B	L	D	B	L
B	19	130	51	29	143	25	36	37
L		20	22	80	97	73	26	58
D			8	17	21	73	52	44
B				12	135	22	34	50
L					17	73	33	39
D						10	46	56
B							18	47
L								23

Table 3.2: Row Id. gives the window of identification in a consecutive way starting from the first breakfast (B), lunch (L) and dinner (D) period. The columns represent the prediction window, since during prediction only varied parameter sets from previous identifications can be used, the result is an upper triangular matrix, where the diagonal represents the RMSE mg/dl of the identification. The RMSE in the cells indicate how well the identification works on the evaluated future interval.

S_{τ_D}	S_{S_I}	S_{EGP}	S_{GEZI}
7.77	2.36	2.10	0.863

Table 3.3: Calculated parameter sensitivities with respect to the prediction error.

In Table 3.3, parameter sensitivities are given based on (3.10). It can be seen that the τ_D (the time constant related to the meal) had the largest effect on the accuracy of the prediction using previous. It indicates that not only the carbohydrate content of the meal is an important factor, but the quality of the carbohydrate as well. The insulin sensitivity S_I and the endogenous glucose production EGP had a similar effect, while the $GEZI$ had the lowest. This finding is in agreement with other studies [R20, R51], insulin sensitivity usually considered with the largest known variability.

3.3 Parameter estimation with a particular focus on endogenous glucose production

The aim of this investigation was to evaluate the fitting accuracies with respect to different complexity of the endogenous glucose production (EGP) submodel. It was the center of our work since in recent years much of the focus had been placed on intrapatient variability and the effect of physical activity [R52, R53]; endogenous glucose production is proven to be effected by both phenomena [R54, R24].

Due to the physiological effects of exercise, such as a higher chance of hypoglycaemia, researchers started to work on the implementation of physical activity into the prediction of blood glucose levels. In general, for extending models with the effects of exercise, relatively simple glucose predicting models are used, such as Hovorkas model [R20] and the Identifiable Virtual Patient (IVP) model [R55]. For instance, Jacobs and colleagues have created a hormone dosing algorithm related to exercise, where the insulin action was based on Hovorkas equations [R56]. Rashid and colleagues also extended the Hovorka model while modeling glucose-insulin dynamics in type 1 diabetes, taking into account physical activity [R57]. Hajizadeh and colleagues used the Hovorka model to create a multivariable artificial pancreas system using the estimation of plasma insulin concentration [R58]. Reenberg and colleagues created a glucagon, an exercise, and a CGM subsystem in addition to the original insulin, meal and glucose subsystem of the model [R59]. The usage of the IVP model is also common due to its compromise in effectiveness and complexity. In the first thesis we took the IVP model as a basis while designing an observer for estimating the rate of glucose appearance [R60].

Most studies use heart rate, lactate, $PAMM$ (percentage of active muscle mass) or PVO_2^{max} (maximal O_2 usage) data to define physical activity. From these, heart rate is the easiest to measure with a wearable device, such as a wrist or chest band, in contrast to the other types of data, which are more complicated to be monitored continuously during the day. Ormsbee and colleagues developed an endogenous glucose production equation in function of heart rate [R61].

We investigated the fitting accuracy on CGM measurements with respect to different endogenous glucose production submodels. The IVP model has been extended with the insulin action and with the effect of heart rate. From the simplest piecewise constant approach to the more complex insulin and heart rate dependent functions, all endogenous glucose production related parameters were assumed to possess variability during the day. Compared to previous investigations, the IVP model (3.4)-(3.1) has been modified so that the EGP is defined as a function.

3.3.1 Models of endogenous glucose production

Ormsbee and colleagues organized an exercise protocol, during which they measured lactate and heart rate levels. Using the measured lactate and heart rate data, they created an equation to estimate lactate concentration.

$$LC = \frac{\alpha \cdot HR}{(220 - HR)^{\beta}}, \tag{3.11}$$

where LC is the lactate concentration, HR is the heart rate, and the maximal heart rate was assumed to be 220 bpm. α and β parametrize the observed connection between heart rate and lactate level. The results were validated on independent literature data. They created another equation to estimate EGP levels using lactate and heart rate data from the literature.

$$EGP = \gamma \cdot HR + \delta \cdot LC, \tag{3.12}$$

where γ and δ parameters were determined based on the literature data. The calculated parameters were $\alpha = 13.25$, $\beta = 1.6$, $\gamma = 0.027$ and $\delta = 0.73$.

Using these equations we extended the original IVP model. In our model we made the following modifications. Instead of using four parameters (α, β, γ and δ) we lumped together α and δ parameters, calling them $\hat{\alpha}$. Also, instead of estimating the EGP parameter we estimated either $\hat{\alpha}$ or γ.

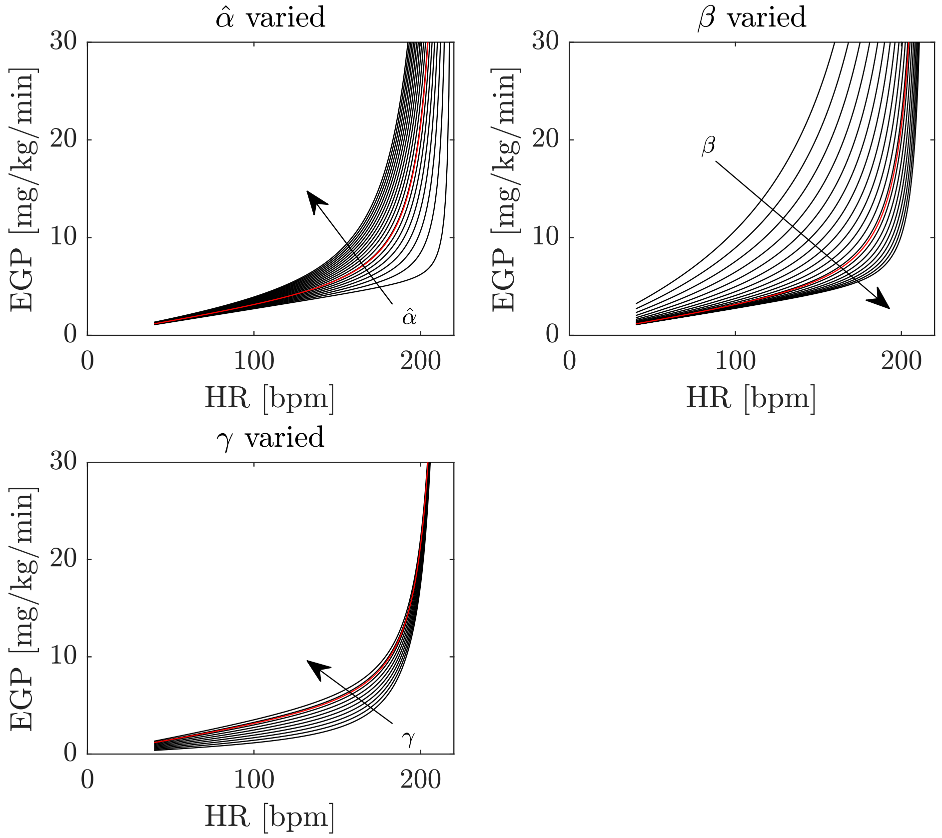

Figure 3.5: Effects of $\hat{\alpha}$, β and γ parameters on EGP. Red line represents the EGP values depending on HR, using the constant values of the parameters. Black lines show the varying EGP values when changing one parameter within the given bounds.

The unit of the EGP was converted from ($mg/kg/min$) to ($mg/dl/min$) using the body weight (BW) (kg) and the glucose distribution volume (dl) of the patient.

$$EGP = \frac{BW}{V_G} \cdot \gamma \cdot HR + \hat{\alpha} \cdot \frac{HR}{(220 - HR)^{\beta}}, \tag{3.13}$$

where $\hat{\alpha} = 9.6725$, $\beta = 1.6$ and $\gamma = 0.027$ according to the original values.

We also took into account the possibility of modeling the insulin action on the endogenous glucose production as it is used in the widely applied Hovorka model. As opposed to the deactivation and activation rate constant parametrization we used the gain (insulin sensitivity) parametrization to match the IVP model. Taking into account x_3 insulin effect, the model modifies to:

$$\boldsymbol{EGP} = EGP(1 - x_3(t)), \tag{3.14}$$

$$\dot{x}_3(t) = -\frac{1}{\tau_E} \cdot x_3(t) + \frac{1}{\tau_E} \cdot S_{IE} \cdot I_P(t), \tag{3.15}$$

where $x_3(t)$ represents the effects of insulin on endogenous glucose production, and S_{IE} is the insulin sensitivity belonging to $x_3(t)$.

3.3.2 Investigated model versions

We distinguished three possible extensions of the model: effect of insulin on the endogenous glucose production, effect of physical activity parametrized by $\hat{\alpha}$ or γ. Moreover, the joint effect of insulin and physical activity was also considered, resulting in a total number of 6 scenarios: IVP, IVP+HR$_{\hat{\alpha}}$, IVP+HR$_{\gamma}$, IVP+x_3, IVP+x_3+HR$_{\hat{\alpha}}$, IVP+x_3+HR$_{\gamma}$. The idea was to limit the number of estimated parameters; the baseline method requires the estimation of a single parameter EGP per interval to calculate the $\boldsymbol{EGP}$. A single parameter remains for the scenarios IVP+HR$_{\hat{\alpha}}$, IVP+HR$_{\gamma}$ and IVP+x_3, as well. However, the combined effect of insulin and physical activity involves the estimation of two parameters per interval. The summary for the different model versions is given in Table 3.4.

Model	**EGP**
IVP	$EGP(t)$
IVP+HR$_{\hat{\alpha}}$	$\frac{BW}{V_G} \cdot \gamma \cdot HR + \hat{\alpha}(t) \cdot \frac{HR}{(220-HR)^{\beta}}$
IVP+HR$_{\gamma}$	$\frac{BW}{V_G} \cdot \gamma(t) \cdot HR + \hat{\alpha} \cdot \frac{HR}{(220-HR)^{\beta}}$
IVP+x_3	$EGP(t)(1 - x_3(t))$
IVP+x_3+HR$_{\hat{\alpha}}$	$\big(1 - x_3(t)\big)\big(\frac{BW}{V_G} \cdot \gamma \cdot HR + \hat{\alpha}(t) \cdot \frac{HR}{(220-HR)^{\beta}}\big)$
IVP+x_3+HR$_{\gamma}$	$\big(1 - x_3(t)\big)\big(\frac{BW}{V_G} \cdot \gamma(t) \cdot HR + \hat{\alpha} \cdot \frac{HR}{(220-HR)^{\beta}}\big)$

Table 3.4: Summary of the model versions

Since we aimed to investigate the effect of the additional dynamics –not the effect of wider parameter ranges–, the upper and lower bounds of the parameters were adjusted accordingly. $\hat{\alpha}$ and γ parameters were determined to meet the condition, that the $\boldsymbol{EGP}$ stays inside the original bounds (0.062 - 2.32 mg/dl/min) at a resting heart rate of 70 bpm. Thus, the bounds for the $\hat{\alpha}$ and γ parameters were calculated based on the maximum $\overline{V_G}$ and minimum $\underline{V_G}$ values; $HR = 70$ bpm was used in these calculations.

Lower bounds of $\hat{\alpha}$ and γ:

$$0.062 < \frac{BW}{\bar{V}_G} \cdot 0.027 \cdot HR + \hat{\alpha} \cdot \frac{HR}{(220 - HR)^{1.6}}, \tag{3.16}$$

$$0.062 < \frac{BW}{\bar{V}_G} \cdot \gamma \cdot HR + 9.6725 \cdot \frac{HR}{(220 - HR)^{1.6}}. \tag{3.17}$$

Upper bounds of $\hat{\alpha}$ and γ:

$$\frac{BW}{\underline{V_G}} \cdot 0.027 \cdot HR + \hat{\alpha} \cdot \frac{HR}{(220 - HR)^{1.6}} < 2.232, \tag{3.18}$$

$$\frac{BW}{\underline{V_G}} \cdot \gamma \cdot HR + 9.6725 \cdot \frac{HR}{(220 - HR)^{1.6}} < 2.232. \tag{3.19}$$

In the Hovorka kinetics cases, τ_E had the same bounds as other insulin related time constants. The lower bound of SI_E was assumed to be the same as the lower bound of SI; however the upper bound needed to be changed. The EGP values are not allowed to decrease below zero, so the maximum value of x_3 needs to be less than one. In addition, x_3 needs to vary in the widest possible range, so that the EGP values could also be varied in a wide range. Taking these conditions into account, we assumed the upper bound of SI_E to be 0.017. Time constants of the insulin submodel was chosen to match the insulin profile of the NovoRapid [R62] rapid acting insulin, which was used during the data collection. All parameter bounds can be seen in Table 3.5. The values of the constant parameters are the following ones: $BW = 89\ (kg)$, $C_I = 1200\ (mL/min)$, $\hat{\alpha} = 9.6725$, $\beta = 1.6$ and $\gamma = 0.027$.

Parameter	***Lower bound***	***Upper bound***
τ_1, τ_2, τ_3, τ_E	30	50
V_G	100	1000
τ_D	5	60
EGP	0.062	2.232
$GEZI$	5E-4	7E-2
S_I	1.173E-4	4.224E-3
SI_E	1.173E-4	0.017
$\hat{\alpha}$: IVP+HR$_{\hat{\alpha}}$	0.5	26
$\hat{\alpha}$: IVP+x_3+HR$_{\hat{\alpha}}$	0.6	25
γ	0.007	0.032

Table 3.5: Parameter bounds

3.3.3 Parameter estimation method

The parameter estimation task was formulated as an optimization problem, where the free variables were the parameters of the mathematical model. The cost function was defined as the root-mean-square error between the simulated and the measured blood glucose trajectory. Taking into account the bounds and constraints the problem is given as:

$$\begin{aligned} \min_{\boldsymbol{p} \in \mathbb{R}^n} \quad & J(\boldsymbol{p}) = \sqrt{\frac{1}{L}\sum_{l=1}^{L}(CGM_l - G_l)^2}, \\ \text{s.t.} \quad & \boldsymbol{p} \in [\underline{\boldsymbol{p}}, \bar{\boldsymbol{p}}], \\ & 80 \leq G_B \leq 120, \\ & \boldsymbol{x}_0 = \boldsymbol{x}_B \quad \text{(Initial condition)}, \end{aligned} \tag{3.20}$$

where L is the optimization window (24 hours), because of the 5 min sampling time of the CGM it translates to 288 samples/day. G is the simulated blood glucose level, G_B and x_B are the basal glucose and steady state of the system, respectively. Lower and upper bounds of the estimated parameters are defined by $\underline{\boldsymbol{p}}$ and $\bar{\boldsymbol{p}}$. The *fmincon* [R63, R64] function carried out the optimization from 30 initial points sampled by Latin hypercube sampling ($lhsdesign$ [R63]) to counteract the drawbacks of a local search. After the optimization, the parameter set with the lowest cost was selected for further analysis.

Parameters with proven daily intrapatient variability (S_I, $\boldsymbol{EGP}$, $GEZI$) were estimated on intervals [R54, R24]. The script defined three daily intervals in an automated way such that the transitions coincide with either lunch (closest meal to 1 PM) or dinner (closest meal to 8 PM). When $\boldsymbol{EGP}$ was a function of other parameters, the independent variables were allowed to change between the intervals.

3.3.4 Results

The utilized data came from two databases. Both were generated during an approximately 3-day-long session in which blood glucose concentration and heart rate were measured. The patient was on multiple daily injection therapy and logged the carbohydrate content of the meals and insulin injections. In both cases a Medtronic Enlite© CGM sensor was applied with a sampling frequency of 5 minutes. Heart rate was measured with Mi band 5 with a sampling frequency of 1 minute. The heart rate data was resampled to a 5 minutes basis by using linear interpolation to match the sampling frequency of the CGM sensor. For the tests, we fitted the models on 5 non-overlapping days starting from 7 AM. The first two days are from the first and the last three days are from the second database.

Model	***20/09***	***21/09***	***22/10***	***23/10***	***24/10***	***avg***	***std***
IVP	14.10	13.14	11.76	18.52	11.62	13.83	2.82
IVP+HR$_{\hat{\alpha}}$	19.99	12.00	13.53	20.28	12.56	15.67	4.11
IVP+HR$_{\gamma}$	19.22	12.19	13.29	18.89	12.09	15.14	3.61
IVP+x_3	13.01	13.04	11.47	17.90	11.54	13.39	2.63
IVP+x_3+HR$_{\hat{\alpha}}$	16.36	11.72	13.04	17.89	12.08	14.22	2.75
IVP+x_3+HR$_{\gamma}$	16.19	11.70	12.85	17.31	11.89	13.99	2.59

Table 3.6: RMSE of the evaluated models, highlighted models achieved the lowest RMSE on the given estimation horizon.

Table 3.6 summarizes the root-mean-square errors (RMSE) with respect to the different days, while Fig. 3.6 and 3.7 with respect to the blood glucose level and heart rate, respectively. In most cases, taking into account the heart rate deteriorated the fitting accuracy, especially on 20/09/20. Looking at the corresponding blood glucose trajectories of 20/09/20 in Fig. 3.9, the IVP and IVP+x_3 methods underestimated the glucose when the heart rate was low and overestimated when the heart rate was higher. Since the heart rate has a direct elevatory effect on the EGP, it will modify the trajectories in a deteriorating way. The model with the effect of insulin on the EGP (IVP+x_3) achieved the lowest average RMSE and the lowest standard deviation. Comparing the estimation of the $\hat{\alpha}$ and γ parameters, the latter one yielded the lower RMSE, in two cases the lowest errors. The larger effect of γ on the EGP value at a given heart rate and the less steep slope of the function –as illustrated in Fig. 3.5– could lead to better estimation.

In Fig. 3.6, it can be observed that larger estimation error occurred at higher blood glucose concentrations independently from the applied EGP submodel and was caused by the underestimation of the postprandial peaks. It implies that the source of the inaccuracy should not be sought in the modeling of the EGP.

In Fig. 3.8m the estimated EGP values and relative postprandial peaks are illustrated. With some exceptions the insulin-dependent and heart rate dependent EGP values correlated well with the piecewise constant values. The postprandial peaks were calculated by

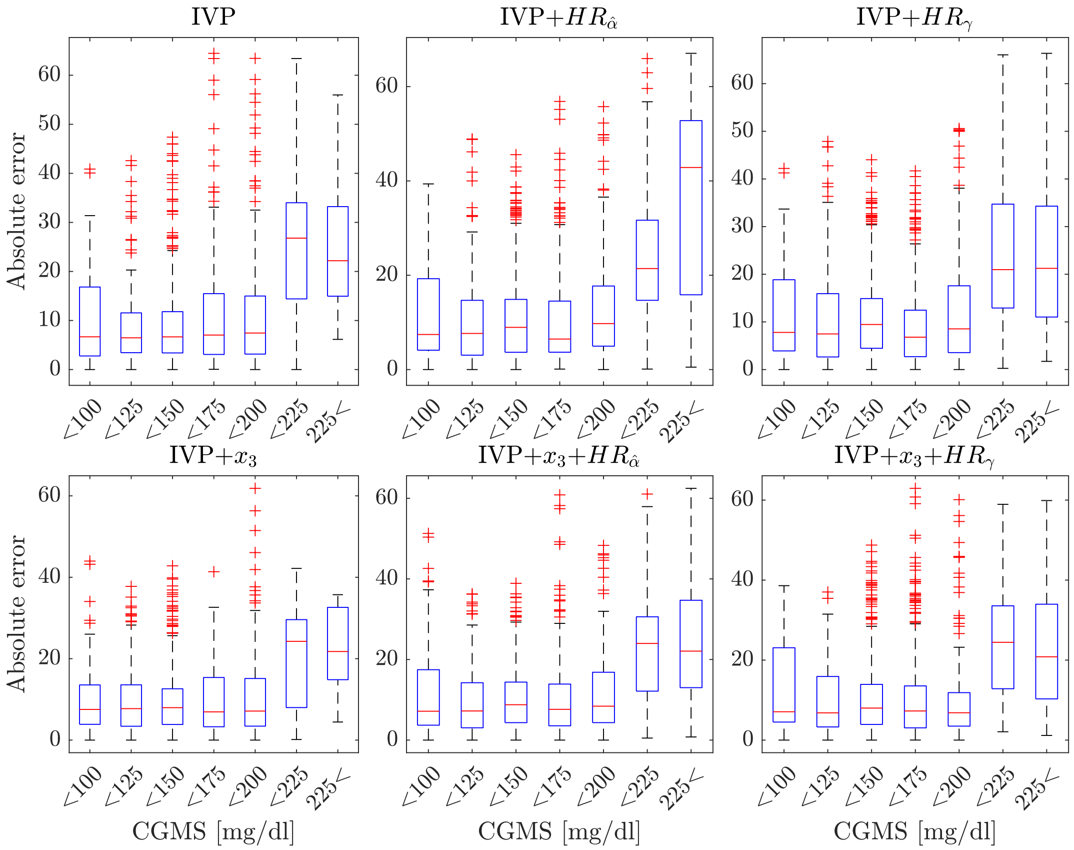

Figure 3.6: Boxplot of the absolute errors between the CGM measurements and estimated BG values with respect to the CGM values. The errors are grouped into 25 unit long ranges.

administering a 30 g of carbohydrate input and a 3 unit of insulin to the virtual patient in a steady-state condition. This metric provides a perspective of the whole behavior of the model, where the meal, insulin effect is also taken into account. It is important to compare the general behavior as well, since because of the identifiability and observability limitations seemingly different EGP trajectories can result in similar blood glucose trajectories or similar EGP values in different final trajectories. Such a situation can be seen on 21/09/20, where the EGP values in the second interval are much larger compared to the third interval however, the relative peaks are all around 30 mg/dl.

Figure 3.9 gives a general overview how the fittings change between different models, intervals and days. Overall, the modifications in the EGP term does not influence the behavior in a substantial way. There are key periods, which contribute the majority of the error to the RMSE. These discrepancies usually occur around the postprandial peak or after the depletion of the glucose coming from the carbohydrate consumption.

Results showed that the largest improvement in the fitting accuracy was achieved by taking into account the insulin action on the endogenous glucose production. In some scenarios the heart rate dependent, γ parametrized EGP could further reduce the estimation error. However, important to note that the reduction of the estimation error was minor. Compared to the piecewise constant EGP functions of the baseline IVP model, x_3 introduced two new parameters and the heart rate dependency one more parameter. The parameter bounds were chosen so that the EGP at basal conditions remains in the same range as in the piecewise constant case. The approach highlighted the effect of the insulin action and heart rate on the EGP, and mitigated the effect of the increased degree of freedom.

In light of these considerations, the piecewise constant EGP function provided a good compromise between the estimation accuracy and the number of variables. Limiting the

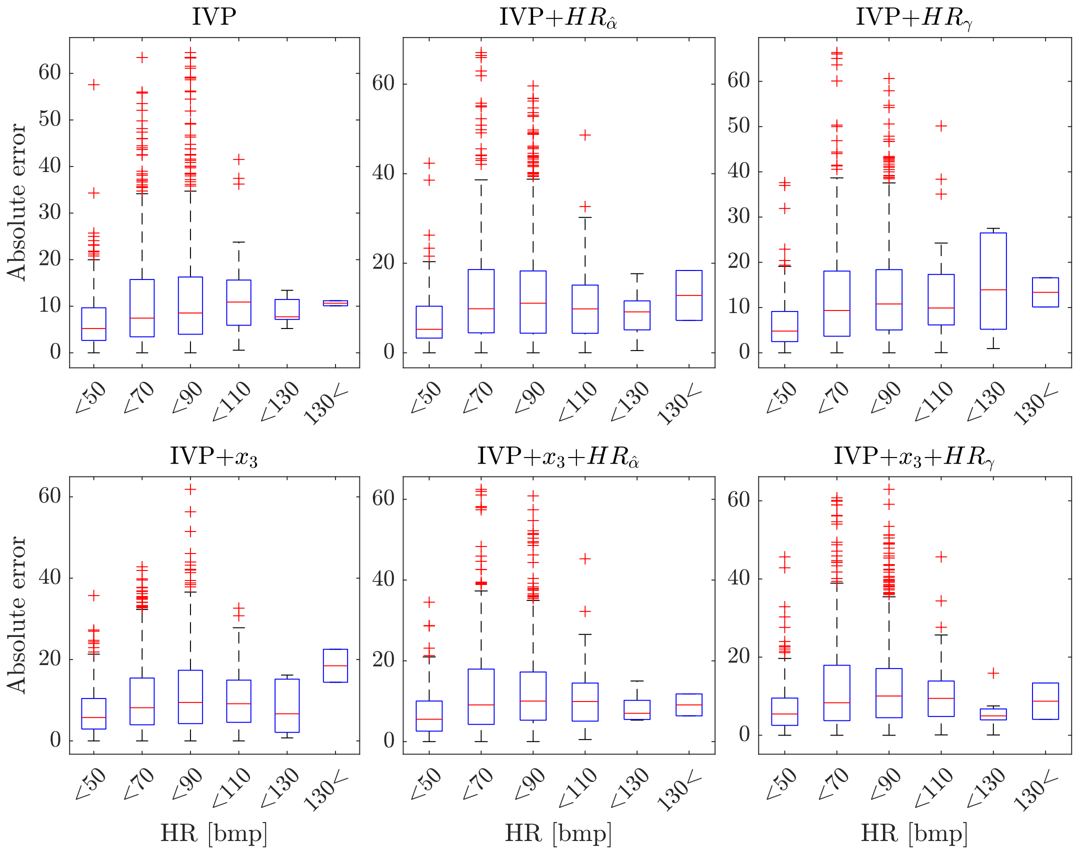

Figure 3.7: Boxplot of the absolute errors between the CGM measurements and estimated BG values with respect to the heart rate values. The errors are grouped into 20 unit long ranges.

number of free parameters is an important aspect when the model is used in the artificial pancreas system in order to mitigate the identifiability issues and improve the consistency of the parameter values between consecutive estimations. Although the results implied that the majority of the estimation error was not due to the oversimplification of the EGP submodel, they have to be taken with caution. Due to the lack of CGM measurements under 80 mg/dl, the investigated data were biased towards larger blood glucose levels and prohibited the evaluation of the models during hypoglycemic conditions. On the other hand, the heart rate measurements were biased towards the smaller values.

3.4 Meal estimation in Model Predictive Control-Moving Horizon Estimation control strategy

Over the last decade, three artificial pancreas systems gained Food and Drug Administration (FDA) approval [R4, R5, R6]. These systems can alleviate much of the burden of glucose control, improve the time spent in the target blood glucose range and the quality of life of the patients [R65, R66]. The approved systems fall into the category of hybrid closed-loop systems; it means that the system requires the announcement of the meal and an estimated carbohydrate (CHO) content. Usually, the control algorithm combines rules and a model predictive controller. The performance of the control algorithm is largely affected by the CHO counting accuracy of the patient and the accuracy of the model parameters.

Brazeau et al. [R67] assessed the CHO counting accuracy of adults with type 1 diabetes mellitus and found that the difference between the CHO content and the estimated CHO was 15.4±7.8 g. The difference was calculated between the reported value by the patient and a dietitian who used a computerized analysis program as well. Another study [R68] which focused on adolescents utilized a slightly different approach; adolescents filled the so-called PedCarbQuiz [R69] questionnaire. The authors found that 42% of the participants estimated the CHO content within 10 g of the actual value, 44% within the 10-20 g range, and 14% didn't meet the 20 g threshold. [R70] proposes a mathematical model of CHO-counting error. The model shows a tendency of underestimation of larger meals and a positive correlation between the standard deviation of the error and the meal size. The standard deviation increases from 4.78 g for meals under 20 g to 33.4 g for meals above 100 g of CHO.

Several studies investigated the performance of a fully closed-loop artificial pancreas in recent times. These studies are largely performed in the FDA approved UVa-Padova simulator [R71, R72], however clinical study has been conducted as well [R73]. A model predictive control-moving horizon estimation approach was presented and evaluated in silico in [R74] and was found to reduce the number of hypoglycemic events and result in a smoother BG trajectory. We investigated the meal estimation accuracy of an MPC-MHE strategy in silico. The investigated scenario sit between the hybrid and the fully closed-loop therapy in the sense that the announcement of the meal was assumed to be known, but no other related data. We investigated the CHO content and the time constant estimation accuracy of the meals in two setups: with and without CGM noise. We also investigated the effect of the meal estimation on the prediction accuracy, which largely determines the performance of a model predictive control scheme. By automatically estimating the meals with an acceptable error (and by knowing only the time of the meal intake), we could improve the automated artificial pancreas system and decrease the administrative load of diabetic patients.

Both the controller and the observer utilized the IVP model (3.1)-(3.5). The basal glucose level G_B is a function of 5 variables: EGP, $GEZI$, S_I, C_I and u_B which is the basal insulin infusion. During the parameter estimation process, one of the assumptions we made is that the basal glucose level was known. Furthermore, we fixed the C_I parameter to improve the consistency of the results and lower the identifiability issues. C_I and S_I are both gains of the system and cannot be identified together when the only measured variable is the BG. As physiologically EGP and S_I are easier to grasp, and physiologically relevant ranges are easier to define, we kept them as free parameters during the estimation process. The remaining variable was determined by the nonlinear constraint $GEZI > 0$ we imposed on the basal glucose level as follows:

$$GEZI = \frac{EGP}{G_B} - \frac{S_I}{C_I} u_B. \tag{3.21}$$

We extended the IVP model (3.1)-(3.5) with a CGM error model based on [R75]. The model can account for the delay [R50] – since the measurement site is the interstitium –, sensor drift, additive sensor noise and calibration error. To limit the number of factors, which affect the CHO estimation the sensor drift has been omitted. The sensor delay was modeled as an additional interstitial glucose compartment IG, while the additive noise was an autoregressive process of order two with a white noise term $w \sim \mathcal{N}(0, \sigma^2)$ as follows:

$$\dot{IG}(t) = -\frac{1}{\tau_{IG}} IG(t) + \frac{1}{\tau_{IG}} G(t), \tag{3.22}$$

$$v(t) = \alpha_1 v(t - T_s) + \alpha_2 v(t - 2T_s) + w(t), \tag{3.23}$$

$$CGM(t) = IG(t) + v(t), \tag{3.24}$$

where τ_{IG} is a time constant characterizing the transfer between the blood and the interstitial glucose, while α_1 and α_2 define the autoregressive process.

3.4.1 Moving horizon estimation

A moving horizon estimation based observer has been developed with the purpose of providing estimated initial state, patient parameters and CHO for the MPC. The observer ran in a sliding window every 5 minutes, in accordance with new CGM measurements. The method was based on a constrained optimization where a cost function was minimized. The cost function was defined to be the root-mean-square error between the estimated trajectory of the blood glucose and the CGM values of the last 24 hours:

$$\begin{aligned} \min_{\boldsymbol{p} \in \mathbb{R}^n} \quad & J(\boldsymbol{p}; t_k) = \sqrt{\frac{1}{L} \sum_{l=k-L}^{k} (CGM_l - G_l)^2} \\ \text{s.t.} \quad & \boldsymbol{p} \in [\underline{\boldsymbol{p}}, \bar{\boldsymbol{p}}], \\ & GEZI \geq 0, \\ & \boldsymbol{x}_0 = \boldsymbol{x}_B \quad \text{(Initial condition)}, \end{aligned} \tag{3.25}$$

where L is the sliding window length, t_k is the current time instance, $\boldsymbol{p} = [S_I, EGP, \boldsymbol{d}, \boldsymbol{\tau_D}]$ is the vector of free parameters during the current optimization horizon, k is the discrete step using the forward Euler method. The number of free variables n depends on the number of meals in the current window. The initial condition of the state vector $\boldsymbol{x}_0$ is defined as the steady-state of the system assuming that $d_0 = 0$ and $u_0 = u_B$.

The optimization was done using the differential evolution method of the SciPy library. The differential evolution algorithm ran until a termination criterion of accuracy or a maximum number of iterations was achieved.

3.4.2 Closed-loop simulation scenario

After the 2-day-long open-loop session (manual insulin dosing), the closed-loop setup automatically administered the insulin to the virtual patient for an extra two days. The open-loop session was needed to provide historical data for initial patient parameter estimation. On this initial horizon, the patient was assumed to be on a multiple daily injection regimen, meaning long-acting insulin was taken into account as a basal insulin level, and boluses were injected to compensate for the pandrial peaks. After the 48-hour-long initialization horizon, the closed-loop strategy took over control and administered micro boluses every 5 minutes virtually. The meal estimation accuracy was evaluated on the closed-loop session, which consisted of meals between 10 to 80 g of CHO and peak times of absorption between 15 and 60 min. Two meal schemes have been defined and used in the following pattern: Meal scheme 1, Meal scheme 2 during the multiple daily injection therapy and Meal scheme 2, Meal scheme 1 during the closed-loop therapy as it can be seen in Fig. 3.10.

The patient parameters of the virtual patient were the arithmetic mean of the virtual cohort published in [R24].

3.5 Results of the meal estimation

In Fig. 3.10, the full horizon is depicted. The simulation started with a 2-day-long multiple daily injection therapy where the injections were defined manually. After the initialization, the MPC determined the control insulin (plotted in solid green line) in each iteration based on the estimated CHO and patient parameters. The magnitudes of the arrows (injections) are proportional to the values of the continuous infusion therapy. The solid red line depicts the simulated CGM trajectory, while the black dashed line the corresponding BG level of the virtual patient.

Under the BG trajectories, the orange and magenta curves represent the 1-step-ahead prediction error of the MPC during the optimization. The magnitudes of the errors imply the overall estimation accuracy of the MHE. It can be seen that at the time of a given meal consumption, the prediction error usually abruptly increased, and as new measurements were being made, the error decreased. This phenomenon was more noticeable without CGM noise. When the noise perturbed the BG trajectory practical identifiability has to be taken into account; during the MHE optimization, local minima appear as the same or very similar root-mean-square errors can be achieved with different trajectories (and patient parameter sets). Despite these different parameter sets can result in very similar errors, they can significantly alter the predicted BG values.

The controller achieved similar performance regardless of the CGM noise, slightly lower peaks and safer minimum values could be observed without the CGM noise, depicted by the solid purple line in Fig. 3.10. Similarly, the root-mean-square-error to the nominal BG value of 115 mg/dl showed no significant difference between the two trajectories (32.45 with CGM noise, 31.85 without). During the 2-day-long manual therapy we used a total of 72 units of insulin, while 80 during the closed-loop therapy.

In Fig. 3.11, the CHO content and time constant estimation errors are plotted as a function of time (relative to the consumption of the meal). The data were aggregated in half-hour steps for evaluation. It can be seen that the median estimation error drops drastically for both parameters in the first 2 hours. Regardless of the CGM noise, the errors were of similar magnitudes throughout the evaluated 8-hour-long horizon; in fact, the error samples come from the same distribution based on the two-sample Kolmogorov-Smirnov test (with a mean p-value of 0.6), even if aggregated in 15-minute-long steps.

In Fig. 3.12, the horizontal axes represent the normalized error ($\frac{p-p_{ref}}{p_{ref}}$) in the estimated parameters: CHO content and time constant. The vertical axes denote the 1-step-ahead prediction error: ($\hat{G}_{l+1} - G_{l+1}$). An important aspect of the time constant estimation is that while during the first half-hour the prediction and the estimation error had a negative regression coefficient (-0.32 and -0.14), over 30 minutes the coefficients were positive (2.15 and 2.53). This means that underestimation of the time constant during the early stages makes the MPC anticipate quicker absorption, hence larger peaks. Over 30 minutes the effect is the opposite. Overestimated meals – that otherwise have been already absorbed – make the MPC anticipate absorption over extended periods of time.

Despite the fact that we observed no statistically significant differences in the distributions of the estimation errors, the prediction errors differed greatly in the regression coefficients (1.03 vs 3.95 and 1.93 vs 6.00). The increased prediction errors – despite the similar CHO and time constant estimation error – indicate that the deterioration of the prediction accuracy originates from the estimation of other (patient) parameters.

While on a distribution level, the CGM did not introduce significant differences in the meal estimation; in specific cases, the detrimental effect of the noise could appear. The outliers of the τ_D estimation in Fig. 3.12 corresponds to the 10 g meal of the Meal scheme 2. The large estimation error can be explained based on the difference between the CGM noise (red solidline) and the reference BG (dashed black line) in Fig. 3.10. For small meals, it can occur that the magnitude of the postprandial peak falls into the range of the CGM noise, and the resulting trajectory makes the time constant estimation unreliable.

3.6 Numba-accelerated parameter estimation and simulation functions

Optimization algorithms are a main focus of scientific computing. It is also heavily used in control engineering and more specifically in artificial pancreas applications [R76]. Two areas where optimization problem rises: input signal calculation and parameter estimation. We focused on the latter problem, where the task is to find some combination of the parameters of the mathematical model, which accurately describes the behavior of the process and meets additional constraints. In recent years, general-purpose computing on GPUs have been widely applied for optimization algorithms [R77, R78, R79].

Usually, these problems consist of the integration of nonlinear mathematical models, applying linear or nonlinear constraints, and a large number of parameters. Often due to these facts population-based optimization algorithms are employed such as the differential evolution [R80, R81]. A key feature of population-based strategies is that they usually slower to converge, but able to explore larger spaces and can be efficiently parallelized.

Despite the widely accepted notion of being "slow", Python is the most popular programming language in data science and scientific computing [R82]. Usually, Python makes up for the longer runtimes by sparing compilation and code development times. However, there are cases where raw speed is required. In such situations, Numba [R83] aims to provide a solution by converting Python code into fast machine code. With minor modifications in the syntax, the computationally heavy functions can be transferred to parallelized machine code deployed either on the CPU or the GPU.

We showcased the performance differences in a parameter estimation task between general Python syntax, Numba-accelerated code on CPU and GPU. In the case of the general Python syntax, NumPy [R84] library was used where the array operation could be accelerated with it, and the differential evolution algorithm of the SciPy [R85] library was used as the optimization algorithm. In all cases, the most frequently used methods were the forward Euler method in order to simulate the blood glucose trajectories, and the exponential decay impulse response of the meal inputs. Runtimes were evaluated and compared on different cloud computing platforms (Google Colab [R86] and Gradient [R87]) and a PC laptop to provide a more general view on the performance differences.

The simulation of the blood glucose trajectories was separated into two functions to speed up the calculations: the meal impulse response function (3.5) calculated the R_A term, while the cost function simulated the blood glucose trajectories and calculated the root-mean-square error. Besides, the population evolution step was also accelerated compared to the SciPy library, which was utilized by the general Python syntax version. The implemented differential evolution algorithm was based on [R88] with "best1bin" strategy; the same settings were applied in the SciPy function as well.

3.6.1 Meal impulse response

The meal impulse response function calculates the R_A term for each patient for each discrete timepoint as given in (3.5). The calculation can be greatly parallelized as a single thread can be responsible for the calculation of the resulting 2-dimensional R_A matrix as illustrated in Fig. 3.13.

where N is the number of meal intakes during the horizon, typically around 5 for a 24-hour-long estimation window, i is the index of the individual in the population, $t_n(t_k)$ defines the time past since the n-th meal intake in the t_k discrete timepoint. The optimized parameters in the function are the V_G and τ_D.

In order to fully utilize the GPU, input arrays were converted to single-precision floating-point format, and the global memory access patterns of the elements: V_{G_i}, $\tau_{D_{n,i}}$, $t_n(t_k)$ and

Algorithm 1 Meal impulse response

```
$\sum R_A = 0$
for $n = 1, 2, \ldots, N$ do
    $R_{A_n} = \frac{d_n}{V_{G_i} \cdot \tau^2_{D_{n,i}}} \cdot t_n(t_k) \cdot e^{-\frac{t_n(t_k)}{\tau_{D_{n,i}}}}$
    $\sum R_A = \sum R_A + R_{A_n}$
end for
$R_A(t_k, i) = \sum R_A$
```

d_n to coalesced. The latter one was ensured by making the horizontal dimension of the arrays (population sizes) multiples of 32 and converting the arrays to "C-contiguous". For monitoring GPU occupancy, memory accesses and kernel optimization purposes Nvidia Nsight Compute was used [R89].

3.6.2 Cost function

The cost function solves the differential equations on the simulated horizon and calculated the root-mean-square error between the measured and the simulated blood glucose trajectories as:

$$
\begin{aligned}
\min_{\boldsymbol{p} \in \mathbb{R}^n} \quad & J(\boldsymbol{p}; t_k) = \sqrt{\frac{1}{L} \sum_{l=k-L}^{k} (CGM_l - G_l)^2} \\
\text{s.t.} \quad & \boldsymbol{p} \in [\underline{\boldsymbol{p}}, \bar{\boldsymbol{p}}], \\
& \boldsymbol{x}_0 = \boldsymbol{x}_B \quad \text{(Initial condition)},
\end{aligned}
\tag{3.26}
$$

where L is the optimization horizon, $\underline{\boldsymbol{p}}$ and $\bar{\boldsymbol{p}}$ are lower and upper bounds of the free variables and $\boldsymbol{x}_B$ is the steady-state of the system.

Algorithm 2 Cost function

```
$J(i) = 0$
for $l = k - L, k - L + 1, \ldots, k$ do
    $\mathbf{x}(t_{l+1}) = \mathbf{x}(t_l) + \Delta T \cdot \dot{\mathbf{x}}(t_{l+1})$
    $J(i) = J(i) + (G(t_{l+1}) - CGM(t_{l+1}))^2$
end for
$J(i) = \sqrt{J(i)/L}$
```

where $\mathbf{x} = [G, I_{EFF}, I_p, I_{sc}]$ is the state variable and $J(i)$ is the corresponding cost of the i-th individual in the population.

3.7 Results with the accelerated functions

Runtimes were evaluated by running the differential evolution algorithm for 100 generations with different population sizes, and the whole optimization was repeated 10 times to get an average runtime. In all CPU cases, multi-threaded calculations were used. Two additional factors were excluded: compilation time which affects the Numba-accelerated functions and the spawning of multiple processes in the SciPy library which affects the general Python syntax runtime.

In Fig. 3.14, total runtimes and the runtimes of the parallelized functions are given with respect to environments with different specifications. The total runtime includes general Python syntax code and host-to-device transfer times as well. The complete Python syntax implementation was evaluated solely on the PC Laptop setup, which had the highest computing performance in terms of the CPU. The Numba just-in-time (JIT) compiled CPU runtime was approximately two orders of magnitude shorter (when evaluated on the same CPU), and slower CPUs still greatly outperform the general syntax when using the Numba JIT compiled functions.

Comparing the performance of the JIT compiled CPU and GPU runtimes larger variance can be seen in terms of the CPU performances; large difference in terms of threads (2 vs 12 for the Colab and PC, respectively) and clock speeds (2.2 vs 4.0 GHz) explain the variance.

Between the total runtime, meal impulse response, and cost function, the largest improvement was achieved in the meal impulse response. The reason for the one order of magnitude acceleration even at low population sizes was due to the fact that two levels of a three-level nested for loop can be parallelized, and each thread on the GPU can be assigned to calculate a single element in a 2-dimensional matrix. For the cost function, the acceleration was prevalent only for large population sizes, as it involves a single for loop; GPU versions outperform their CPU counterpart above a population size of 3000. The calculation of the cost function was not compute-heavy enough for small population sizes, as the GPUs can yielded almost the same runtime in the range of 128 to 3000.

In Fig. 3.15, the ratios of the CPU and GPU runtimes are illustrated with respect to the environments. The slightest advantage of using a GPU over the CPU is on the PC laptop. On the cloud computing platforms the ratio was larger and the GPU outperformed the CPU version for smaller population sizes. It can be seen that for larger population sizes, depending on the environment a speed-up of 2 to 8 times can be achieved using the GPU.

3.8 Thesis summary

Findings in my first thesis led to the conclusion that the structure of the mathematical model and the accuracy of the patient parameters can have greater impact on the estimation accuracy than the state observer algorithm itself. Thus, I focused on parameter estimation methods, with a particular focus on constraining the free parameter space to improve the speed, convergence and consistency. Also, the estimated parameters can be of great use in various applications such as blood glucose prediction, replaying different insulin and meal scenarios, also observing daily or long-term trends in insulin sensitivity. The method and its use-cases fall under the umbrella of digital twins. In [C3], I developed moving horizon estimation based methodology to track intrapatient variability. In [C4], the focus was on the estimation of the endgenous glucose production and extending the model with heart rate as a potential, easy-to-access parameter to describe physical activity. In [C5], the estimation algorithm was extended with a model predictive controller and its performance was evaluated in a simulation environment. In [C6], I optimized the parameter estimation algorithm for tackling large populations as a cloud-based service.

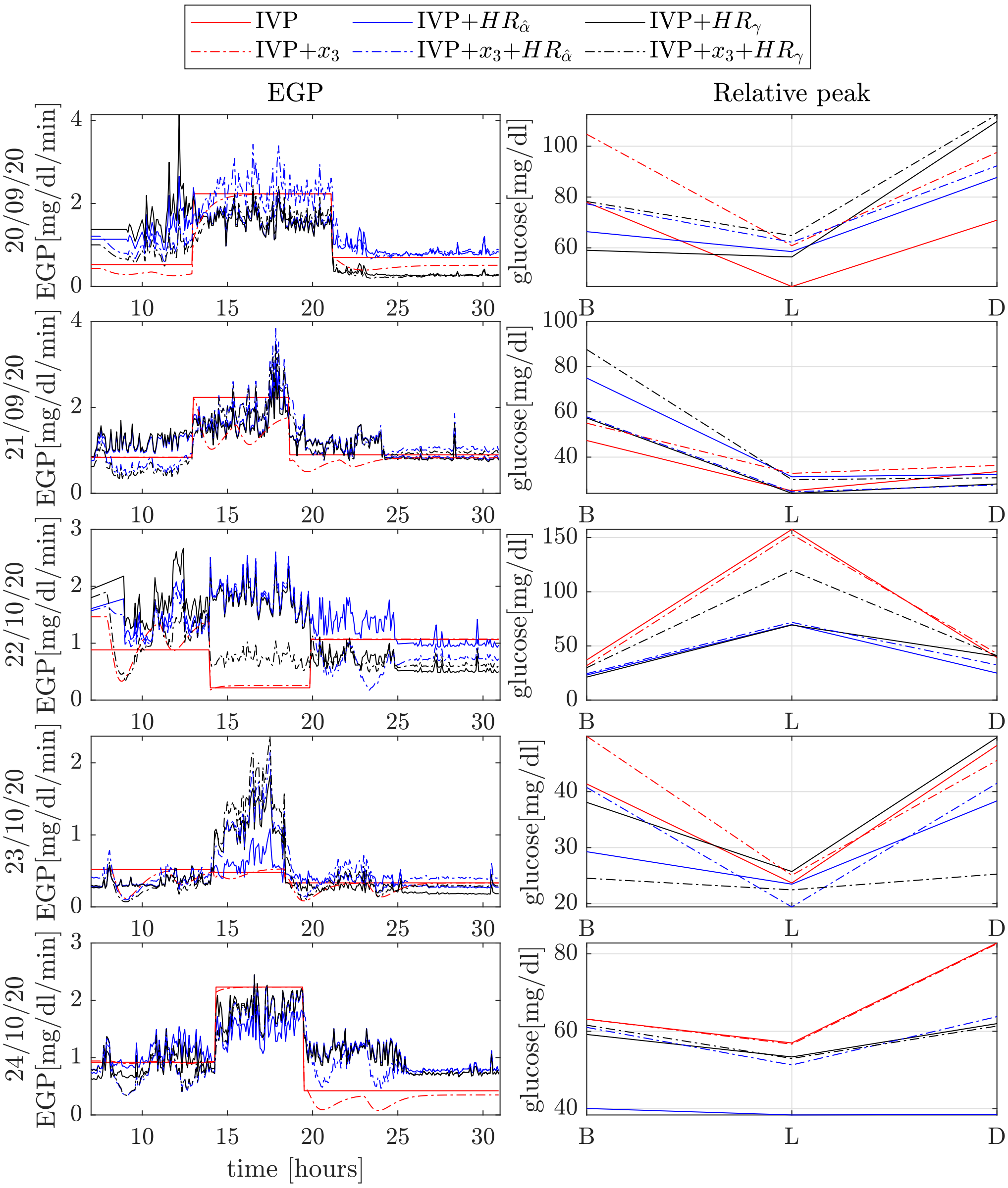

Figure 3.8: The left column visualize the EGP values of the different models across the estimation horizons. The right column illustrates the relative postprandial peak during the breakfast (B), lunch (L) and dinner (D) periods. Each row represents a specific day from the applied database.

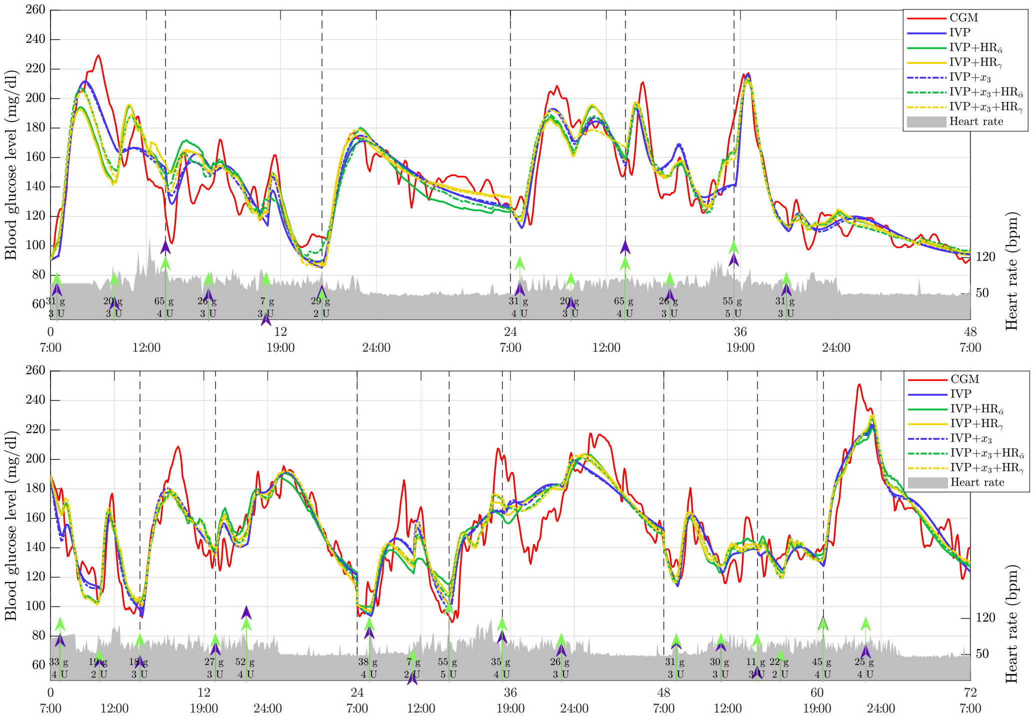

Figure 3.9: Two days of data from the first (upper) and three days of data from the second (lower) measurement session. Measured BG level is plotted in a solid red line. The estimated trajectories of the different models are represented with different colors. The timepoint of the carbohydrate consumptions and insulin injections are given by the purple and green arrows, respectively. The measured heart rate is illustrated by the grey area.

Figure 3.10: Summary of the control with the defined multiple daily injection therapy and with the closed-loop therapy on the full simulation horizon. The upper plot represents the simulated BG trajectories, where the green arrows represent the insulin injections, the purple arrows the meals, and the continuous green line is the insulin infusion. The lower plot depicts the 1-step-ahead prediction errors with and without CGM noise.

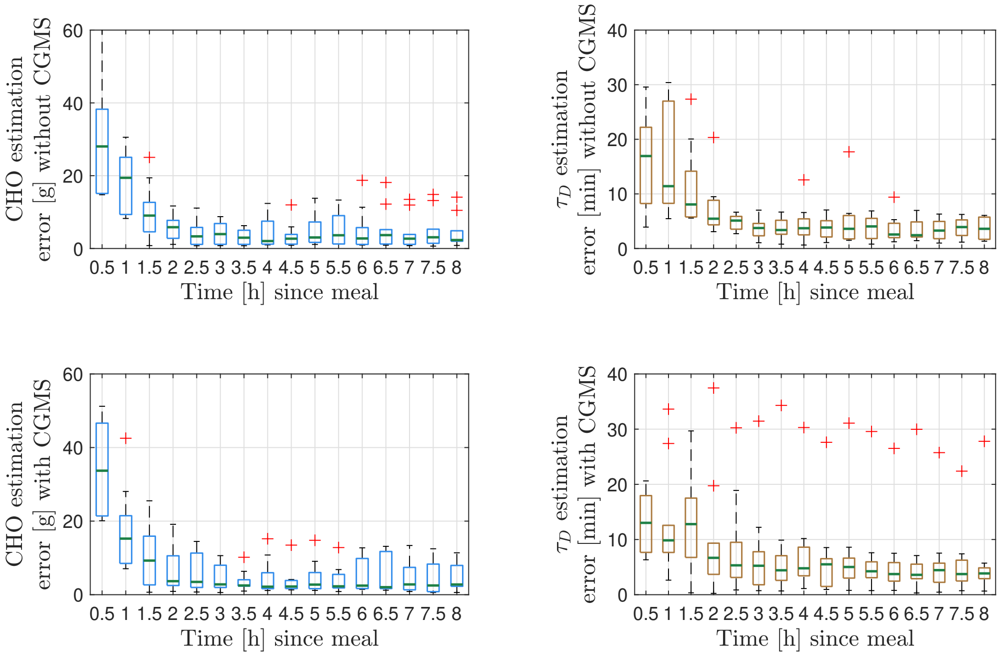

Figure 3.11: Aggregated estimation errors of the CHO content and time constants with respect to the time passed since the consumption of the meal.

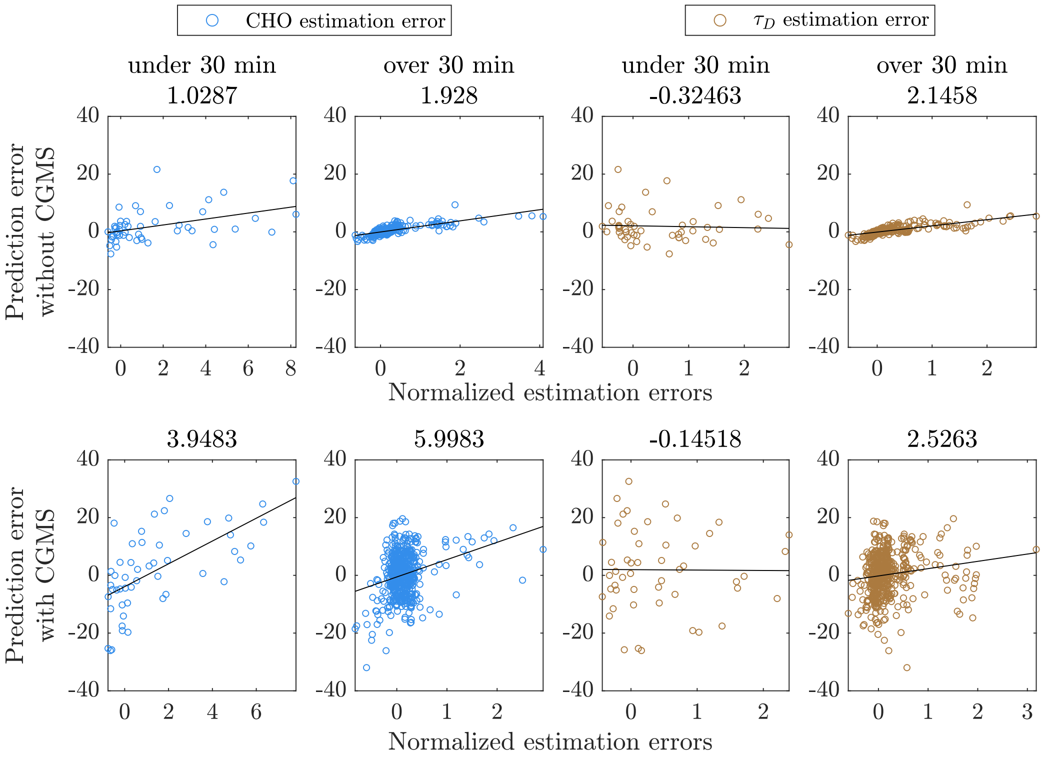

Figure 3.12: 1-step-ahead prediction errors are plotted as a function of the normalized errors in the CHO and time constant estimations. The short-range and long-range estimations (with a threshold of 30 minutes) are separated into different subplots. The β numbers are the regression coefficients.

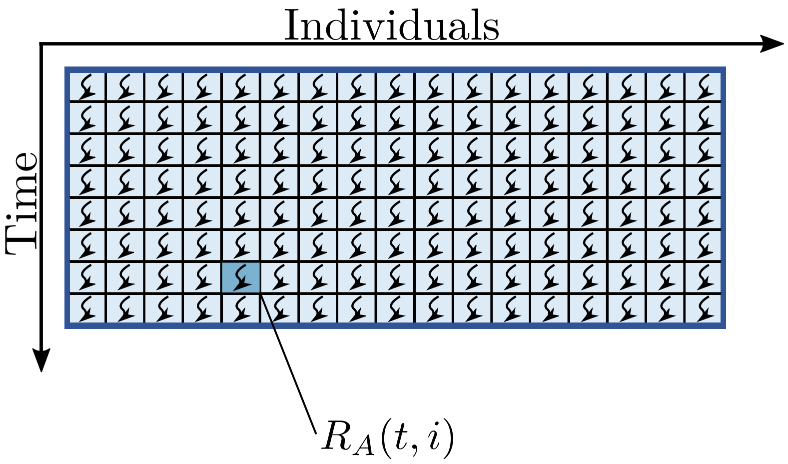

Figure 3.13: 2D result array of the meal impulse response function.

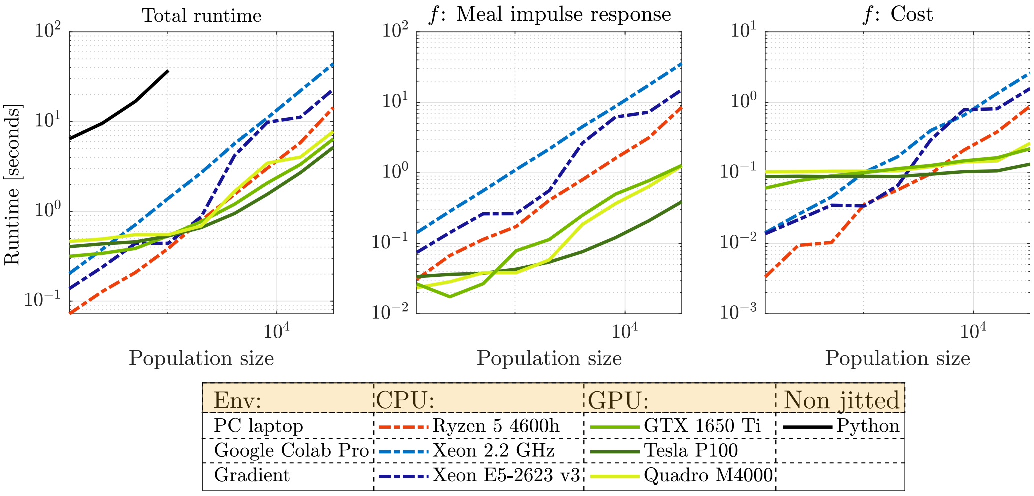

Figure 3.14: Total runtimes and the runtimes of the parallelized functions are given for different environments.

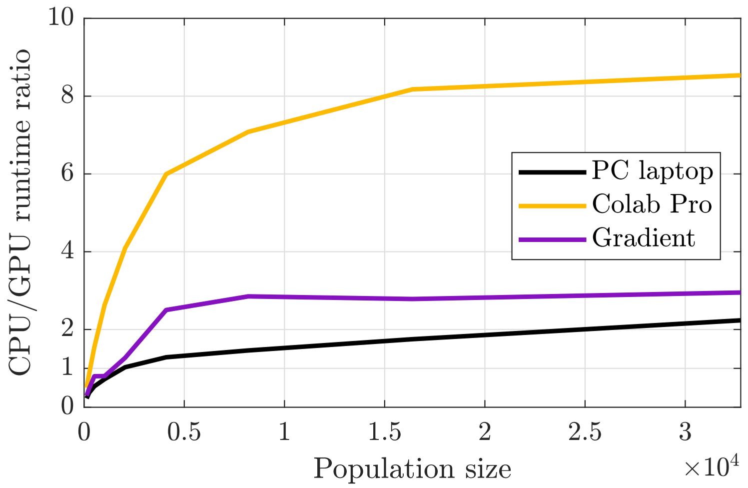

Figure 3.15: Ratio of the CPU and GPU runtimes are given for the Numba JIT compiled functions for different environments.

4

Time Varied Illumination Speckle Contrast Imaging

Thesis group 3: Time varied illumination in laser speckle contrast imaging

Thesis 3
I contributed to the theory of laser speckle contrast imaging by modeling the effect of varying laser illumination. I contributed to the validation through simulations and in vivo experiments. I contributed to the real-time implementation of the time varied illumination methodology.

Thesis 3.1
I developed a mathematical model which describes the speckle contrast with regards to the varying, modulated laser illumination. I generalized a well-known model which assumed constant illumination.

Thesis 3.2
I validated the model of varied illumination by fitting it to invitro and invivo measurements.

Thesis 3.3
I implemented the time varied laser speckle contrast imaging on a Raspberry Pi coupled with a Basler camera. The system was able to optimize the laser illumination in real-time.

Publications relevant to the theses: [J3, J4].

4.1 Time Varied Illumination Speckle Contrast Imaging Model

Laser Speckle Contrast Imaging (LSCI) is an optical technique that has been widely used for monitoring disease induced blood flow changes on the brain surface [R90, R91], skin [R92], surgery situation [R93] or even retina [R94]. It has a large field of view, paired with high spatial and temporal resolution, and it requires no contrast agent, which makes it an ideal choice for flowmetry. LSCI is based on the dynamic light scattering of coherent light illumination. Laser speckles can be observed when an illuminated medium scatteres the light in a way that it produces a random interference pattern from the superposition of phase fluctuations. As the pattern changes in accordance with the movement of the scatterers, the decorrelation of such patterns can be used to determine the flow rate of blood.

The first description of Laser Speckle Imaging and blood flowmetry was published as early as 1981 [R95]. Ever since the technique has been improved greatly. Temporal analysis can help to reduce the time-invariant noise and static scattering [R90]. Multi-exposure methods [R96, R97] were developed to increase the dynamic range of the measurements and for static scattering elimination. Multi-exposure method and its variants use multiple exposure times with constant light intensity to estimate the correlation time of speckles algorithmically and thus the flow rate. To suppress measurement noise and remove static scattering with the aim of obtaining true flow speckle contrast and flow speed, LSCI system calibrations and calculation procedures were proposed [R98, R99]. In order to balance the temporal and spatial resolution, and speckle versus pixel size ratio various solutions have been published [R100, R101]. Recently, in [R102], a high-speed camera enabled imaging method was presented for wide-field measurement of the speckle temporal intensity autocorrelation function.

For the quantification of speckle contrast, usually the variance of intensity is normalized by the mean intensity in local spatial or temporal windows. This contrast is than used to calculate the speckle autocorrelation (correlation time). The common methodology is the following:

$$\kappa = \frac{\sigma_s}{\langle I \rangle}, \tag{4.1}$$

where κ is the calculated contrast from the image, σ is the standard deviation and $\langle I \rangle$ is the mean light intensity over a window of pixels on the image or sequence of images. Relative flow can be then estimated using (4.1), as the decorrelation increases with the flow rate and hence κ is larger at smaller velocities and vice versa. The normalized second order model of the underlying physical model was presented in [R103] as:

$$\upsilon_2(T) = \frac{\beta}{T^2} \int_0^T \int_0^T \rho |g_1^n(t' - t'')|^2 + (1-\rho)|g_1^n(t' - t'')| dt' dt'', \tag{4.2}$$

where υ_2 is the reduced second moment, T is the exposure time, ρ is the fluctuating component fraction and $(1-\rho)$ is the statically scattered ratio, and $t' - t''$ give the time differences during the exposure. The constant β is a normalization factor depending on the speckle size, detector size and additional factors of the experimental setup. g_1 is the electric field autocorrelation [R95] which according to [R102] gives us $g_1^n(t) = exp(-(t/\tau_c)^n)$, where τ_c is the correlation time. The value of n depends on the type of flow dynamics. In case of small arteries/veins in the size range of ≈30 to 150 μm with single scattering unordered motion (SU) or multiple scattering ordered motion regime (MO) $n = 1$. For multiple scattering unordered motion (MU) representing the behavior of capillary perfused tissue (i.e. parenchyma) $n = 0.5$, while $n = 2$ describes single scattering from ordered motion for larger vessels (SO). In transition situations, these dynamics $(g_1^{0.5}, g_1^1, g_1^2)$ are weighted accordingly extending (4.2). The speckle contrast (4.1) can be used to identify τ_c and other parameters by modeling $\kappa(T, \tau_c)$ and $\sqrt{\upsilon_2(T, \tau_c)}$ equivalency.

The standard LSCI methods have the assumption that the light intensity does not change throughout the exposure time. Note, this holds for the multi-exposure methods [R96] technique, its derivatives, and for single-shot acquisition multi-exposure methods with a high frame rate single-photon avalanche diode camera speckle imaging [R97] as well. In these methods, constant average laser intensity is used within an exposure.

In order to model the varying laser intensity during a single exposure, we generalized

(4.2) by defining $I(t)$ as time dependent illumination intensity:

$$\upsilon_2(T) = \frac{\beta}{\int_0^T\int_0^T I(t')I(t'')dt'dt''} \int_0^T\int_0^T I(t')I(t'')g^{\rho,n}(t'-t'')dt'dt'', \tag{4.3}$$

where $I(t')$ and $I(t'')$ are the laser intensities at the sample at time instant t' and t'', and for better readability the complex relation including scattering and flow dynamics is substituted as $g^{\rho,n}(t'-t'') = \rho|g_1^n(t'-t'')|^2 + (1-\rho)|g_1^n(t'-t'')|$ for non-transition dynamics [R102]. The description of the equation intuitively is the following: the decorrelation is weighted with the intensity levels, which can be transformed to be dependent on the time lag by calculating the correlation function. By applying integration once in (4.3) the reduced second moment becomes:

$$\upsilon_2(T) = \frac{\beta}{\int_0^T R_{II}(t)dt} \int_0^T R_{II}(t)g^{\rho,n}(t)dt, \tag{4.4}$$

where $R_{II}(t)$ is the autocorrelation of $I(t)$. Note, that selecting $I(t) = const.$ the $R_{II}(t)$ and the denominator integral reduce to the well known $(1 - t/T)$ and $2/T$ formulas. This equation can be used to derive various contrast to speckle correlation time relation in an efficient way.

We propose as the most advantageous usage of changing illumination profile to be a decreasing valued function. Meaning, a short bright period with decreasing brightness afterwards continuously or in discrete steps. The idea behind is similar to multi-exposure concept, maintaining the average brightness for increasing exposure times. Thus, various τ_c periods are captured with $\propto 1/\tau_c$ intensity and $\propto \tau_c$ observation time. The significant difference from the multiple exposures is that the speckle decorrelation phenomena is continuously observed and is not separated into time segments.

Our proposed method – similar to the standard speckle contrast imaging – gives valid result under the assumption that, except for the varying intensity, the critical laser properties are maintained such as coherence length, wavelength, noise performance during exposure. In lieu of the limited and usually expensive analog modulation schemes (e.g. laser current modulation, micro-opto-electro-mechanical systems or micromirror array, Bragg cell), we rely on binary intensity modulation of finite pulse time resolution and constant intensity.

The pulse coding enables wider average intensity range to be covered, and at the same time the calibration of the nonlinear characteristics of continuous modulation can be avoided. Given high enough pulse rate and sharp pulse skew, various modulation techniques such as pulse width, position, code or delta modulation can be applied to tailor the speckle contrast and correlation time relation. The validity of the nanosecond pulsed speckle contrast imaging with uniform pulse rate has already been proven in [R104].

The pulsed illumination comes with limitations as well. The correlation time may be close to the finite pulse width resulting in distortion in temporal averaging and in β [R102]. We estimate this limit, derived from the frame-rate requirements of [R102], as $\tau_c/T > 4$, where the β becomes near distortion-free of this effect. Thus, e.g. $T = 5\mu s$ pulses enable to capture $\tau_c > 20\mu s$ dynamics.

A simulation was done with exposure time of $2\ ms$ at constant laser intensity (continuous wave, CW) and a single exposure with the decreasing illumination value ($I \propto 1/t$) using (4.4). The υ_2 and τ_c relations are presented in Fig. 4.1. In the simulations, three different realistic flow dynamics were considered: $SO_{n=2}, SU/MO_{n=1}$ regimes with $\beta = 0.3, 1-\rho = 0$ values, and $MU_{n=0.5}$ with $\beta = 0.3, 1-\rho = 0.2$ [R102]. Fig. 4.1b) shows the absolute sensitivity S_a, defined as υ_2 sensitivity to absolute flow changes [R105], at the different physiological regions and dynamics.

The sensitivity of the continuous wave illumination remains localized in a τ_c region raising the need for changing the exposure time to capture rather different flow speeds. The varied illumination on the other hand flattens the sensitivity curves and shifts the sensitive parts of the different dynamics into τ_c regions where they actually occur: $SO_{n=2}$ curve towards lower τ_c of larger flow rate, etc. As a result, we expect that our method compresses and enhance the flow speed coverage while having sensitivity at various dynamics in the physiologically important span [R106].

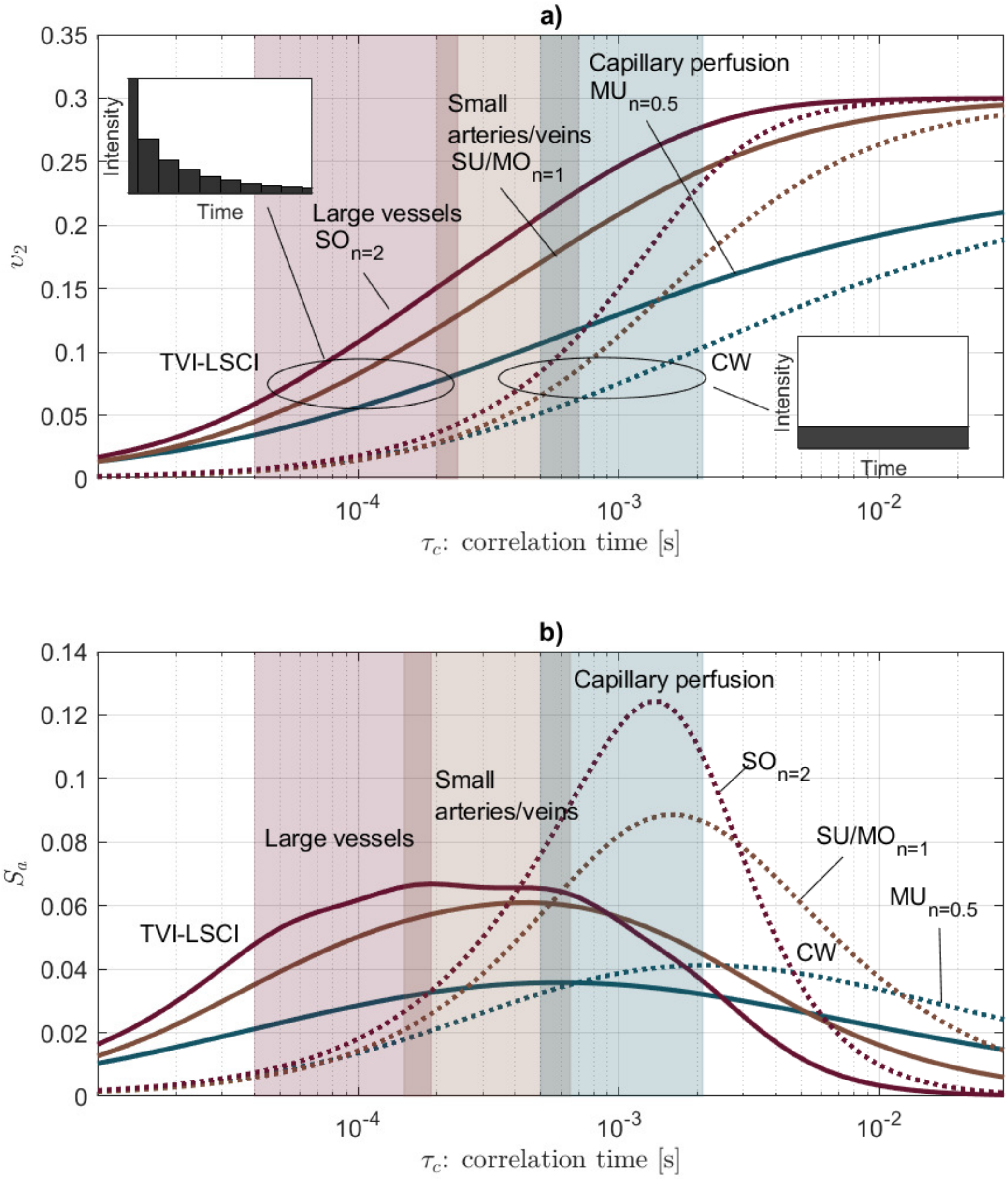

Figure 4.1: Simulation of 2 ms constant illumination (dotted curves) and single-shot 2 ms time varied intensity illumination (solid curves) speckle contrast with $\beta = 0.3$, $1 - \rho = 0.2$ for $n = 0.5$ and $\beta = 0.3, 1 - \rho = 0$ for $n = 1, 2$ regimes. Fig. a) shows the physiological regions, dynamics types, and the speckle contrast versus correlation time relations. Fig. b) shows the absolute sensitivity of the different dynamics versus illumination scheme.

4.2 In-vitro and in-vivo validation

Two experiments were conducted: first, human full blood was pumped through a clear channel slide, and second, the blood flow in the vessels visualized on a surgically prepared mouse brain surface. The samples were illuminated with a fast modulated continuous laser diode and observed with a camera.

In details, the laser spot was generated by a non-collimated single-mode laser diode (RLD84PZJ2, λ=842 nm, 220 mW, ROHM Co., Ltd., Japan). The laser diode was placed in a mount with thermoelectric cooling stage (HLD001, Thorlabs, Newton, NJ, USA). The images were acquired with 10x and 4x infinity corrected objectives (Thorlabs, Newton, NJ, USA) and a monochrome camera of 3.45x3.45 μm^2 pixel size (Basler ACA2040-55um, Basler Vision Technologies, Germany). The minimal laser pulse length was $T_{on} = 5\ \mu s$ (200 KHz sampling rate). Interfacing between a host computer, the camera trigger and the pulse waveform generation were done by a data acquisition card (USB-6211, National Instruments Co., Austin, TX, USA). The timing and stability performance of the setup was verified by a Si fixed gain detector (PDA015A/M, Thorlabs, Newton, NJ, USA) and a spectrometer (AvaSpec-ULS2048 StarLine, Avantes Ltd., The Netherlands).

In the first experiment, a syringe pump (SN-50F6, Sino Medical-Device Technology Co., Ltd., China) drove the blood through a μ-Slide I Luer channel slide (ibidi GmbH, Germany). The measured medium was room-temperature anticoagulated (citrate) packed red blood cell product for transfusions. The flow velocity was varied across a large dynamic range, from 0 to 600 mL/min in 19 logarithmic distributed steps (considering the flow control resolution of the syringe pump). These volumetric flow rates resulted in 0 to 37.5 mm/s velocities, taking into account the dimensions of the channel. The visible area was 720x540 μm^2 and the speckle contrast was then calculated over a large region of interest of uniform speed distribution using (5.21) [R107].

In the in vivo experiment, first we deeply anesthetized a mouse (strain: C57BL6/J) by 25 mg/kg xylazine and 125 mg/kg ketamine in 0.9% NaCl mixture, and then we fixed the head of the animal in a stereotaxic frame (Stoelting Inc, USA). Next we made a 1 cm long sagittal incision on the skull, and cleaned the surface by 3% H_2O_2. With a high speed drill we opened the skull and made a 5x5 mm window on the parietal part. To avoid the drying of the tissue, we put physiological saline solution on the brain and covered it with a glass cover slip. The used 4x objective resulted in appr. 4x3 mm useful visible area on the brain surface. The speckle size was $s \approx 13.2\mu m$.

First, the model given in (4.4) has been identified based on controlled measurements of the ex vivo setup. In the second step, to make the effect of an intensity profile predictable, we used the identified model for optimization and used it later on the in vivo measurement.

We defined $\tau_c := k\frac{1}{v+v_b}$, where v is the flow speed in the channel, v_b is the speed corresponding to Brownian motion and k is a scaling factor, $\rho = 1$ neglecting the static scattering component. As the exploration of second type dynamics induced variability is not in the scope of this article, we assumed $n = 1$ for the ex vivo characterization. For the identification (4.4) was extended with a v_s offset as proposed in [R96], to better account for static scatterers and measurement noise. The identification process was formulated as an optimization problem, where the free variables are: β, k, v_s and v_b. The goal of the optimization was to minimize the root-mean-square error (RMSE) between the measured and the simulated contrast values:

$$\min_{\beta,k,v_b,v_s} \sum_{i=1}^{M} RMSE(\boldsymbol{\kappa}^{(i)} - \boldsymbol{\kappa}_{sim}^{(i)}), \tag{4.5}$$

where M is the number of different exposure times, κ is the measured and κ_{sim} is the simulated contrast. The optimization was done by the MATLAB 2020a $fmincon$ function interior-point method from 20 initial points generated by Latin Hypercube Sampling (LHS) [R108]. The identified parameters were given as $\beta = 0.195$, $k = 6.027 \cdot 10^{-4}\ mm$ and $v_b = 0.0072\ mm/s$ with RMSE of 0.012 ± 0.0047.

During intensity profile optimization the goal was to extend the dynamic range of the non-saturating speckle contrast values from the $\tau_c \approx 10^{-5} - 10^{-2}$ s span. A given exposure time has been sliced into sections of different lengths, and each section could have different repetition rate of the fixed length pulses (i.e. equivalent CW constant intensity). From an optimization point of view the variables were the length and duty cycle of each section. A feasible implementation requires the lengths to be integer multiplicative of the hardware limited pulse width ($T_{on} = 5\ \mu s$), thus the number of pulses in a particular section becomes $N_i = round(\frac{T_i D_i}{T_{on}})$, where T_i is the section length and D_i is the duty cycle. These pulses are then equally distributed on the resulting $T_i^h = round(\frac{N_i T_{on}}{1-D_i})$, where subscript h indicates the hardware implemented section length. The rounding introduces discontinuities in the cost function rendering derivative based optimizer not applicable. Therefore, instead of the $fmincon$ algorithm, $patternsearch$ was applied from 20 initial points generated by the LHS, similarly to the identification process. The cost function and optimization was defined in the following way:

$$\min_{T_i, D_i} \ \sigma\Big(\frac{\Delta\kappa(T,\tau_c)}{\Delta t_c}\Big) + \mu\Big(\frac{\Delta\kappa(T,\tau_c)}{\Delta t_c}\Big)^{-1}, \tag{4.6}$$

$$\text{subject to} \ \ t_c = \log(\tau_c), \tag{4.7}$$

$$\sum_i T_i \cdot D_i = T_{const}, \tag{4.8}$$

where T_{const} is the total "on time" of the equivalent exposure using one constant frequency, $\sigma(\cdot)$ is the standard deviation and $\mu(\cdot)$ is the mean. The first term of the cost function (4.6) forces the convergence of the difference quotients toward a constant value, realizing a linear-like response on the logarithmic scale. The second term forces the speckle contrasts to spread, by maximizing the mean slope of the response. The (4.8) puts a constraint on the exposure time. A change of variable is made (t_c), since the near-linear response is expected on the logarithmic scale, where the differences are calculated between the experimentally evaluated flow speeds. The simulated and measured speckle variances are illustrated in Fig. 4.2 labeled with the different illumination scenarios. The curves represent a single exposure per rate with no averaging of multiple frames. Due to the lack of continuous illumination control in the setup, the constant illumination cases in the comparison were produced by uniformly distributed pulse trains similarly to [R104].

It can be observed that the resulting correlation time span has higher dynamic range compared to the uniformly distributed illumination setups as expected.

4.2.1 In Vivo Experiment Results

The protocol was the following during the experiment: after the preparation of the animal, the optical setup is adjusted and a sequence of 100 frames was captured for each measurement scenarios and then the stored sequences were evaluated. The scenarios contained continuous and modulated pulse train illumination versions as well. Before capturing a series, we adjusted the laser position in order to use the broadest dynamic range of the camera at the given exposure time with no saturating pixel values. Finally, the speckle contrast was then calculated with (5.21) on a $7x7$ pixels sliding windows in the individual frames and to improve the signal-to-noise ratio we averaged across the contrast maps.

The results are presented in Fig. 5.6. The images show that for such relatively small flow speed ranges present in the prepared mouse cranial window our TVI-LSCI method

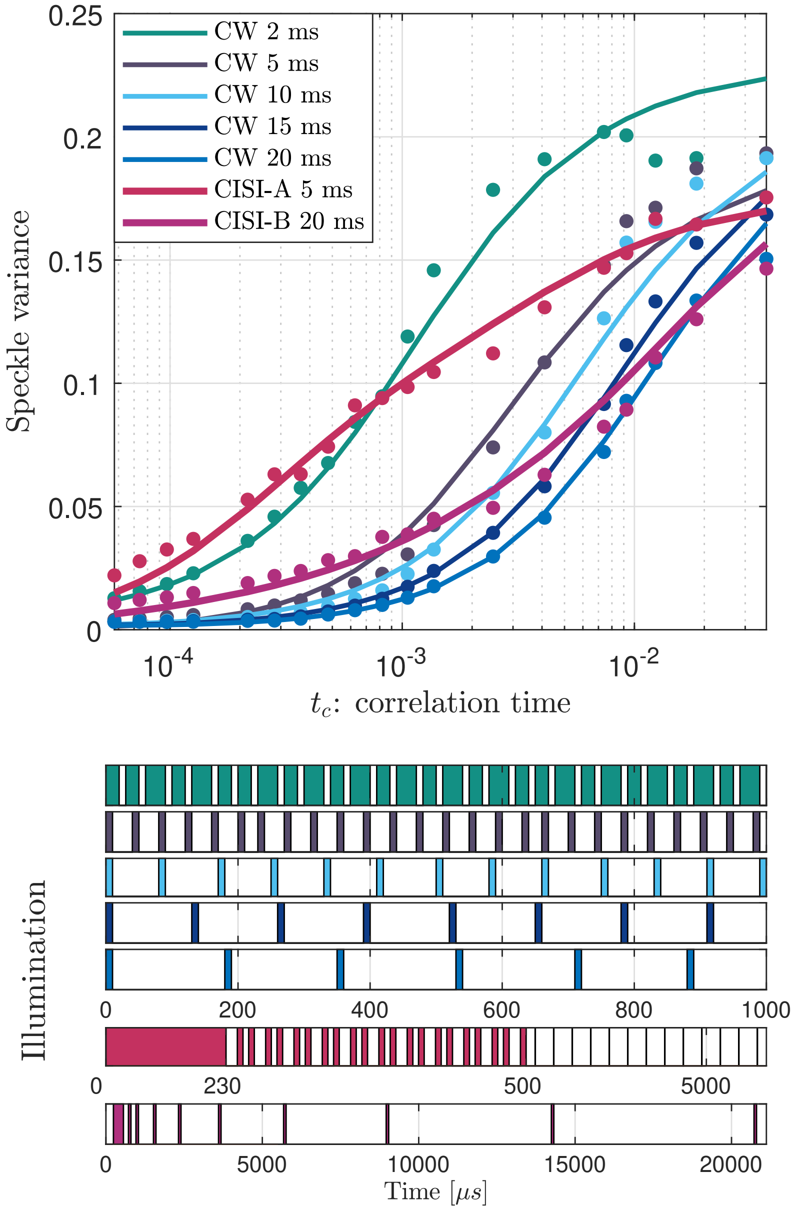

Figure 4.2: Measured and simulated speckle variances given different exposure times and laser pulse modulation setups as a function of flow rate. CW and CISI pulse trains are illustrated in the bottom figure. For the constant frequency setups only a section is shown (1000 μs), for visualization reasons.

perform similarly to CW LSCI. However, it is expected based on our simulations and ex vivo experiment, that in scenarios with higher flow speed ranges like in the human circulatory system TVI-LSCI can achieve better speckle variance and gaining advantage by its higher dynamics mapping. Such experiments will be carried and evaluated in the future.

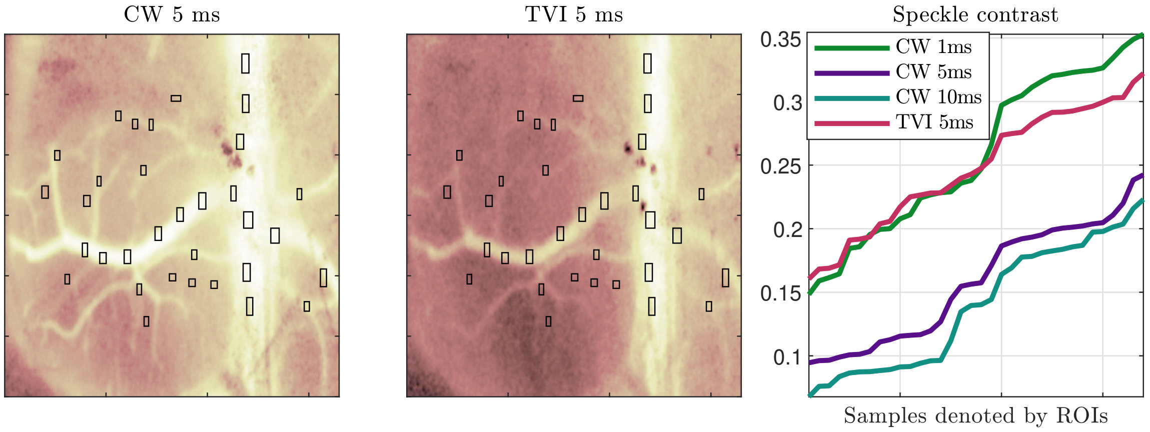

Figure 4.3: In vivo experiment showing speckle contrast of the surface of a mouse brain. Image captions indicate continuous illumination (CW) and varied illumination (TVI-LSCI) outcomes at different exposure time and pulse train length. The ROIs are registered on each image and picked at different vessel size positions. The shown field of view is $3.2x3.2mm^2$.

4.3 Real-time implementation

For the real-time implementation a Raspberry Pi 4, a custom-developed software and Basler camera were used. A Raspberry Pi 4 Model B carries out the digital pulse wave generation, the camera control, and the image processing tasks through a custom-developed software. Fig. 4.4 depicts the sample-in-the-loop experimental setup. The protocol of an experiment can be summarized as follows: First, the user selects the optimization scenario and the related thresholds and reference values. Second, an initial pulse wave is generated to capture a single image for ROI selection purposes. Afterward, the optimization algorithm updates the pulse sequences based on 10 averaged contrast images (with a resolution of 2000x1500 pixels). It continues to do so until a maximum number of iterations or termination limit is reached. The pulsetrains (leaving the GPIO pins of the Pi) control the 660 nm 50 mW laser diode through a laser driver (LDP-VRM 01-12 CA, PicoLAS, Germany) and at the same time trigger the monochrome digital camera (Basler acA2040-55um). Based on preliminary investigations we limited the minimum pulse width to 10 μs. With shorter pulses the proportion of laser transients becomes dominant, which introduces two unwanted effects: average intensity significantly lowers, and contrast lowers because of the larger proportion of incoherent light [R109]. Furthermore, the laser is mounted in a thermally stabilized mount (LDM21, Thorlabs, Germany) driven by a Thorlabs TED200C temperature controller. The constant temperature improves contrast by reducing temperature-induced laser mode hopping.

The validity of pulsed speckle contrast imaging has already been proven in [R104]. In this method, uniform intensity and uniform length discrete laser pulses with uniform pulse rates are used instead of continuous wave illumination. It uses laser pulsetrains of uniform intensity and uniform length discrete pulses, however, it changes the density of the pulses that ultimately simulates a varying intensity during a single exposure. Using a pulse sequence made of multiple density pulsetrains (e.g. 3 pulsetrains of equal length with 75%, 50% and 25% duty cycles concatenated) enables high dynamic range flow rate imaging during this single exposure.

We made this discrete pulse sequence to be a function of a single variable. This func-

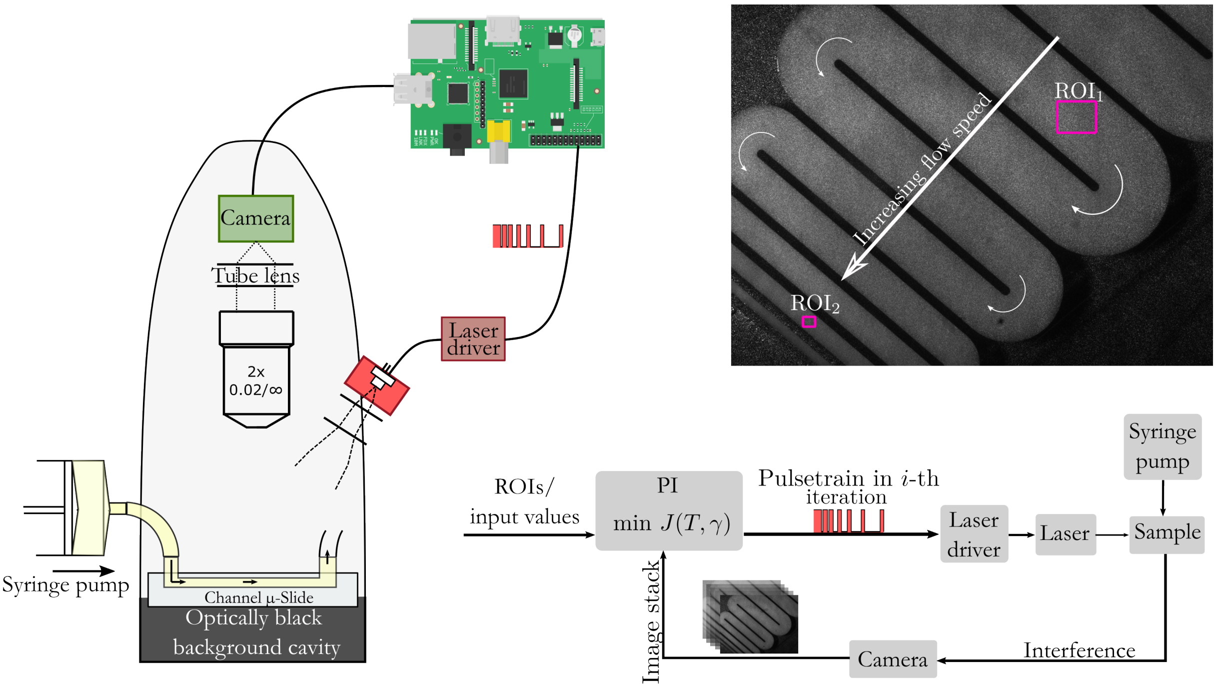

Figure 4.4: The experimental setup can be seen on the left-hand side. A medical syringe pump provides a constant flow speed, while the laser and the digital camera are controlled by the Raspberry Pi. A raw speckle image with a typical ROI selection is illustrated in the upper right corner. The schematic diagram in the lower right corner summarizes the sample-in-the-loop LSCI method.

tion limits the number of feasible sequences but helps with the optimization problem by introducing only one more variable besides the exposure length. The additional parameter affects the spacing – in a form of a power function – between two consecutive high states. The sequence starts with an initial high state. The next high state is defined by the number of low states (n_{LOW}) following the initial high state as:

$$n_{LOW}(i) = round(i^{\gamma}) - 1, \tag{4.9}$$

where the discrete sequence is loaded with binary values from $i = 0$ to $i = \frac{T}{10\ \mu s}$, T is the exposure length, $\gamma >= 0$ is the spacing factor. If $n_{LOW} \leq 0$ the next state will remain a high state. The continuous wave laser setup is a limiting case when $\gamma = 0$, typically we evaluated $0 \leq \gamma \leq 1.4$. Fig. 4.5 illustrates how the spacing factor affects the average ROI intensity for different exposure lengths.

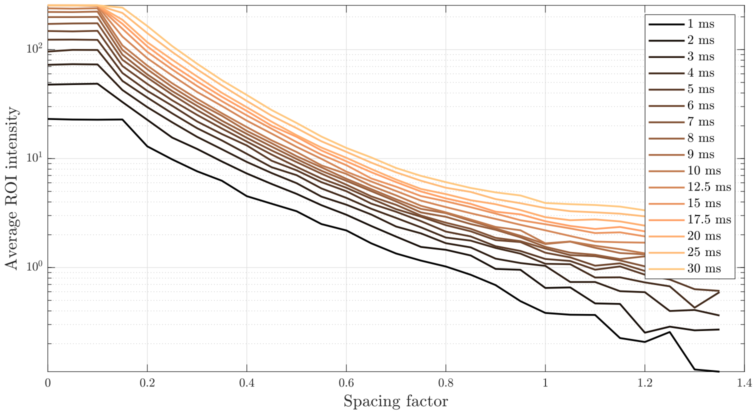

Figure 4.5: Measured average intensities in an ROI are visualized as a function of the spacing factor. It can be observed that after an initial interval between 0 and 0.1, a spacing factor of 1 reduces the intensity by more than an order of magnitude. Small values of the spacing factor would have only a visible effect on exposures above 30 ms.

The typical way of quantifying flow speed in LSCI is by means of contrast calculation. The speckle contrast is calculated on a single digital image or sequence of consecutive images (to descrease noise level), in both cases using a sliding window. The contrast is calculated by taking the quotient of the standard deviation and the mean of the intensities in the current window. The window size is usually $n \times n$, where n is in the range of 5 to 15 [R110]. The spatial speckle contrast is defined as:

$$\kappa = \frac{\sigma(I_s)}{\langle I_s \rangle}, \tag{4.10}$$

where $\sigma(I_s)$ and $\langle I_s \rangle$ are the sample standard deviation and the sample mean in the current window. The choice of window size affects the noisiness and the resolution of the resulting contrast map. The contrast value is averaged on 10 consecutive images in order to reduce noise and improve the consistency of the optimization.

We defined three major optimization problems: contrast setpoint, sensitivity maximization, and dynamic range maximization. Previously it was shown in [R111] that the intensity has a significant effect on the contrast values. Thus, besides the major objectives, all three share an optional penalization for underexposed images; a linear term penalizes the given parameter/parameter set when the average intensity falls below a predefined threshold in the ROIs. In our experimental setup ROI sizes ranged between 10x10 to 50x50 depending on the size of the evaluated cross-section in the channel slide.

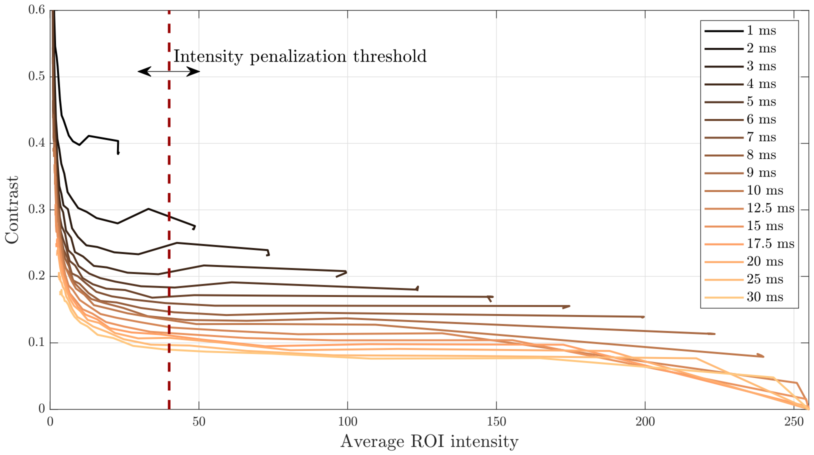

Figure 4.6: Observed speckle contrasts plotted with respect to the average ROI intensity. Low intensities can cause falsely observed large contrast values, while high intensities can cause falsely observed low contrast values. In order to avoid the potentially detrimental effects, a method of intensity penalization is implemented during the optimization. The figure indicates that a threshold around an intensity level of 40-50 guarantees a linear, flat response.

4.3.1 Contrast setpoint

Optimization based methods are widely used in control problems [R112, R113, R114, R115], we defined the first scenario as an optimization to setpoint contrast value. The user can select an arbitrary ROI and define a desired average contrast value in that particular ROI. Then the gradient descent algorithm iteratively modifies the continuous wavelength, which also determines the exposure length of the camera. This first scenario aims to approach the sample-in-the-loop concept in the simplest manner. For this reason, we decided to optimize a single variable with the gradient descent method as follows:

$$T_{i+1} = T_i - \alpha \frac{\Delta J}{\Delta T}, \tag{4.11}$$

where α is the step size, Δ denotes the differences in cost J and exposure length T between the i-th and $i-1$-th iteration.

$$\begin{aligned} \min_{T} \quad & J(T) = |\kappa(T) - \kappa_{ref}| + J_{exp.}, \\ \text{s.t.} \quad & T \in [1, 30], \\ & J_{exp.} = \begin{cases} 0, & \text{if} \quad \mu >= \mu_{ref}, \\ \frac{\mu - \mu_{ref}}{\lambda}, & \text{else.} \end{cases}, \end{aligned} \tag{4.12}$$

where κ is the average calculated contrast in the ROI, κ_{ref} is the user-defined contrast setpoint, and μ_{ref} is the average intensity threshold. The offset from the reference intensity μ_{ref} is normalized by λ in order to scale the additional penalization in the range of the unpenalized cost, in our experimental setup, a reasonable value for the λ was around 40. The parameters of the control: α, the number of iterations, and the λ were determined based on multiple experiments with different channel slides and flow speeds.

4.3.2 Sensitivity maximization

The cost is defined as the inverse of the difference:

$$\begin{aligned} \min_{T} \quad & J(T) = \frac{1}{|\kappa_1(T) - \kappa_2(T)| + \epsilon} + J_{exp.}, \\ \text{s.t.} \quad & T \in [1, 30], \\ & J_{exp.} = \begin{cases} 0, & \text{if} \quad \mu >= \mu_{ref}, \\ \frac{\mu - \mu_{ref}}{\lambda}, & \text{else.} \end{cases}, \end{aligned} \tag{4.13}$$

where κ_1 and κ_2 are the average contrast values in the respective ROI and ϵ avoids division by zero.

4.3.3 Dynamic range maximization

Study [R116] showed that by utilizing time variant illumination during the camera exposure the dynamic range of the laser speckle contrast imaging can be greatly improved.

$$\begin{aligned} \min_{T, \gamma} \quad & J(T, \gamma) = |\kappa_1(T, \gamma) - \kappa_{ref}| + |\kappa_2(T, \gamma) - \kappa_{ref}| + J_{exp.}, \\ \text{s.t.} \quad & T \in [1, 30], \quad \gamma \in [0, 1.4], \\ & J_{exp.} = \begin{cases} 0, & \text{if} \quad \mu >= \mu_{ref}, \\ \frac{\mu - \mu_{ref}}{\lambda}, & \text{else.} \end{cases}, \end{aligned} \tag{4.14}$$

where $\kappa_{ref.}$ is a user-defined contrast value, around which the sensitivity ought to be the least.

4.4 Results of the real-time implementation

4.4.1 Optimization to contrast setpoint

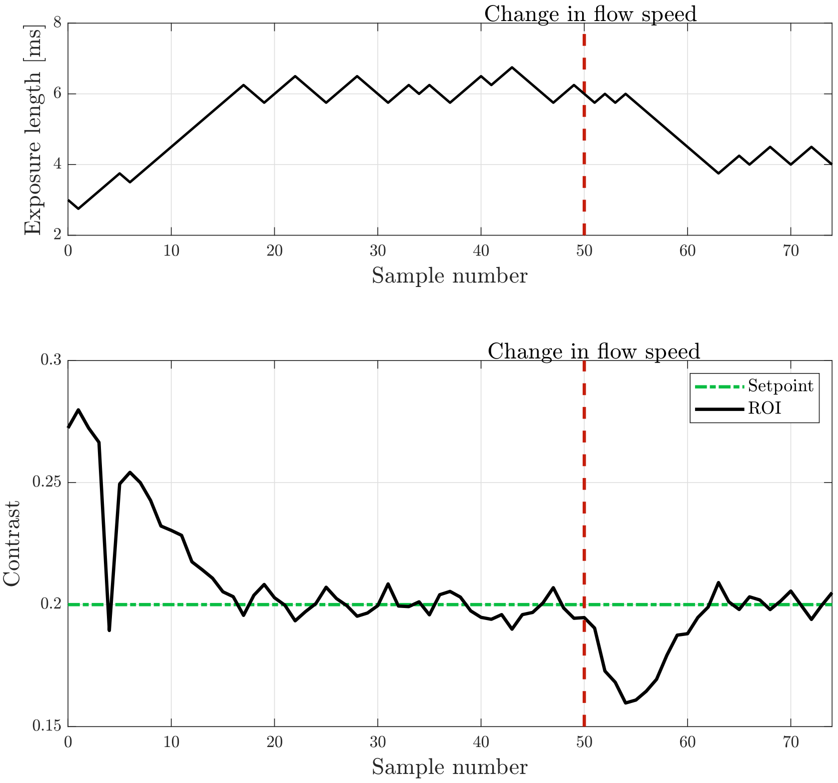

Figure 4.7: The set exposure length and measured contrast with respect to the current sample number are illustrated by solid black lines. The flow speed of the syringe pump has been modified during the experiment (denoted by the dashed red line), creating an external disturbance on the system. The contrast setpoint is depicted by the dashed green line.

Fig. 4.7 demonstrates the result of the first scenario, namely the optimization for a specific contrast value. A contrast value of 0.27 is observed with an initial exposure length of 3 ms. Then the gradient descent algorithm iteratively increases the exposure length to match the reference 0.2 contrast value. Besides the fluctuation caused by the measurement noises, the algorithm settles for an exposure length of 6 ms. When the disturbance occurs (in a form of flow speed change), the observed contrast drops by 0.05, but the algorithm compensates for it after a couple of iterations and settles for a new 4 ms exposure length. A change in flow speed induces a change in the measured contrast values, which are based on the captured image. The larger deviance in the contrast value ultimately results in a larger cost. A new optimum can be found by either increasing or reducing the exposure time so that deviance can be counteracted. The compensation can be done only in a feasible range of the parameters which determine the operation of the laser and the camera.

4.4.2 Sensitivity maximization

Despite that the optimization of the exposure length would be sufficient for sensitivity maximization, we carried out an experiment using both of the variables for demonstration purposes: the spacing factor and the exposure length.

Fig. 4.8 demonstrates well that the optimizer achieved the lowest costs when the spacing factor was close to zero. The small spacing factor in practical perspective translates to a continuous wave-like operation, which is otherwise expected to yield the best result in terms of sensitivity.

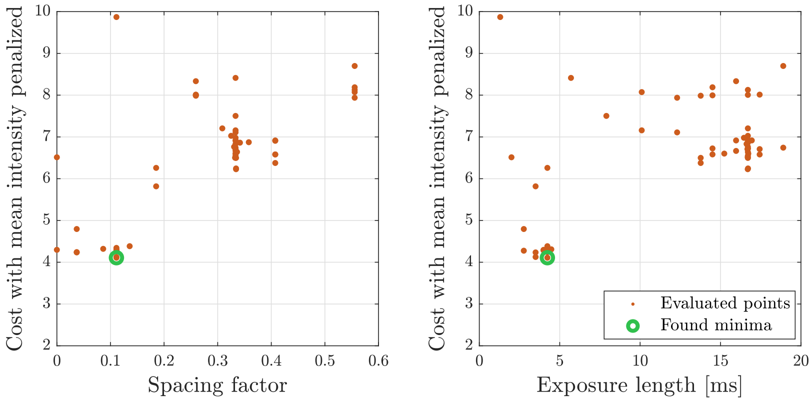

Figure 4.8: Evaluated spacing factor-exposure length combinations are illustrated during the sensitivity maximization scenario. It can be seen that the lowest costs are achieved if the optimizer converges the pulse sequence to the continuous wave operation.

4.4.3 Dynamic range maximization

In Fig. 4.9 we showcase an exemplary optimization using the grid search algorithm [R117]. The algorithm aims to minimize the cost function given in (4.14). It can be seen that it converges to a spacing factor of around 0.3 and to an exposure length of 8 ms, where a minimum is found. In this multivariate scenario, the grid search algorithm was preferred in order to avoid the possibility of quick convergence to a local minimum.

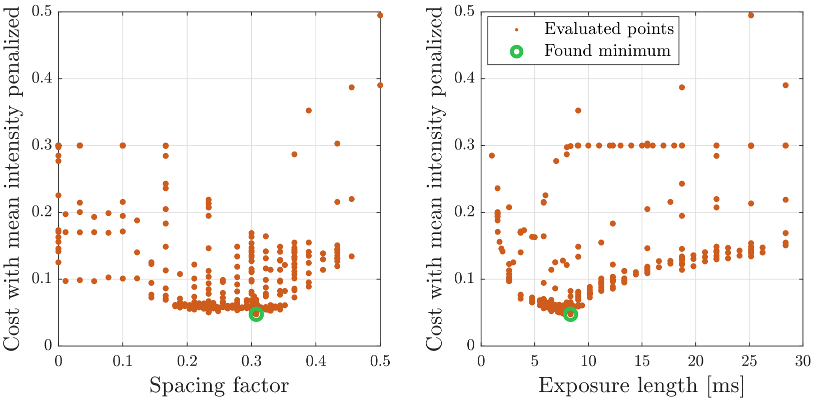

Figure 4.9: Evaluated spacing factor-exposure length combinations are illustrated during the dynamic range maximization scenario. It can be seen that the cost can be lowered by applying time-varying illumination. An optimal solution is found around a spacing factor of 0.3 and an exposure length of 8 ms.

We explored the effect of the spacing factor and exposure length in order to ascertain the cost surface and that the algorithm indeed found a minimum. The exposure length is varied in a range from 1 ms to 30 ms and the spacing factor is from 0 to 1.4. Fig. 4.10 and 4.11 depict the optimization surfaces given two different reference contrast values. The reference value of (4.14) is set to 0.1 in Fig. 4.10 and 0.3 in Fig. 4.11.

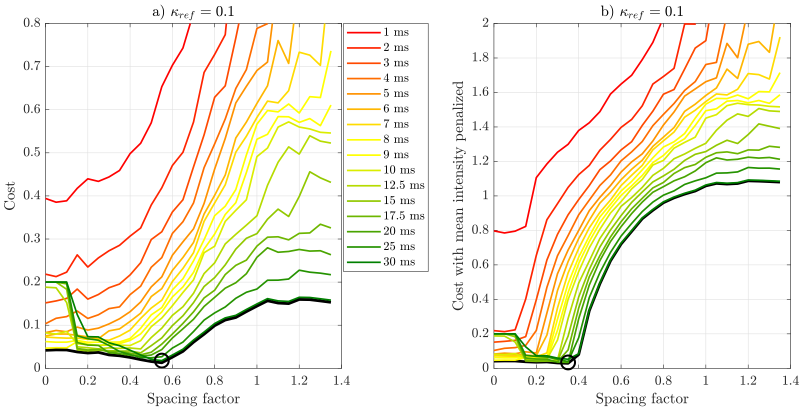

Figure 4.10: The measured optimization surface when the reference value is set to 0.1 is approximated with a family of curves. Subplot a) represents the "raw" cost, while subplot b) the cost when the average intensity is penalized.

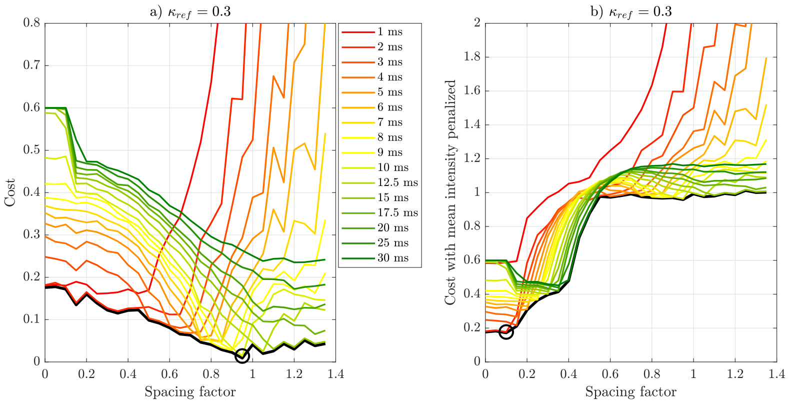

Figure 4.11: The measured optimization surface when the reference value is set to 0.3 is approximated with a family of curves. Subplot a) represents the "raw" cost, while subplot b) the cost when the average intensity is penalized.

The behavior of the cost function towards the minimum (0) and maximum (1.4) of the spacing factor is dominated by the phenomenon related to the average intensities. Firstly, for small values of the spacing factor, the laser switches to continuous wave-like operation, which means increased exposure. The increased exposure (mostly in the case of longer exposure times) leads to saturation, which in return lowers the observed contrast (as indicated in Fig. 4.6). Zero contrast values consequently saturate the cost function, as it can be seen in Fig. 4.10 and 4.11 subplots a) for exposure times above 20 ms. Secondly, the countereffect of high spacing factors introduces numerical instability into the calculation of the speckle contrast. Falsely observed high contrast values increase the cost; numerical instability appears at smaller spacing factors for shorter exposure times. Subplots b) showcase the intensity penalized cost surface. The significant difference between the raw and the penalized versions is that the cost towards the larger spacing factors is affected by an additional term, which penalizes the underexposed images in a linear way. The start of the penalization – when the exposure falls below the predefined threshold – is dependent on the actual exposure length as expected.

The theoretical minimum moves toward the continuous wave operation mode for larger values, as it is indicated by the black circle on the envelope. Such behavior is expected since larger spacing factors have a great effect on the dynamic range, making the response so wide that the contrast values fall below the reference values, hence increasing the cost. Fig. 4.12 depicts the Pareto front around the minimum; it can be seen that similar costs are achieved with different combinations of exposure length and spacing factor.

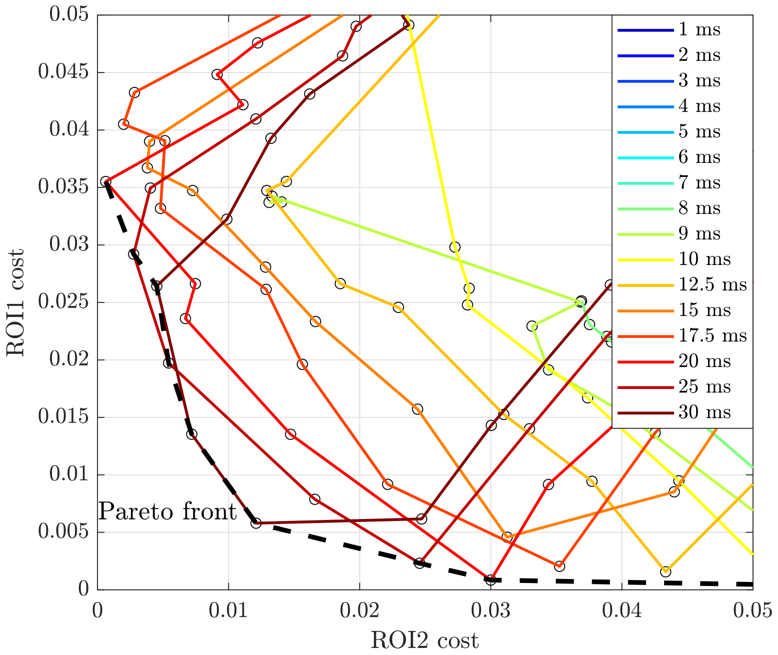

Figure 4.12: As the dynamic range maximization in (4.14) is formulated as a multi-objective optimization, a Pareto front can be found, where ROI1 and ROI2 costs represent the distances from the reference contrast value.

4.5 Thesis summary

Laser speckle contrast imaging is a method with great potential, as it can be a cheap, noninvasive imaging modality in medical applications. It is capable of generating blood flow maps and recently was used in assessing the microcirculation in diabetic feet. On the other hand, the method has some drawbacks and lacks models which can be used to interpret measurements and make optimizations. In [J3], we introduced time varied illumination laser speckle contrast imaging, which is a method to improve the dynamic range of the technique by varying the laser light during the camera exposure. I developed the model which describes the effect of varying illumination and defined optimization scenarios to improve the dynamic range. In [J4], I developed the laser illumination optimization method on a Raspberry Pi, which realizes a real-time implementation of the technique.

5

Modeling the effect of exposure, static and dynamic scatterers on laser speckle contrast imaging

Thesis group 4: Models of exposure and scattering medium in laser speckle contrast imaging

Thesis 4
I contributed to the theory of laser speckle contrast imaging by developing a mathematical model of static and dynamic scatterers. Also, I contributed to the theory by developing a model of overexposure compensation. I validated the models through simulations and invivo experiments.

Thesis 4.1
I developed a mathematical model which describes the effect of static and dynamic scatterers on the measured contrast; the model also describes how ensemble averaging affects the contrast.

Thesis 4.2
I developed a mathematical model which describes how overexposure affects the measured contrast, and how can the model be used to compensate for the overexposure.

Thesis 4.3
I validated the mathematical models through simulations and invivo experiments by fitting the model parameters to the measured variables. The fitted models showed good accuracy and consistency with the data.

Publications relevant to the theses: [J5, J6].

5.1 Model of scattering medium and ensemble averaging

Laser speckles are the result of the superposition of scattered coherent light forming interference patterns. The movement of the scatterers creates phase fluctuations, and as a result, the interference patterns decorrelate during observation time. Inert materials possess a behavior of fixed patterns, while decorrelation will increase with the movement of the scatterers and with other local activities of the living tissue. To quantify decorrelation and flow rate, the speckle contrast is calculated on a digital image or series of images of the sample. For the calculation, as the basis of the LSCI technology, the standard deviation of the intensity is normalized by the mean intensity in spatial or temporal sliding windows to form a contrast map. The observed speckle pattern is affected by static and dynamic scatters of the observed surface. Static scatterers remain fixed, while dynamic ones are moving. Speckle patterns of consequent frames are correlated in time in the presence of non-moving scatterers, e.g. contains frozen speckle patterns. This nonzero speckle pattern correlation is the consequence of the temporal stability of the mutual location of static scatterers, such as skin or tissue, and the laser source. In practice, the result is granular image and false flow rate estimate on static and static scatterer-rich areas. We investigated the use cases of ensemble averaging and how it changes contrast map quality as a function of static and dynamic scatterers ratio. We proposed a model, which describes the relation between scatterer ratios and contrast outcomes, also with respect to ensemble averaging.

We used two premises: the frame by frame illumination change should not diminish the speckle contrast of the individual frames and at the same time, the consecutive patterns should be uncorrelated. Hence, the correlation time τ_I of the illumination related objective speckle patterns must be significantly larger than the exposure time $T_{exp} \ll \tau_I$, and the decorrelation of the speckle patterns of the consecutive frames must be forced on the whole region of interest.

Different technical solutions could satisfy these conditions: slowly rotating ground glass diffuser [R118][R119], digital micromirror arrays [R120][R121], space light phase modulators, tunable laser diodes [R122], and other similar techniques that are commonly used in switchable laser speckle reduction solutions [R123, R124] may be considered for the purpose.

Next, we formulated the combination of intensity speckle patterns of static and dynamic scatterers to model the effect of sample size (number of frames). We adopted the common definition of the fraction of dynamic optical scatterers over total scatterers denoted by ρ, and the non-moving scatterers as $(1 - \rho)$. The static component is modeled as a single fully developed speckle pattern, the dynamic contribution was described by temporarily integrated distribution [R107], and an independent noise source was modeled by Gaussian noise as:

$$I = (1 - \rho)S(\lambda_S) + \rho D(k_D, \lambda_D) + W, \tag{5.1}$$

where S is random variables of exponential distribution with parameter $\lambda_S > 0$ representing static scatterers. Dynamic scatterers are described with the random variables D of a gamma distribution defined by shape-rate parametrization: $k_D, \lambda_D > 0$, where λ_D is rate and the k_D is the shape parameter. Camera noise is taken into account as random variable of normal distribution $W \sim \mathcal{N}(\mu_W, \sigma_W^2)$. Any non-zero mean error source such as dark current or readout noise can be modeled by non-zero μ_W bias and other zero mean sources, like photon or electronic noises, can be described by σ_W^2.

The quality factor was calculated in an alternative way – based on variance and mean. As for the standard deviation of the sample standard deviation no closed-form expression exists. The expression can be approximated by using Taylor series expansion. However, due to the highly nonlinear nature of the problem even the second order approximation introduces significant inaccuracies, the variance based variables were defined by:

$$K_s^v = \frac{\sigma_s'^2}{\mu_s'}, \quad \epsilon_K^v = \frac{\mathrm{Var}\left(K_s^v\right)}{\mathrm{E}\left(K_s^v\right)}, \tag{5.2}$$

where σ_s^2 and μ_s are the sample variance and sample mean, respectively. The K_s^v is evaluated similarly to the spatial speckle contrast on a sliding spatial neighborhood of $n_s \times n_s$ pixels than ϵ_K^v is calculated through n frames.

The effect of the number of samples n was used for constructing the variables of the distributions for the two illumination cases. Since variance of sample variance was calculated, the dependent variables were extended with $n^{1/4}$. The illumination has no effect on the expected value, thus separate variables were used for the calculation of the variance and the expected value. Using the scaling property of the exponential, the gamma distribution, and the variance, the following change of variables could be made for the different illumination cases.
Stable illumination:

$$\text{Var}: \quad \lambda'_S = \frac{\lambda_S}{1-\rho}, \quad \lambda'_D = \frac{\lambda_D}{\rho} n^{1/4}, \quad k'_D = k_D, \qquad \mu'_W = \mu_W, \quad \sigma'_W = \frac{\sigma_W}{n^{1/4}}, \tag{5.3}$$

Decorrelated illumination:

$$\text{Var}: \quad \lambda'_S = \frac{\lambda_S}{1-\rho} n^{1/4}, \quad \lambda'_D = \frac{\lambda_D}{\rho} n^{1/4}, \quad k'_D = k_D \qquad \mu'_W = \frac{\mu_W}{n^{1/4}}, \quad \sigma'_W = \frac{\sigma_W}{n^{1/4}} \tag{5.4}$$

Illumination independent:

$$\text{E}: \quad \lambda'_S = \frac{\lambda_S}{1-\rho}, \quad \lambda'_S = \frac{\lambda_D}{\rho}, \quad k'_D = k_D \qquad \mu'_W = \mu_W, \quad \sigma'_W = \sigma_W, \tag{5.5}$$

where the λ'_S, λ'_D, k'_D, μ'_W and σ'_W are the transformed variables. In order to express the quality as a function of sample size, we used moment generating functions [R125]:

$$M_S(x) = \frac{\lambda'_S}{\lambda'_S - x}, \quad M_D(x) = \Big(\frac{\lambda'_D}{\lambda'_D - x}\Big)^{k_D}, \quad M_W(x) = e^{\mu_W x + 0.5(\sigma'_W x)^2}, \tag{5.6}$$

where M is the moment generating function. The k-th moment and the sum of the random variables can be obtained in the following way:

$$M_I = M_S(x) M_D(x) M_W(x), \tag{5.7}$$

$$E[I^k] = \frac{d^k}{dx^k} M_I(x)\Big|_{x=0}. \tag{5.8}$$

The variance and the mean of the ratio distribution can be approximated using Taylor series expansion [R126]. Furthermore, utilizing that the covariance of the sample variance and sample mean is:

$$\mathrm{E}\left(\frac{\sigma_s'^2}{\mu_s'}\right) \approx \frac{\mathrm{E}(\sigma_s'^2)}{\mathrm{E}(\mu_s')} - \frac{\mathrm{Cov}(\sigma_s'^2, \mu_s')}{\mathrm{E}(\mu_s')^2} + \frac{\mathrm{Var}(\mu_s')\,\mathrm{E}(\sigma_s'^2)}{\mathrm{E}(\mu_s')^3}, \tag{5.9}$$

$$\mathrm{Var}\left(\frac{\sigma_s'^2}{\mu_s'}\right) \approx \frac{\mathrm{Var}(\sigma_s'^2)}{\mathrm{E}(\mu_s')^2} + \frac{\mathrm{E}(\sigma_s'^2)^2\,\mathrm{Var}(\mu_s')}{\mathrm{E}(\mu_s')^4} - \frac{2\,\mathrm{Cov}(\sigma_s'^2, \mu_s')\,\mathrm{E}(\sigma_s'^2)}{\mathrm{E}(\mu_s')^3}, \tag{5.10}$$

$$\mathrm{Cov}\left(\sigma_s'^2, \mu_s'\right) = \frac{\mu_3'}{n_s^2}, \tag{5.11}$$

$$\mathrm{Var}(\sigma_s'^2) = \frac{\mu_4'}{n_s^2} - \frac{n_s^2 - 3}{n_s^2 - 1}\frac{\sigma_s'^4}{n_s^2}, \tag{5.12}$$

$$\mathrm{Var}(\mu_s') = \frac{\sigma_s'^2}{n_s^2}, \tag{5.13}$$

$$K_s = \mathrm{E}\left(\frac{\sigma_s}{\mu_s}\right) \approx \frac{\mathrm{E}(\sigma_s')}{\mathrm{E}(\mu_s')} - \frac{\mathrm{Cov}(\sigma_s', \mu_s')}{\mathrm{E}(\mu_s')^2} + \frac{\mathrm{Var}(\mu_s')\,\mathrm{E}(\sigma_s')}{\mathrm{E}(\mu_s')^3}, \tag{5.14}$$

$$\mathrm{Cov}\left(\sigma_s', \mu_s'\right) = \frac{\mu_3'}{2\sigma_s' n_s^2}, \tag{5.15}$$

where μ_3', μ_4' is the 3rd and 4th central moment and n_s^2 is the area size. The two most specific limits of the model are given of static and dynamic content only ($\rho = 0, 1$) for stable illumination, assuming that λ_S=λ_D=λ, the complex relation simplifies to the following:

$$\lim_{\substack{k_D \to 1\\ \sigma_W \to 0\\ \rho \to 1\\ \mu_W \to 0}} \epsilon_K^v = \frac{n_s^2 - 4n^{1/4}(n_s^2 - 1) + \sqrt{n}(8n_s^2 - 6) - 1}{\lambda n^{3/2}(n_s^2 - 1)^2}, \tag{5.16}$$

$$\lim_{\substack{k_D \to 1\\ \sigma_W \to 0\\ \rho \to 0\\ \mu_W \to 0}} \epsilon_K^v = \frac{5n_s^2 - 3}{\lambda(n_s^2 - 1)^2}, \tag{5.17}$$

Equation (5.16) confirms the expected behavior, that the variance-based quality factor improves with increasing sample number n for a given n_s^2 area, and shows $\epsilon_K^v \propto 1/n$ dependency. Meanwhile, for static content Eq. (5.17) the quality is sample number n independent at constant illumination, meaning that the averaging does not improve the flatness of the contrast map. On the other hand, the interframe decorrelated illumination makes the samples independent and consequently reduces the variability of the static scatterers as well. In order to validate the model and observe the mixed static, dynamic behavior, a numerical simulation was implemented using the methods and models presented in [R127] and [R128]. Figure 5.1 shows a comparison of ϵ_K^v under stable and changing illumination at different ρ values and Fig. 5.2 demonstrates the effect of the variations of multiple distribution parameters.

The case of temporal contrast calculation was addressed as well. The temporal contrast calculation based flowmetry is demonstrated to be less sensitive to static scatterers in volume scatterers and flows [R129]. Using interframe decorrelated illumination the patterns become statistically independent frame by frame, and as a consequence, the flow rate cannot be estimated with the calculated temporal contrasts. In order to retain the proper temporal statistics and still evaluate the effect of ensemble averaging, we proposed a combined experimental method.

The temporal methods rely on determining the first-order statistics of the speckle fluc-

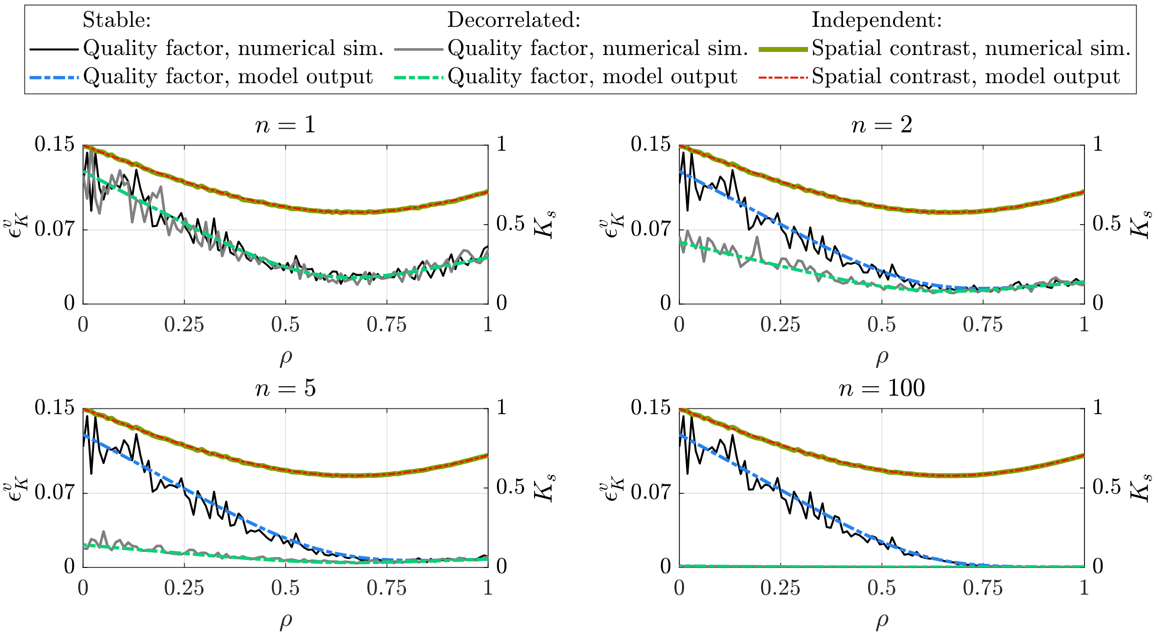

Figure 5.1: Comparison of the numerical simulations and the model. Quality factor ϵ_K^v is plotted on the left axis, while the spatial contrast K_s with respect to factor ρ on the right axis. The value of parameter ρ defines the fraction of dynamic scatterers and total scatterers ($\rho = 1$ only dynamic, $\rho = 0$ only static scatterers), n denotes the number of frames acquired, n_s^2 area was set to constant 400. The numerical simulation, similarly to [R127] and [R128], was carried out by generating independent random samples for D and W variables, while keeping S variable constant. A sample defines an intensity map as given in Eq. (5.23). The parameters of the random variables were chosen so that D and S variables had identical mean. The shape parameter was $k_D = 2$, which resulted in a $\sqrt{2}$ spatial contrast in the fully dynamic ($\rho = 1$) scenario, the μ_W and σ_W were set to 0.

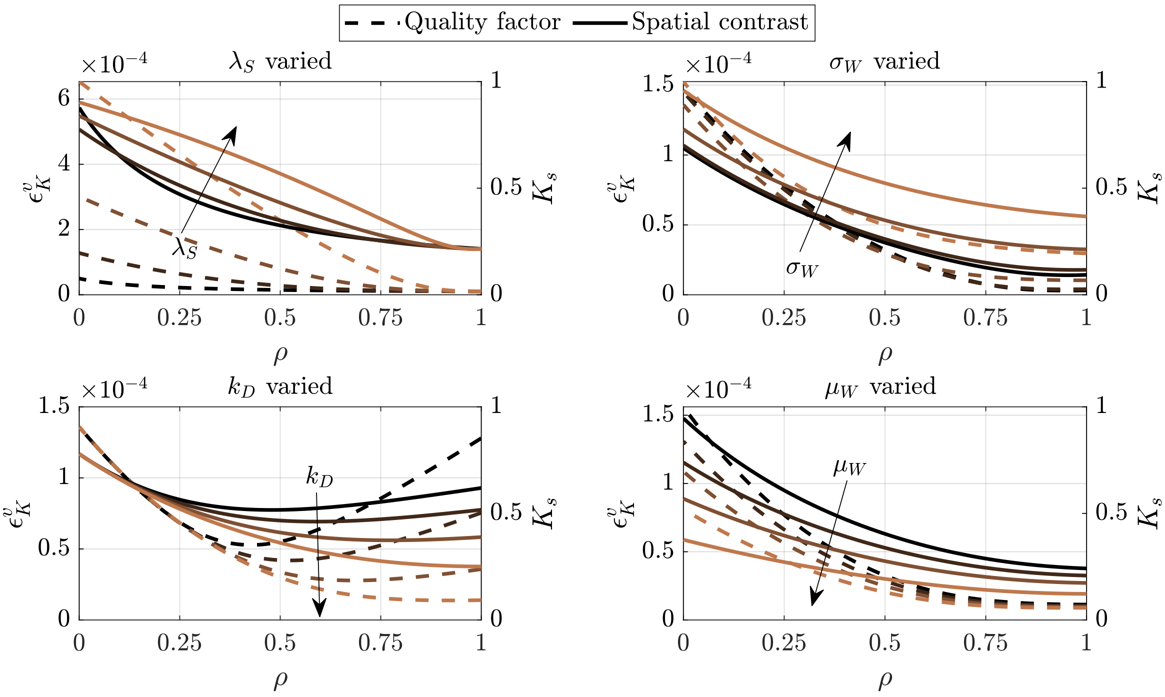

Figure 5.2: The model parameters have been varied around a nominal value in order to showcase the effect of the different parameter tendencies on the quality factor and the spatial contrast. The nominal values of the parameters have been based on the validation. The arrows indicate the direction of increase in the parameter values. The camera noise related parameters, namely σ_W and μ_W have opposite effect. Larger mean noise level causes larger spatial contrast degradation, this effect can be attenuated by acquiring several images as the trajectories of the quality factors indicate. Larger σ_W values superpose an additional pattern on the image, and increases the spatial contrast. The shape parameter k_D related to the ratio of camera exposure time and decorrelation time, larger values indicate higher ratios, and from a practical point of view a blurred image. Furthermore, the shape parameter doesn't have an effect on the fully static scenario ($\rho = 0$), as it affects only the distribution of the dynamic variable.

tuations data of a sequence [R101]:

$$K_t = \frac{\sigma(I_t)}{\langle I_t \rangle} = \sqrt{\frac{\langle I_t^2 \rangle - \langle I_t \rangle^2}{\langle I_t \rangle^2}}, \tag{5.18}$$

where $\langle I_t \rangle$ and $\langle I_t^2 \rangle$ are the mean and mean square values of the speckle intensity variations during exposure time. The temporal contrast calculation works on a $1 \times 1 \times n$ neighborhood using n temporal length that depends on the exposure time and frame rate [R101]. The exact relation between the contrast and flow rate is a complex question and depends on multiple factors [R98, R96, R129, R97, R99, R102, R130].

The temporal contrast is calculated according to Eq. (5.18) for a short sequence [R101] (e.g. 15-20 frames). Then, after providing an independent wavefront phase distribution, another contrast map is gathered. The contrast maps are accumulated in this manner and finally averaged.

Three versatile experiments were conducted to compare the predicted difference between the stable and the ensemble illumination schemes:

- Intralipid (Fresenius Kabi AB, Uppsala, Sweden) flow was observed while pumped through a clear channel slide phantom covered with a series of different thickness diffusers.
- Blood flow in vessels was visualized in vivo on a surgically prepared mouse brain surface.
- The underside of a fresh Ficus benjamina leaf was examined.

The general setup is detailed in Fig. 5.3. We changed the phase distribution of the scattered field of the laser with a pair of diffusers in which one diffuser was rotated. This arrangement supersede the presented single diffuser arrangements [R118][R121], in several aspects: i) a doubly scattered speckle system (mm range diameter aperture) approximates better Gaussian statistics, ii) the larger surface structures of one diffuser are suppressed effectively on the illuminated target, iii) the overall speckle pattern count using rotating diffuser, the maximum number of uncorrelated speckle patterns is limited by a single diffuser [R121], while the double configuration is still limited, but provides significantly larger independent pattern count [R131].

A laser spot was generated by a collimated and beam expanded single-mode laser diode driven by a constant current source (RLD82PZJ2, 820 nm central wavelength, 220 mW, ROHM Co., Ltd., Japan). The laser diode was placed in a mount with a thermoelectric cooling stage (LDM9T, Thorlabs, Newton, NJ, USA). The images were acquired with a 2x infinity-corrected objective, a 15 cm focal length tube lens, a linear polarizer (Thorlabs, Newton, NJ, USA), and a monochrome camera of 1536x2048 pixels resolution and $3.45x3.45$ µm^2 pixel size (Basler ACA2040-55um, Basler Vision Technologies, Germany). One fused silica 1500 grit diffuser of the dual pair (DGUV10-1500, Thorlabs, Newton, NJ, USA) was placed in a DC servo motorized rotational stage. The visible area was $4x5$ mm^2. The speckle size was $s \approx 10.4$ µm. The speed of revolution of the diffuser was set to a slow rotation of 0.05 rad/s to achieve $\tau_I \approx 50$ ms. We chose exposure times in the range of $2-3$ ms and we set the frame rate to 20 FPS in the demonstrations to satisfy the required premises. The number of emerging temporally independent speckle intensity patterns during the used exposure time is $M = T_{exp}/\tau_I \approx 0.06$, meaning negligible reduction in speckle contrast [R131], while each frame is provided an independent pattern. To measure the quality and to quantify the non-uniformity of the speckle contrast maps we use a simpler metric based on Eq. (5.21):

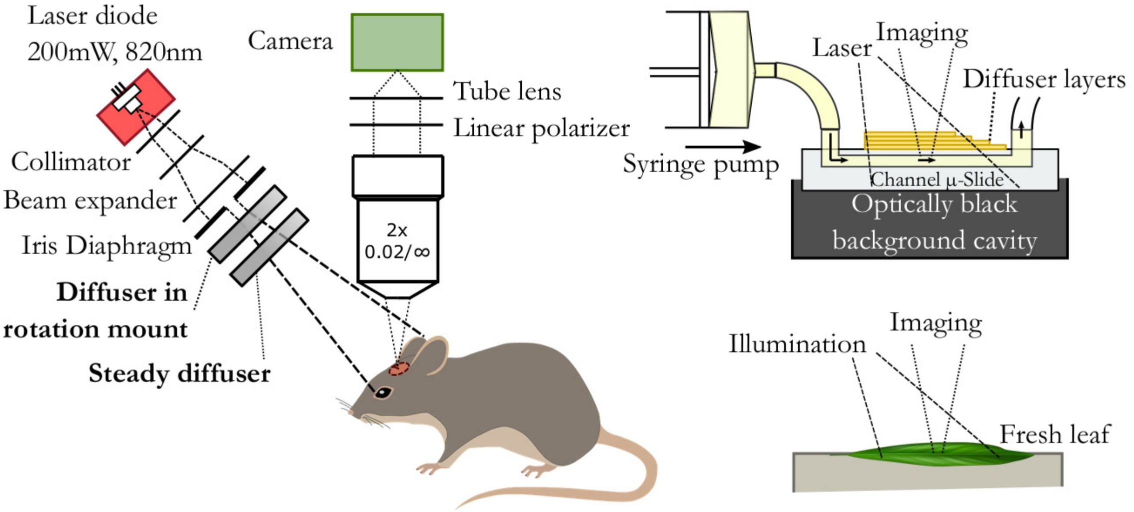

Figure 5.3: The optical arrangements of the illumination and imaging system used in the experiments. The examined targets are a channel phantom, a fresh leaf of ficus benjamina, and the surgically prepared mouse brain surface.

$$\epsilon_K = \frac{\sigma_K}{\mu_K}, \tag{5.19}$$

where ϵ_K, σ_K and μ_K are the standard deviation and mean values of a region of interest of the calculated contrast [R132].

First, we conducted the channel slide experiment to evaluate the effect of ensemble averaging in a controlled environment with known flow speed and changing ρ. A syringe pump (SN-50F6, Sino Medical-Device Technology Co., Ltd., China) drove a 10% emulsion of phospholipid stabilized soybean oil (Intralipid) through a μ-Slide I Luer channel slide of 200 µm channel height (ibidi GmbH, Germany) at 2.0 mm/s speed. The slide was placed on a black beam blocking background cavity in order to avoid multiple reflections and provide optical isolation. The entire channel has been covered uniformly with an $\approx 54\mu m$ thick weak diffuser (Scotch Magic Tape, 3M, USA) with increasing number of layers. During the first measurement the slide was not covered, and one additional layer was applied to the channel slide up step by step after each measurement step, up to 9 layers. In each step, the speckle pattern was recorded for 100-100 frames with an exposure time of 3 ms with stable and decorrelated illumination as well. The spatial speckle contrast (Eq. 5.21) was calculated in a $n_s \times n_s = 7 \times 7$ spatial neighborhood sliding window and then averaged through the frames for $1, 2, ..., N$ times. The non-uniformity of the contrast maps is calculated by Eq. 5.19 using a $n_s \times n_s = 11 \times 11$ spatial window and averaged for each n value. The spatial windows sizes were selected to meet the Nyquist criterion with respect to the speckle size and the spatial contrast pattern. The comparative results are presented in Fig. 5.4.

It can be seen in the figure that the increasing static scatterer ratio (decreasing ρ) contrast map quality does not improve as the number of frames increases using stable illumination (Fig. 5.4(a)). On the other hand, as expected, the decorrelated illumination effectively improves the contrast map (Fig. 5.4(b)). Note, that the data series recorded on static ground glass diffuser of sub speckle sized surface structures and $\rho = 0$ follows the $\propto 1/\sqrt{n}$ improvement rate. This is not the case in a structured scatterer: the decreasing slope of improvement is due to the heterogeneous structure of the used diffuser under the quality metric. Comparing the mean spatial contrasts for the two illumination cases Fig. 5.4(c) suggests that the contrast remains independent of illumination changes. As a

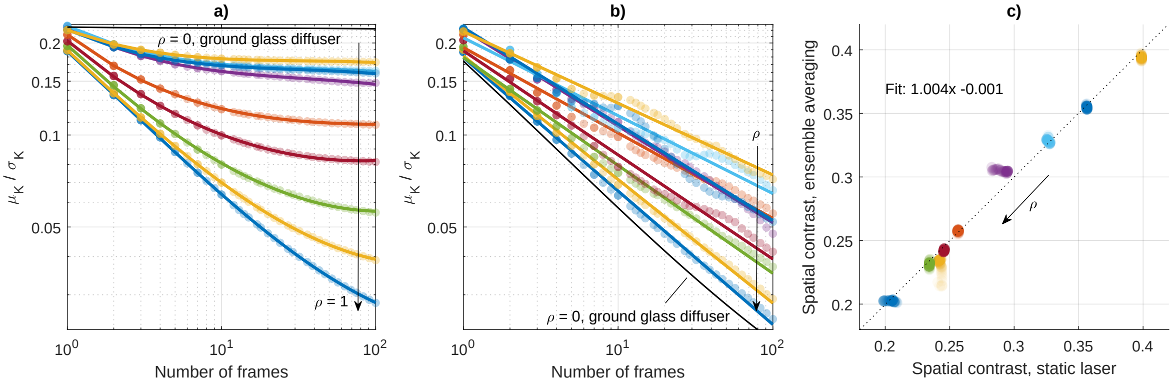

Figure 5.4: The mean quality factor of the channel slide area is calculated with increasing diffuser coverage (decreasing ρ) at constant flow rate 2 mm/s of 10% Intralipid emulsion in a channel slide. Figure (a) shows the quality factor change as a function of the number of averaged contrast maps and ρ with stable illumination. Figure (b) corresponds to the quality factor using decorrelated illumination. Figure (c) maps the mean spatial contrast values of the two illumination cases. In figures (a) and (b) the $\rho = 0$ curves were captured on an ground glass diffuser for comparison.

conclusion, the expected value of the contrast maps does not change, while it becomes less granulated, limited by the scatterer structure.

The model given in Eqs.(5.2)-(5.13) has also been validated on this measurement. The validation is formulated as an identification process with constraints on the ρ factor. Each additional layer of the diffuser is assumed to reduce the ρ factor by a constant $\Delta\rho$ value – as it is illustrated in Fig. 5.5 –, a fully static ($\rho = 0$) and a fully dynamic ($\rho = 1$) sequence is recorded, as well. During the identification beside the model parameters, the $\Delta\rho$ parameter is optimized as follows:

$$\begin{aligned} \min_{\substack{\Delta\rho,\lambda_D,\lambda_S,\\ k_D,\mu_W,\sigma_W}} \quad & \frac{\sum_{n\in\{1,100\}} \sqrt{\frac{1}{n_\rho}\sum_{k=1}^{n_\rho}\left(\Delta\epsilon_K^v(n)\right)^2}}{2\epsilon^v_{K,max}} + \frac{\sqrt{\frac{1}{n_\rho}\sum_{k=1}^{n_\rho}\Delta K_s^2}}{K_{s,max}} \\ \text{s.t.} \quad & \rho = [0, 1 - k\Delta\rho], \\ & k \in (0,9) \subset \mathbb{Z}, \\ & k_D \geq 1, \end{aligned} \tag{5.20}$$

where $n_\rho = 11$ is the number of calculated quality factors and spatial contrasts based on the measurements, $\Delta\epsilon_K^v$ denote the difference between the measured and simulated quality factor, while ΔK_s denote the difference between the spatial contrasts. Furthermore, the quality factors are evaluated at the two extremes ($n = 1$ or $n = 100$), the contributions from the quality factor and spatial contrast are normalized by their maximum values $\epsilon^v_{K,max}$ and $K_{s,max}$, respectively. The results of the identification are summarized in Fig. 5.5.

Next, we conducted an in vivo experiment to investigate the effect of illumination change. First, we deeply anesthetized a mouse (strain: C57BL6/J) with 25 mg/kg xylazine and 125 mg/kg ketamine in 0.9% NaCl mixture, and then we fixed the head of the animal in a stereotaxic frame (Stoelting Inc, USA). Next we made a 1 cm long sagittal incision on the skull, and cleaned the surface with 3% H_2O_2. With a high speed drill we opened the skull and made a 5x5 mm cranial window on the parietal part. The exposure time was 3 ms and 100-100 frames were recorded with each of the two illumination types. The two speckle contrast maps were calculated using $n_s \times n_s = 7 \times 7$ pixels neighborhood and then averaged (Fig. 5.6).

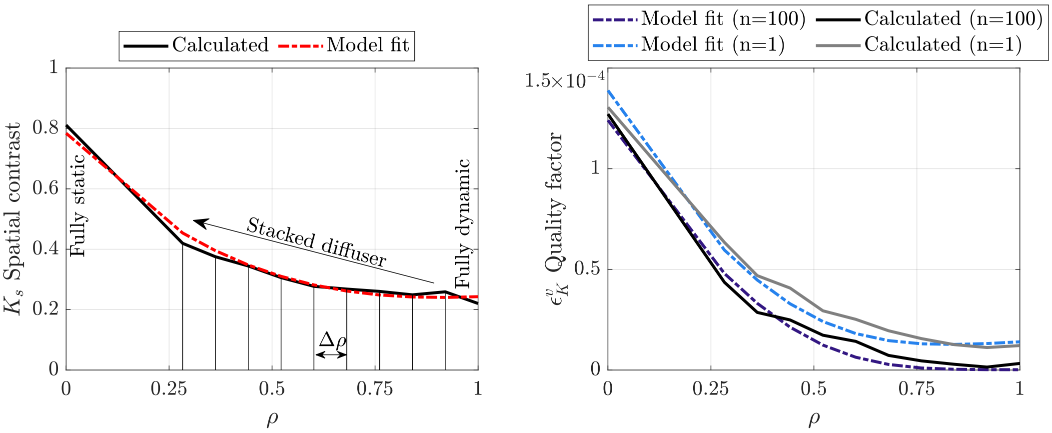

Figure 5.5: The result of the identification is in good agreement with the measured spatial contrast and quality factor. Dashed line represent the output of the model, while the continuous lines are the measured values with linear interpolation between the data points. The identified parameters are as follows: $\Delta\rho = 0.08$, $\lambda_S = 0.0042$, $\lambda_D = 0.01$, $k_D = 17$, $\mu_W = 0.0015$, $\sigma_W = 0.0016$.

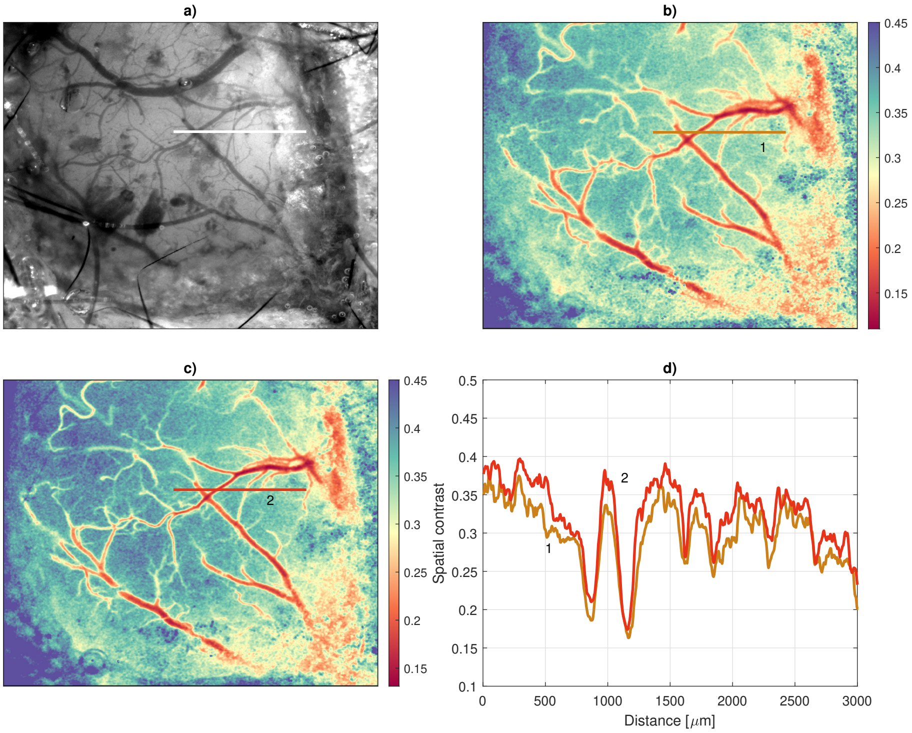

Figure 5.6: Results of the in vivo experiment of the parietal opening of a mouse. Figure (a) brightfield image, (b) averaged spatial speckle contrast map of 100 frames with stable laser illumination, (c) averaged spatial speckle contrast map of the ensemble averaging, (d) cross-sections of (b) and (c) maps along the denoted line. The scale bar is $3\,mm$.

After segmenting the brightfield microscopy view to categories of bone/tissue covered parenchyma, uncovered parenchyma, and vessels, we observed significant qualitative improvement (σ_K/μ_K lowered by $45-50\%$) over the cross section at the partially tissue-covered region when decorrelated illumination was used. On the open surface of parenchyma and arteries/large vessels, the decorrelated illumination showed less improvement: σ_K/μ_K is lowered by $15-20\%$ and $10-15\%$, respectively. The later difference can be originated in more heterogeneous and voluminous organization of the parenchyma and deeper light penetration depth compared to the simpler surface vessel structure.

As a representative example for temporal contrast calculation, we examined the midrib and veins of the underside of a fresh Ficus benjamina leaf (Fig. 5.7(a)). The flow rate varies in the range of a few m/h (<1 mm/s) in the leaves. This slow flow rate does not enable the integral type spatial contrast calculation, thus a moderate sampling rate, short exposure time, and temporal contrast calculation is the appropriate technique to estimate the flow rate [R133]. The exposure time was 10 ms, 100 frames were captured at 20 frames per second and used for temporal contrast calculation. In the reference measurement no diffuser movement was applied as shown in Fig. 5.7(b). During the modified experiment, the diffuser has been moved after every 20 frame and the contrast calculation was restarted. The result was calculated as the average of the contrasts of the whole sequence (Fig. 5.7(c)). The quality factor σ_K/μ_K was reduced significantly (Fig. 5.7(f)), resulting in much less variation. Figure 5.7(d) cross-section compares a line section of the contrasts near a large and narrow vein. We think that the improvement of this technique in imaging setups, with the limit of ergodicity near static scatterers [R134], by partial ensemble averaging is an important observation and worth further investigation. The amount of improvement is similarly to the former experiments, is limited by the volumetric structure of the scatterers.

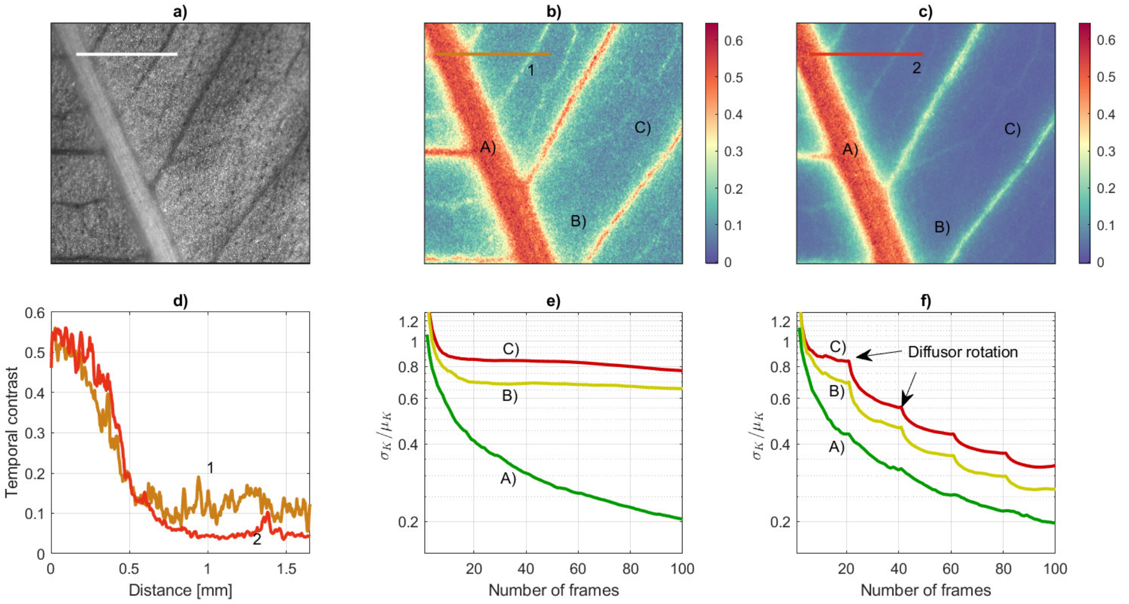

Figure 5.7: Temporal speckle contrast measurement of the underside of a fresh Ficus benjamina leaf. (a) brightfield image, (b) temporal contrast of 100 consecutive frames, (c) average of 5 temporal contrast maps of sequences of 20 frames including diffuser relocation after each sequence. (d) cross-sections of the two (b) and (c) contrast maps. Figures (e-f) show the quality factor of three ROIs for the two cases. The scale bar is $1.5\,mm$.

5.2 Model and compensation of overexposure

LSCI utilizes the statistics of the random speckle pattern based on a measure of contrast κ. As random pattern changes in accordance with the movement of the scatterers, the flow rate $\propto \tau_c$. The different τ_c decorrelation times are then mapped to a contrast map calculated as:

$$\kappa_s^2 = \frac{\sigma^2(I_s)}{\langle I_s \rangle^2}, \tag{5.21}$$

where $\sigma(I_s)^2$ and $\langle I_s \rangle$ are the sample variance and the sample mean calculated in a sliding window of a small neighborhood (e.g $N \times N = 5 \times 5$). The reduced second moment υ_2 depending on T exposure time and τ_c is given in the following model [R103]:

$$\upsilon_2(T, \tau_c) = \frac{\beta}{T^2} \int_0^T \int_0^T \rho |g_1^n(t' - t'')|^2 + (1-\rho)|g_1^n(t' - t'')|^2 dt' dt'', \tag{5.22}$$

where ρ is the ratio of the dynamic scatterers and $(1-\rho)$ is the ratio of the static scatterers to total scatterers, and $t' - t''$ give the time differences during the exposure, β is a normalization factor depending on the speckle size [R135], detector physical resolution and additional factors of the experimental setup [R136, R137]. g_1 is the electric field autocorrelation, which according to [R95] gives us $g_1^n(t) = exp(-(t/\tau_c)^n)$ relation, where τ_c is the correlation time. The value of n depends on the type of flow dynamics [R102]. The contrast values are usually averaged on multiple consecutive frames to improve the signal-to-noise ratio. There are other approaches using temporal or spatiotemporal contrast calculations [R132, R101, R129].

It is important to note, that the outlined methods rely on undistorted speckle patterns, meaning there should be no significant alteration found compared to the ideal Gaussian distribution. Overexposure results in clipped signals and truncated distribution, making the calculations misleading. Our aim was to compensate the saturation effect on contrast calculation during the preprocessing of overexposed speckle patterns.

5.2.1 Effect of signal saturation

Several previous studies [R107, R136, R137] detail the statistical properties of the speckle pattern. Working with biological samples and realistic sensors, the recorded speckle pattern becomes a composite of multiple origins. Three major factors can be distinguished in this composite: a static element, a dynamic element and a factor, which accounts for the camera noise. The static component can be modeled as a single fully developed speckle pattern. The component of interest is the dynamic one, which is described by the integration of the varying speckle pattern in the time domain over a single exposure. The general composite of the factors can be modeled by the sum of three random variables as [R138]:

$$I_s = (1-\rho)S(\lambda_S) + \rho D(\alpha_D, \beta_D) + W, \tag{5.23}$$

where S is a random variable of exponential distribution, representing static scatterers. Dynamic scatterers are described with the random variable D of gamma distribution. The gamma distribution can be defined by $\alpha_D > 0$ shape and $\beta_D > 0$ rate parameters. Camera noise is taken into account as a random variable of normal distribution W and ρ is the ratio of the dynamic scatterers to total scatterers (as in Eq. (5.22)).

We focused only on large signal behavior, thus we simplified by assuming the camera noise to be negligible $W \approx 0$. Since the sum of different multiple gamma distributions can be estimated by a single near gamma distributed gamma-series [R139, R140], we handle I_s as a single one, regardless of static scatterer content. The described model does not include several realistic image acquisition and laser source error phenomena (such as laser bandwidth, pixel cross talk, shoot noise, speckle oversampling). In order to handle these effects, we implemented a numerical approach that is described in the following sections.

Let I_i be the individual samples with gamma distribution, so the probability density function can be described as:

$$f(I_i) = \frac{\beta^\alpha}{\Gamma(\alpha)} I_i^{\alpha-1} e^{-\beta I_i}, \tag{5.24}$$

and the cumulative distribution function is:

$$F(I_i) = \frac{\gamma(\alpha, \beta I_i)}{\Gamma(\alpha)}, \tag{5.25}$$

where $\Gamma(\alpha) = \int_0^\infty t^{\alpha-1} e^{-t} dt$ is the gamma function, and $\gamma(\alpha, \beta I_i) = \int_0^{\beta I_i} t^{\alpha-1} e^{-t} dt$ is the lower incomplete gamma function. In order to calculate the contrast, the expected value and the variance of Eq. (5.24) is needed. The two values are calculated as $E(f) = \alpha/\beta$ and $\sigma^2(f) = \alpha/\beta^2$ based on the contrast calculation equations $\kappa_s^2 = 1/\alpha$ for the unsaturated reference distribution.

Next, we investigated the saturated case by defining it with the following cumulative (truncated) distribution function:

$$F_{sat}(I_i) = \begin{cases} F(I_i), & \text{if } I_i < I_{sat} \\ 1, & \text{otherwise.} \end{cases}, \tag{5.26}$$

where I_{sat} is the saturation threshold. The expected value of the truncated gamma distribution in the undistorted $[0, I_{sat}]$ region is:

$$E(\gamma(\alpha, \beta I_{sat})) = \frac{1}{\beta} \frac{\gamma(\alpha+1, \beta I_{sat})}{\gamma(\alpha, \beta I_{sat})} \tag{5.27}$$

The expected value of the saturated distribution $E(f_{sat})$ can be calculated by weighting the truncated gamma distribution by $F_{sat}(I_i)$ and adding the saturation threshold I_{sat} weighted by $1 - F_{sat}(I_i)$:

$$E(f_{sat}) = \frac{\alpha}{\beta} \frac{\gamma(\alpha+1, \beta I_{sat})}{\Gamma(\alpha+1)} + I_{sat} \left(1 - F_{sat}(I_i)\right) \tag{5.28}$$

Variance is calculated based on the expression of moments $\sigma^2(x) = E(x^2) - E(x)^2$, and that the combined variance is the sum of the individual variances of independent samples:

$$\sigma^2(f_{sat}) = \frac{\alpha}{\beta^2} \frac{\gamma(\alpha+2, \beta I_{sat})}{\Gamma(\alpha+1)} - E(f_{sat})^2 + I_{sat}^2 \big(1 - F_{sat}(I_i)\big). \tag{5.29}$$

The contrast equals to $1/\alpha$ in the limiting case when $I_{sat} \to \infty$, and it becomes zero when $I_{sat} \to 0$.

For completeness, it is important to mention that the quantization of very low intensity values cause a different kind of distortion in the observed contrast values. As it is described in [R141], the effect of the bit depth b on the contrast can be modeled by defining κ^2 corrected contrast:

$$\kappa^2 \approx \kappa_s^2 \left(1 + \frac{I_{sat}}{E(f)(2^b - 1)}\right). \tag{5.30}$$

Eqs. (5.28)-(5.30) enable to simulate and analyze both the effect of under- and overexposure.

5.2.2 Analytical solution for the reference contrast

We refer to the contrast, which we could observe under ideal conditions as the reference contrast. The reference contrast $1/\alpha$ can be calculated by using higher-order partial derivatives of the saturation ratio and sample mean with respect to the saturation threshold (I_{sat}). For ease of notation we introduce saturation ratio R and Y as:

$$R = 1 - F_{sat}(I_i) \tag{5.31}$$

$$Y = E(f_{sat}) - I_{sat}R = \frac{\alpha}{\beta}\frac{\gamma(\alpha+1, \beta I_{sat})}{\Gamma(\alpha+1)} \tag{5.32}$$

Note, that the saturation ratio is equal to the complementary cumulative distribution function (tail distribution). The shape and rate parameters of the distribution can be calculated in the following way:

$$\text{Let} \quad A = \frac{\partial^2 Y}{\partial I_{sat}^2} = \frac{1}{\Gamma(\alpha)}\beta^{\alpha} e^{-\beta I_{sat}}\left[\alpha I_{sat}^{\alpha-1} - I_{sat}^{\alpha}\beta\right], \tag{5.33}$$

$$\text{and let} \quad B = \frac{\partial R}{\partial I_{sat}} = -\frac{1}{\Gamma(\alpha)}\beta^{\alpha} I_{sat}^{\alpha-1} e^{-\beta I_{sat}}, \tag{5.34}$$

$$\text{then} \quad \frac{A}{B} = -\alpha + \beta I_{sat}, \tag{5.35}$$

$$\frac{\partial}{\partial I_{sat}}\frac{A}{B} = \beta, \tag{5.36}$$

$$\left(\frac{\partial}{\partial I_{sat}}\frac{A}{B}\right)I_{sat} - \frac{A}{B} = \alpha \tag{5.37}$$

Though the result is theoretically feasible, it is unsuitable for practical application. First and second order derivatives and their ratio are required for the implementation, which makes the solution sensitive to noise and numerically unstable in the case of small differences. A more consistent result was achieved by defining an iterative method to correct for overexposure. The iterative process is detailed in 5.2.3 and 5.2.4, and was proposed by Péter Földesy.

5.2.3 Simulation

In order to investigate the practical effects of saturation, we performed a thorough image-based numerical simulations using the methods and models presented in [R127], [R128], [R142].

To model a realistic camera and laser source, the following effects are incorporated in the simulations: (i) fixed pattern noise and shot noise modeled by Poisson distribution, (ii) finite bit length data representation by rounding to 12-bit integer, (iii) lateral pixel crosstalk implemented as 7x7 Gaussian kernel, (iv) speckle size, and (v) static scatter content. The simulated wavelength was $\lambda = 820nm$ and the sensor size was 256x256 pixels. The images were scaled with different illumination values, rounded, then normalized to unity by $I_{sat} = 2^{12}$. The saturation effect was modeled by clipping the intensity.

First, speckle patterns were generated with increasing illumination (β rate parameter). The used parameters were $\alpha = 4$, the mean speckle size was 4 pixels, shot noise $\sigma_n = 0.01$, lateral pixel crosstalk $\sigma_p = 0.5$, and $\sigma_\lambda = 3nm$. First, the illumination level (I_{unsat}) was set to the maximum level, where the speckle pattern had no saturated value ($R = 0$). Relative to this value, the intensity was varied in $0.25I_{unsat}$, $1I_{unsat}$, $2.5I_{unsat}$, and $4I_{unsat}$ steps. The resulting images and their probability distributions are presented in Fig. 5.8.

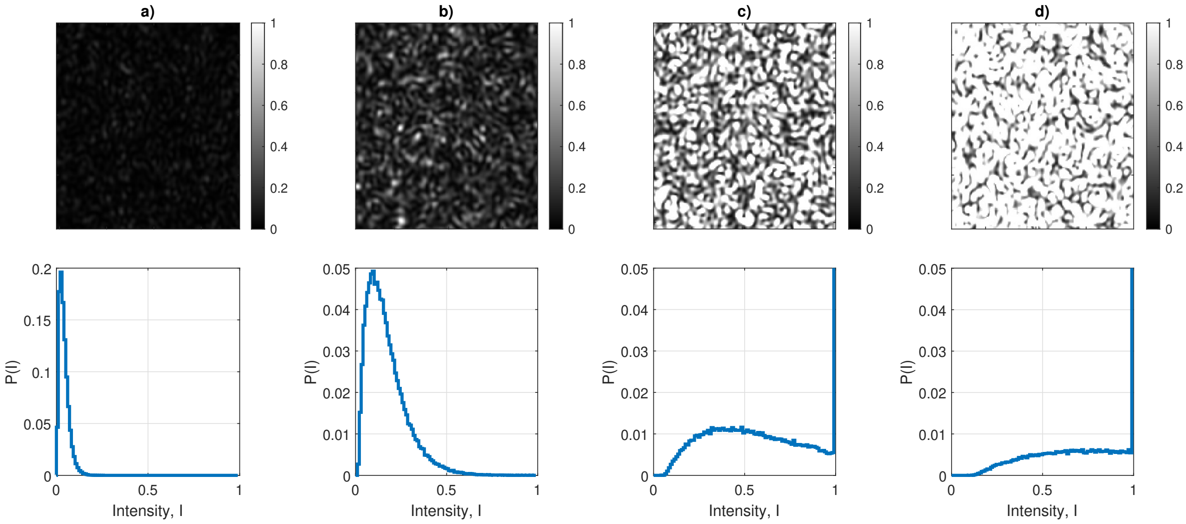

Figure 5.8: Density functions of 256x256 pixels of simulated speckle patterns are shown. The used parameters are $\alpha = 4$, speckle size 4 pixels, shot noise $\sigma_n = 0.01$, lateral pixel crosstalk $\sigma_p = 0.5$, static scatterer $\rho = 0$. Subplot b) shows the speckle pattern at maximum light intensity (I_{unsat}) where no saturation occurred. The subplots a), c), d) correspond to $0.25, 2.5, 4$ times this intensity. The contrast and saturation ratio of the four speckle patterns are $K_s = 0.46, 0.47, 0.41, 0.27$ and $R_s = 0\%, 0\%, 9.1\%, 43.5\%$, respectively.

The detailed relation between the contrast, the observed mean illumination and the saturation ratio is shown in Fig. 5.9. To calculate the saturation ratio R_s, the intensity levels are first binarized; 0 is assigned if there is no saturation, 1 if the pixel value reached I_{sat}. Then, the binary map is averaged in $N \times N$ neighborhoods:

$$R_s = \langle bin(I_i) \rangle, \text{ where} \tag{5.38}$$

$$bin(I_i) = \begin{cases} 0, & \text{if } I_i < I_{sat} \\ 1, & \text{otherwise.} \end{cases} \tag{5.39}$$

It can be seen that the contrast value decreases as more and more pixels become saturated. The reason behind this is that the mean value of the pattern is increasing asymptotically to the saturation level, while the standard deviation is decreasing.

The contrast κ_s can be approximated as a function of the saturation ratio R_s, with a linear and two exponential components:

$$\kappa_s(R_s) \approx p_1 \cdot R_s + p_0 + a_1 e^{-b_1 R_s} - a_2 e^{-b_2(1-R_s)}. \tag{5.40}$$

Figure 5.9c shows the detrended, exponential component only, with contrast values for the same examples.

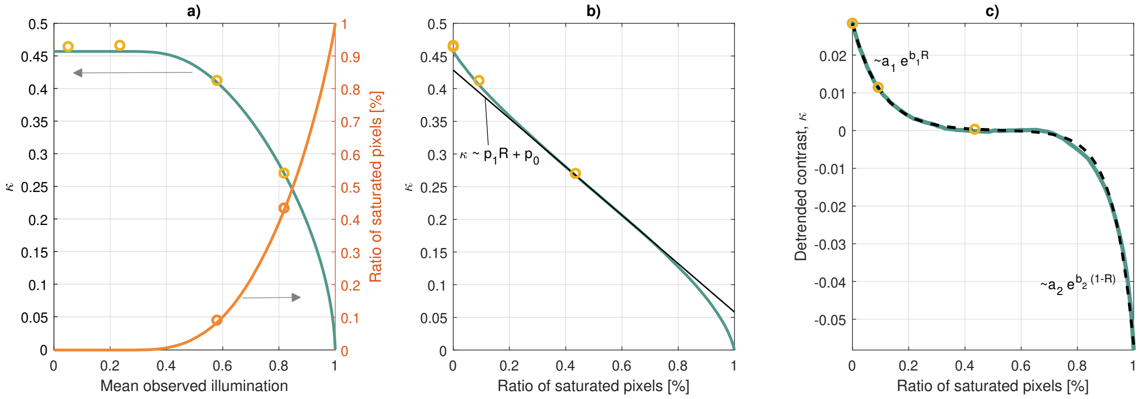

Figure 5.9: Subplot a) shows the contrast values and the saturation ratio as a function of the mean observed illumination. The yellow markers corresponds to the numerical simulation of Fig. 5.8. Subplots b) and c) show the linear and the exponential components of the contrast approximation as a function of the saturation ratio.

Next, we investigated the contrast deterioration as a function of various flow rates and imaging parameters: (i) as a function of α shape parameter, (ii) speckle size, (iii) pixel cross talk and (iv) shot noise. It can be seen in Fig. 5.10 that the main tendency of contrast deterioration does not alter under various scenarios.

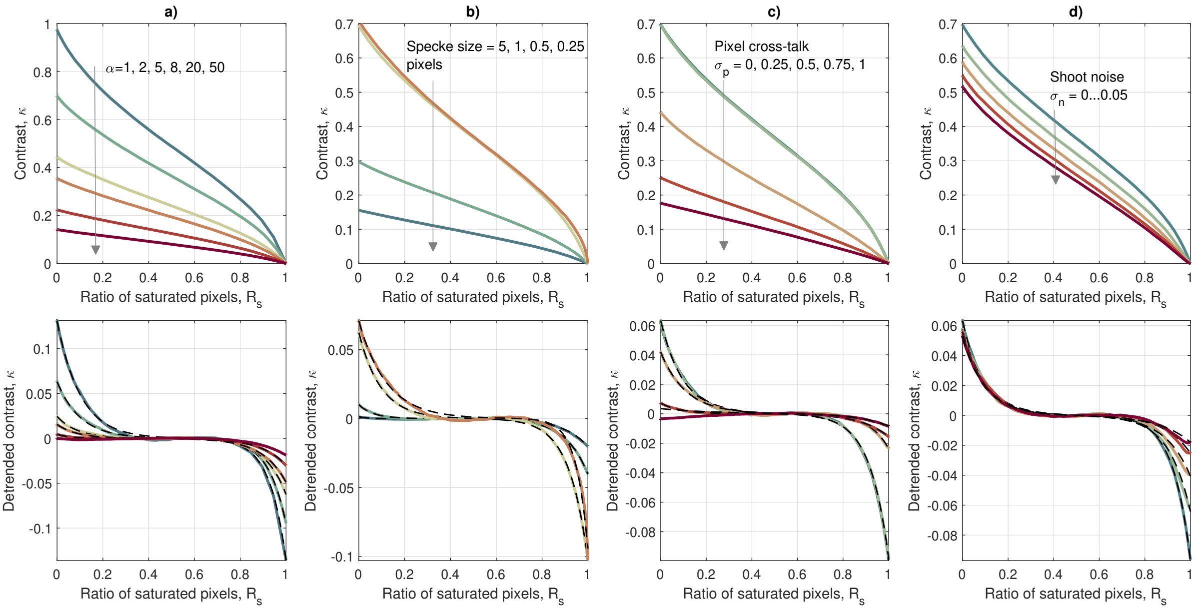

Figure 5.10: The upper subplots show the contrast value as a function of the saturation ratio under various parameter sweeps: shape parameter, speckle size in pixels, pixel crosstalk, and shot noise. In the bottom row, the detrended contrast values are plotted with solid curves and their fitted model (the exponential terms of Eq. (5.40) only) as black dashed curves. While a parameter is changed, the others remained static as $\alpha = 2$, speckle size 4 pixels for subplot a) and speckle size 1 for b-d), shot noise $\sigma_n = 0$, static scatterer ratio $\rho = 0$, lateral pixel crosstalk $\sigma_p = 0.5$.

5.2.4 Correction of overexposure

The goal of this section is to compare the compensation of the contrast distortion of partially saturated images. We demonstrated in the previous sections, that the contrast value decreases as more and more pixels saturate. It can be seen in the detrended contrast curves (Fig. 5.10), which are the exponential components of the fitted values that the low and high saturation sides can differ significantly ($a_1 \neq a_2$ and $b_1 \neq b_2$). The reason for the difference is that the high and low part of the PDF of the intensity is affected differently by various imaging distortions. This observation suggests that a precise extrapolation cannot be done when near half of the pixels are saturated.

Next, we investigate whether the unsaturated case can be estimated by extrapolation from an artificially generated saturation ratio and contrast curve. Such curves, similar to Fig. 5.9 and Fig. 5.10, may be generated from the recorded images by lowering the threshold value step by step, clipping the images and recalculating their contrast maps. The dynamic range of the initial image is limited by the threshold of the sensor as $I_0 \in [0, I_{sat}]$. Let us divide this range into M evenly distributed artificial threshold values. After consecutively clipping the original image at each threshold, we get M contrast κ_i and saturation ratio R_i maps using Eq. (5.21), Eq. (5.38), where $i \in [1, M]$.

We have compared two straightforward function extrapolation strategies. As a reference solution, we fitted the Eq. (5.40) with $M = 7$ threshold levels with constrained nonlinear least-squares optimization. In addition, we explored the near linear behavior of the contrast decreasing in lower contrast cases with a simple and effective linear function.

The presented simulation contained the following parameter settings: $\alpha = 1, 2, 5, 8, 20, 50$, speckle size 2 pixels, shot noise $\sigma_n = 0.01$, lateral pixel cross talk $\sigma_p = 0.5$, static scatterer ratio $\rho = 0.2$.

After parameter fitting, each of them was evaluated at $R_s = 0$ point to get the unsaturated estimate. The simulation was repeated at 100 illumination levels in the range of $0.25 I_{unsat}$ to $5 I_{unsat}$. The outcome is presented in Fig. 5.11a. The Eq. (5.40) based extrapolation method resulted in precise, but slow and noisy estimates.

Next, the contrast κ_s is approximated by a linear function of the saturation ratio and the measured (partially saturated) contrast value:

$$\kappa_{corr,linear} = p_1(\kappa_s, R_s) \cdot R_s + p_0(\kappa_s, R_s). \tag{5.41}$$

In order to further minimize the computational requirements, we took the advantage that setting the threshold level to 0, the resulting contrast becomes 0 at saturation ratio 1, thus there is no need for further contrast calculations in addition to the already known κ_s and R_s. Thus this estimation simplifies to:

$$\kappa_{corr,linear} = \frac{\kappa_s}{1 - R_s}. \tag{5.42}$$

The results are shown in Fig. 5.11b. As expected, this method produced low estimation error at low contrast values where the contrast function is more linear.

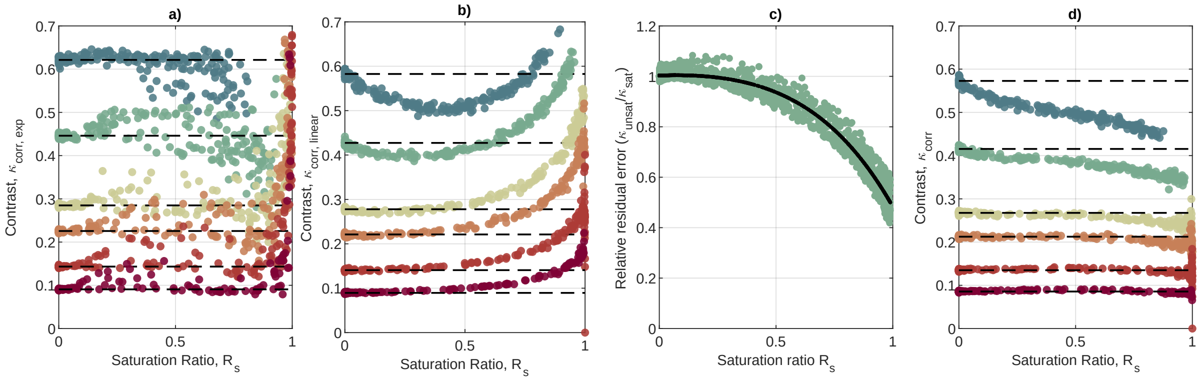

Figure 5.11: Comparison of different extrapolation methods: a) contrast and saturation ratio point pairs are fitted by Eq. (5.40) and evaluated $R_s = 0$; b) linear fitting using Eq. (5.42); c) residual multiplicative error scatter plot and trend of selected, low contrast ($\kappa_s < 0.3$) points; d) linear fitting with residual error correction optimized for low contrast values by Eq. (5.44).

As a continuation, we also analyzed the residual error of the fitting process. Generally, due to the independent distortion sources, error compensation is not feasible, though, for a certain condition range, it is beneficial to reduce the extrapolation imprecision. In order to explore that, multiple simulation setups were used with a wide parameter span. The error was sought as the ratio of the expected and the estimated contrast values $\kappa_{unsat}/\kappa_{corr,linear}$. The relation that describes the error can be derived as the quotient of Eq. (5.40) and Eq. (5.42), and by substituting $R_s = 0$. The quotient can be approximated with good accuracy by a rational function in the range of $R_s \in [0, 1]$ in the following form:

$$\frac{\kappa_{unsat}}{\kappa_{corr,linear}} = \frac{(p_0 + a_1)(1 - R_s)}{p_1 R_s + p_0 + a_1 e^{-b_1 R_s} - a_2 e^{-b_2(1-R_s)}} \approx \frac{1 + c_1 R_s}{1 + q_1 R_s + q_2 R_s^2}. \tag{5.43}$$

The gathered data and the results of the approximate model (Eq. 5.43) is presented in Fig. 5.11c as black dots. For different parameter settings, where the exponential terms of Eq. (5.40) are small the extrapolation error behaved similarly, independently from the actual contrast value. This observation helps to correct some errors of the simple extrapolation for a wide range of setups. As a rule of thumb, low contrast values ($\kappa_s < 0.3 - 0.4$, which corresponds to higher flow rate or long exposure time, small speckle size, etc.) satisfy this condition. Including this term in the correction process, the simplified linear extrapolation becomes:

$$\kappa_{corr} = \frac{\kappa_s}{1 - R_s} \frac{1 + c_1 R_s}{1 + q_1 R_s + q_2 R_s^2}, \tag{5.44}$$

where the parameters are $c_1 = -0.8, q_1 = -0.85, q_2 = 0.25$ for the selected low contrast region. The corresponding corrected curves can be seen in Fig. 5.11d. The simulations of Fig. 5.10 is repeated using Eq.(5.44) and can be seen in Fig. 5.12. The advantage of this form is that it can be evaluated using image operators without pixel-wise fitting routines. Note, to correct the overexposure, κ_s and R_s must be calculated for each image, while c_1, q_1, q_2 only once. On the other hand, the parameters of the correction term may differ for different setups and need to be customized.

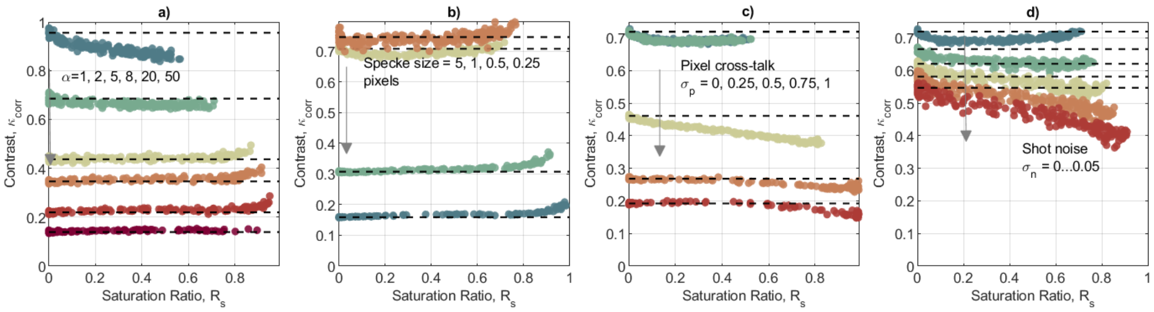

Figure 5.12: Linear extrapolation with residual error corrected repetition of the simulations presented in Fig. 5.10. The dash lines are the expected, unsaturated contrast value levels.

5.2.5 Measurement

In this section, the application of Eq. (5.44) is tested in laboratory experiments. A laser spot was generated by an uncollimated single-mode laser diode driven by a constant current source (RLD82PZJ1, 820 nm central wavelength, 220 mW, ROHM Co., Ltd., Japan). The laser diode was placed in a mount with a thermoelectric cooling stage (LDM9T, Thorlabs, Newton, NJ, USA) and driven by a current generator (LDP-VRM 01-12 CA, Picolas GmbH, Germany). The images were acquired with a 10 cm focal length and f/11 aperture objective and a monochrome camera of 1536x2048 pixels resolution and $3.45x3.45$ µm^2 pixel size (Basler ACA2040-55um, Basler Vision Technologies, Germany). Given the linearly polarized laser diode and an additional static and a rotated linear polarizer (Thorlabs, Newton, NJ, USA) the illumination level was varied in wide range.

The first set of measurements observed a static white carton paper and a small area of the backside of a hand with different exposure times (5, 10, 20 ms) and changing illumination level. The contrast and Eq. (5.44) were calculated in a 7x7 pixels sliding window, than averaged for 2x2 mm^2 area to make a single measurement dot as shown in Fig. 5.13. The points shown in the figure belongs to the original and corrected $1/\kappa_s^2$ values. Working with in vivo samples we found that the contrast and saturation ratio curves tends to be linear, with less non-linearity than the ideal scenarios. As Fig. 5.10 parametric analysis showed, non-idealities separately already result in flattening of the contrast curve. Thus the compensation may be more effective in real applications than the numerical simulations suggest.

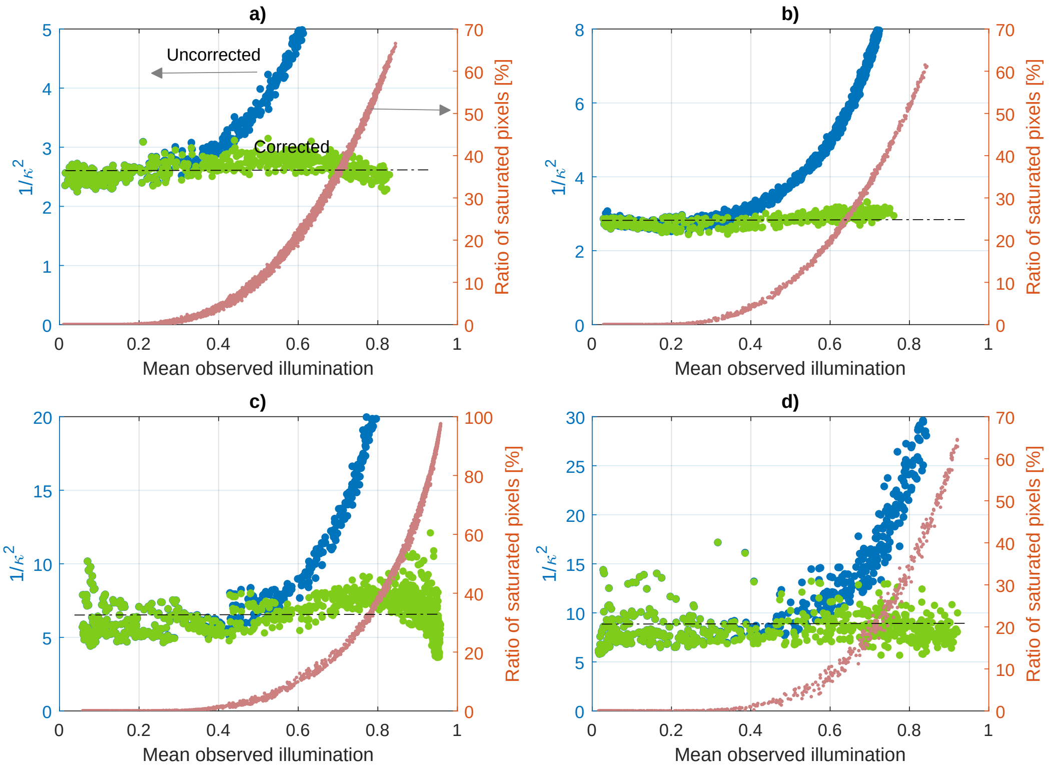

Figure 5.13: Speckle contrast of the same areas at different illumination levels varied in 1:15 ratio. Red dots scaled on the right axis are the ratio of saturating pixels. Scaled on the left axis, the uncorrected values are shown as blue dots, the corrected values as green dots. Subplots show measurements of 2 mm by 2 mm areas of a) static white paper and b-d) back of a hand with 5, 10, and 20 ms exposure times.

As a final experiment, we observed human fingers. 25 frames were taken at 5 ms exposure time first at non-saturating light level, then at three times larger illumination, causing significant area getting overexposured. The spatial contrast is calculated in 11x11 pixels windows and averaged for the frames. Figure 5.14 shows both the uncorrected and corrected perfusion maps.

5.2.6 Discussion

The computational requirement of the presented linear and corrected extrapolation method is slightly above the standard contrast calculations. This may restrict its real time application in time critical applications, such as to visualize blood flow changes in vivo intraoperative situations [R143].

The contrast range reported in practical applications lies in the range of $0.04 < \kappa < 0.6$ restricted by noise, pixel cross-talk, finite laser spatial coherence length and exposition length [R142]. Considering these two limiting cases, we showed that up to 50-60% saturating pixel ratio and low contrast range ($\kappa < 0.3 - 0.4$) simple, linear extrapolation method

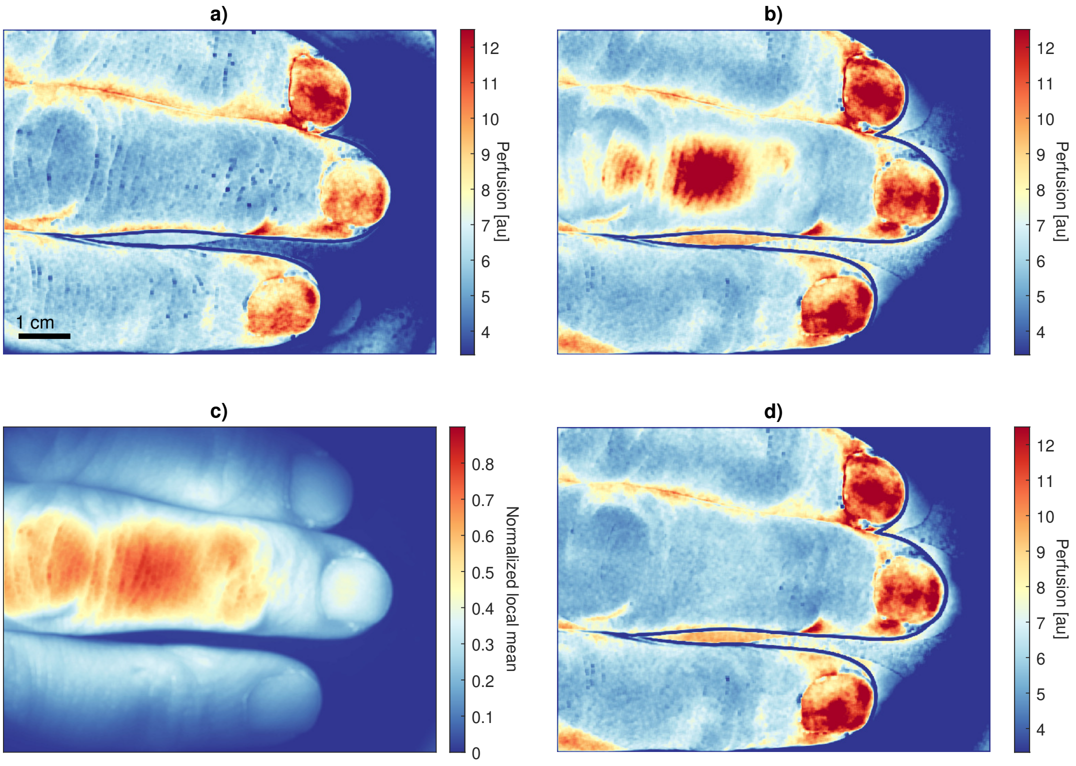

Figure 5.14: Contrast correction of an overexposured image using Eq. (5.44). a) the perfusion map generated at medium illumination. The maximum intensity was set to 50% mean value of the sensor's dynamic range resulting in no saturating pixels. b) perfusion map with overexposured regions using three times higher intensity. Strong distortion can be seen at saturated regions, and better signal to noise ratio at darker areas. c) local mean with color coded saturation (yellow to red areas). d) compensated perfusion map using the proposed linear extrapolation method. The perfusion is estimated as $1/\kappa^2$.

enables external illumination increase with low blood flow index distortion.

5.3 Thesis summary

The signal-to-noise ratio of laser speckle contrast imaging can be improved with taking multiple independent images – also called as ensemble averaging. In [J5], I proposed a model based on statistical distributions which describes how the method depends on the number of captured images and also describes the dependency of static and dynamic scatterers. Differentiating between static and dynamic scatterers is important because taking multiple images improves the signal-to-noise ratio only in terms of the dynamic scatterers. The model was validated in simulations and also on real-world measurements. Exposing properly the image in laser speckle contrast imaging is important to acquire consistent results, overexposing the image distorts the statistical distributions, rendering the observed contrast lower than the contrast of the real distribution. In [J6], we proposed a model which describes the effect of overexposure and I described how it can be used to compensate for overexposed images.

Bibliography

[R1] Home, Resources, Living with diabetes, Acknowledgement, FAQs, Contact, et al. *IDF Diabetes Atlas | Tenth Edition*. en-GB. URL: `https://diabetesatlas.org/`.

[R2] MIchelle Mouri and Madhu Badireddy. "Hyperglycemia". eng. In: *StatPearls*. Treasure Island (FL): StatPearls Publishing, 2023.

[R3] *The History of a Wonderful Thing We Call Insulin | ADA*. URL: `https://diabetes.org/blog/history-wonderful-thing-we-call-insulin` (visited on 04/25/2023).

[R4] Eric Smalley. "Medtronic automated insulin delivery device gets FDA nod". English. In: *Nature Biotechnology* 34.12 (Dec. 2016). Publisher: Nature Publishing Group, pp. 1220–1221. ISSN: 10870156.

[R5] Office of the Commissioner. *FDA authorizes first interoperable, automated insulin dosing controller designed to allow more choices for patients looking to customize their individual diabetes management device system*. en. Publisher: FDA. Mar. 2020.

[R6] Center for Devices and Radiological Health. "MiniMed 770G System - P160017/S076". en. In: *FDA* (Dec. 2020). Publisher: FDA.

[R7] *Omnipod 5 Cleared by the FDA*. en. Jan. 2022. URL: `https://diatribe.org/omnipod-5-approved-fda` (visited on 04/25/2023).

[R8] Jose Garcia-Tirado, Dayu Lv, John P. Corbett, Patricio Colmegna, and Marc D. Breton. "Advanced hybrid artificial pancreas system improves on unannounced meal response - In silico comparison to currently available system". en. In: *Computer Methods and Programs in Biomedicine* 211 (Nov. 2021), p. 106401. ISSN: 0169-2607. DOI: `10.1016/j.cmpb.2021.106401`.

[R9] Su Lim Kang, Yoo Na Hwang, Ji Yean Kwon, and Sung Min Kim. "Effectiveness and safety of a model predictive control (MPC) algorithm for an artificial pancreas system in outpatients with type 1 diabetes (T1D): systematic review and meta-analysis". In: *Diabetology & Metabolic Syndrome* 14.1 (Dec. 2022), p. 187. ISSN: 1758-5996. DOI: `10.1186/s13098-022-00962-2`.

[R10] O A Mennes, J J van Netten, J G van Baal, and W Steenbergen. "Assessment of microcirculation in the diabetic foot with laser speckle contrast imaging". In: 40.6 (July 2019), p. 065002. DOI: `10.1088/1361-6579/ab2058`. URL: `https://doi.org/10.1088/1361-6579/ab2058`.

[R11] Alessandra S. de M. Matheus, Eliete Leão Silva Clemente, Maria de Lourdes Guimarães Rodrigues, Débora Cristina Torres Valença, and Marília B. Gomes. "Assessment of microvascular endothelial function in type 1 diabetes using laser speckle contrast imaging". en. In: *Journal of Diabetes and its Complications* 31.4 (Apr. 2017), pp. 753–757. ISSN: 1056-8727. DOI: `10.1016/j.jdiacomp.2016.12.007`. (Visited on 07/17/2023).

[R12] Perimed AB. *Laser Speckle Contrast Analysis (LASCA)*. en-GB. URL: `https://www.perimed-instruments.com/content/laser-speckle-contrast-analysis-lasca/` (visited on 06/13/2023).

[R13] Ben S. Lertsakdadet, Gordon T. Kennedy, Randolph Stone, Christine Kowalczewski, Andrew C. Kowalczewski, Shanmugasundaram Natesan, et al. "Assessing multimodal optical imaging of perfusion in burn wounds". In: *Burns* (2021). ISSN: 0305-4179. DOI: `https://doi.org/10.1016/j.burns.2021.08.026`. URL: `https://www.sciencedirect.com/science/article/pii/S0305417921002473`.

[R14] K.J. Zheng, E. Middelkoop, M. Stoop, P.P.M. van Zuijlen, and A. Pijpe. "Validity of laser speckle contrast imaging for the prediction of burn wound healing potential". In: *Burns* 48.2 (2022), pp. 319–327. ISSN: 0305-4179. DOI: `https://doi.org/10.1016/j.burns.2021.04.028`.

[R15] Matthijs Draijer, Erwin Hondebrink, Ton van Leeuwen, and Wiendelt Steenbergen. "Review of laser speckle contrast techniques for visualizing tissue perfusion". en. In: *Lasers in Medical Science* 24.4 (July 2009), pp. 639–651. ISSN: 1435-604X. DOI: `10.1007/s10103-008-0626-3`. URL: `https://doi.org/10.1007/s10103-008-0626-3` (visited on 06/13/2023).

[R16] Jorge Bondia, Sergio Romero-Vivó, Beatriz Ricarte, and José-Luis Díez. "Insulin Estimation and Prediction: A Review of the Estimation and Prediction of Subcutaneous Insulin Pharmacokinetics in Closed-Loop Glucose Control". en. In: *IEEE Control Syst.* 38.1 (Feb. 2018), pp. 47–66. ISSN: 1066-033X, 1941-000X. DOI: `10.1109/MCS.2017.2766312`.

[R17] Peter Szalay, Adrienn Molnar, Mark Muller, György Eigner, Imre Rudas, Zoltán Benyó, et al. "Comparison of Sigma-Point Filters for State Estimation of Diabetes Models". In: vol. 2014. Oct. 2014. DOI: `10.1109/smc.2014.6974298`.

[R18] Zeinab Mahmoudi, Kirsten Nørgaard, Niels Kjølstad Poulsen, Henrik Madsen, and John Bagterp Jørgensen. "Fault and meal detection by redundant continuous glucose monitors and the unscented Kalman filter". en. In: *Biomedical Signal Processing and Control* 38 (Sept. 2017), pp. 86–99. ISSN: 1746-8094. DOI: `10.1016/j.bspc.2017.05.004`.

[R19] Luis Omar Avila, Mariano De Paula, and Carlos Roberto Sanchez-Reinoso. "Estimation of plasma insulin concentration under glycemic variability using nonlinear filtering techniques". en. In: *Biosystems* 171 (Sept. 2018), pp. 1–9. ISSN: 0303-2647. DOI: `10.1016/j.biosystems.2018.06.003`.

[R20] Roman Hovorka, Valentina Canonico, Ludovic J Chassin, Ulrich Haueter, Massimo Massi-Benedetti, Marco Orsini Federici, et al. "Nonlinear model predictive control of glucose concentration in subjects with type 1 diabetes". en. In: *Physiol. Meas.* 25.4 (Aug. 2004), pp. 905–920. ISSN: 0967-3334, 1361-6579. DOI: `10.1088/0967-3334/25/4/010`.

[R21] Levente Kovács, György Eigner, Máté Siket, and László Barkai. "Control of Diabetes Mellitus by Advanced Robust Control Solution". In: *IEEE Access* 7 (2019). Conference Name: IEEE Access, pp. 125609–125622. ISSN: 2169-3536. DOI: `10.1109/ACCESS.2019.2938267`.

[R22] Iman Hajizadeh, Mudassir Rashid, Kamuran Turksoy, Sediqeh Samadi, Jianyuan Feng, Nicole Frantz, et al. "Plasma Insulin Estimation in People with Type 1 Diabetes Mellitus". In: *Ind. Eng. Chem. Res.* 56.35 (Sept. 2017), pp. 9846–9857. ISSN: 0888-5885. DOI: `10.1021/acs.iecr.7b01618`.

[R23] R N Bergman, L S Phillips, and C Cobelli. "Physiologic evaluation of factors controlling glucose tolerance in man: measurement of insulin sensitivity and beta-cell glucose sensitivity from the response to intravenous glucose." In: *J Clin Invest* 68.6 (Dec. 1981), pp. 1456–1467. ISSN: 0021-9738.

[R24] Sami S. Kanderian, Stu Weinzimer, Gayane Voskanyan, and Garry M. Steil. "Identification of Intraday Metabolic Profiles during Closed-Loop Glucose Control in Individuals with Type 1 Diabetes". en. In: *J Diabetes Sci Technol* 3.5 (Sept. 2009), pp. 1047–1057. ISSN: 1932-2968, 1932-2968. DOI: `10.1177/193229680900300508`.

[R25] Iván Sala-Mira, José-Luis Díez, Beatriz Ricarte, and Jorge Bondia. "Sliding-mode disturbance observers for an artificial pancreas without meal announcement". en. In: *Journal of Process Control* 78 (June 2019), pp. 68–77. ISSN: 09591524. DOI: `10.1016/j.jprocont.2019.03.008`.

[R26] Boris P. Kovatchev, Marc Breton, Chiara Dalla Man, and Claudio Cobelli. "In Silico Preclinical Trials: A Proof of Concept in Closed-Loop Control of Type 1 Diabetes". In: *Journal of Diabetes Science and Technology* 3.1 (Jan. 2009), pp. 44–55. ISSN: 1932-2968. DOI: `10.1177/193229680900300106`.

[R27] Roberto Visentin, Chiara Dalla Man, and Claudio Cobelli. "One-Day Bayesian Cloning of Type 1 Diabetes Subjects: Toward a Single-Day UVA/Padova Type 1 Diabetes Simulator". In: *IEEE Transactions on Biomedical Engineering* 63.11 (2016), pp. 2416–2424. ISSN: 15582531. DOI: `10.1109/TBME.2016.2535241`.

[R28] Chiara Dalla Man, Michael Camilleri, and Claudio Cobelli. "A system model of oral glucose absorption: Validation on gold standard data". In: *IEEE Transactions on Biomedical Engineering* 53.12 (2006), pp. 2472–2478. ISSN: 00189294. DOI: `10.1109/TBME.2006.883792`.

[R29] Roberto Visentin, Chiara Dalla Man, Boris Kovatchev, and Claudio Cobelli. "The University of Virginia/Padova Type 1 Diabetes Simulator Matches the Glucose Traces of a Clinical Trial". In: *Diabetes Technology & Therapeutics* 16.7 (2014), pp. 428–434. ISSN: 1520-9156. DOI: `10.1089/dia.2013.0377`.

[R30] Jose Garcia-Tirado, Christian Zuluaga-Bedoya, and Marc D. Breton. "Identifiability Analysis of Three Control-Oriented Models for Use in Artificial Pancreas Systems". en. In: *J Diabetes Sci Technol* 12.5 (Sept. 2018), pp. 937–952. ISSN: 1932-2968, 1932-2968. DOI: `10.1177/1932296818788873`.

[R31] Oana-Teodora Chis, Julio R. Banga, and Eva Balsa-Canto. "Structural Identifiability of Systems Biology Models: A Critical Comparison of Methods". en. In: *PLoS ONE* 6.11 (Nov. 2011). Ed. by Johannes Jaeger, e27755. ISSN: 1932-6203. DOI: `10.1371/journal.pone.0027755`.

[R32] Thomas S Ligon, Fabian Fröhlich, Oana T Chi, Julio R Banga, Eva Balsa-Canto, and Jan Hasenauer. "GenSSI 2.0: multi-experiment structural identifiability analysis of SBML models". en. In: *Bioinformatics* 34.8 (Apr. 2018). Ed. by Jonathan Wren, pp. 1421–1423. ISSN: 1367-4803, 1460-2059. DOI: `10.1093/bioinformatics/btx735`.

[R33] Eva Balsa-Canto, David Henriques, Attila Gábor, and Julio R. Banga. "AMIGO2, a toolbox for dynamic modeling, optimization and control in systems biology". en. In: *Bioinformatics* 32.21 (Nov. 2016). Publisher: Oxford Academic, pp. 3357–3359. ISSN: 1367-4803. DOI: `10.1093/bioinformatics/btw411`.

[R34] Roman Hovorka, Fariba Shojaee-Moradie, Paul V. Carroll, Ludovic J. Chassin, Ian J. Gowrie, Nicola C. Jackson, et al. "Partitioning glucose distribution/transport, disposal, and endogenous production during IVGTT". eng. In: *Am. J. Physiol. Endocrinol. Metab.* 282.5 (May 2002), E992–1007. ISSN: 0193-1849. DOI: `10.1152/ajpendo.00304.2001`.

[R35] MatWorks. *Find minimum of function using genetic algorithm - MATLAB ga*. 2019.

[R36] Simon S. Haykin, ed. *Kalman filtering and neural networks*. Adaptive and learning systems for signal processing, communications, and control. New York: Wiley, 2001. ISBN: 978-0-471-36998-1.

[R37] Levente Kovács. "Linear parameter varying (LPV) based robust control of type-I diabetes driven for real patient data". In: *Knowledge-Based Systems* 122 (2017), pp. 199–213.

[R38] Bin Liu. "Particle filtering methods for stochastic optimization with application to large-scale empirical risk minimization". In: *Knowledge-Based Systems* 193 (2020), p. 105486.

[R39] Levente Kovács and György Eigner. "Tensor product model transformation-based parallel distributed control of tumor growth". In: *Acta Polytechnica Hungarica* 15.3 (2018), pp. 1–22.

[R40] Chiara Dalla Man, Francesco Micheletto, Dayu Lv, Marc Breton, Boris Kovatchev, and Claudio Cobelli. "The UVA/PADOVA Type 1 Diabetes Simulator: New Features". en. In: (2014), p. 10. DOI: `10.1177/1932296813514502`.

[R41] Gudmund R. Iversen. "Analysis of Variance". en. In: *International Encyclopedia of Statistical Science*. Ed. by Miodrag Lovric. Berlin, Heidelberg: Springer Berlin Heidelberg, 2011, pp. 44–46. ISBN: 978-3-642-04897-5 978-3-642-04898-2. DOI: `10.1007/978-3-642-04898-2\_117`.

[R42] Peter Sprent. "Sign Test". en. In: *International Encyclopedia of Statistical Science*. Ed. by Miodrag Lovric. Berlin, Heidelberg: Springer Berlin Heidelberg, 2011, pp. 1316–1317. ISBN: 978-3-642-04897-5 978-3-642-04898-2. DOI: `10.1007/978-3-642-04898-2\_515`.

[R43] Sangseok Lee and Dong Kyu Lee. "What is the proper way to apply the multiple comparison test?" In: *Korean J Anesthesiol* 71.5 (Oct. 2018), pp. 353–360. ISSN: 2005-6419. DOI: `10.4097/kja.d.18.00242`.

[R44] Catherine O. Fritz, Peter E. Morris, and Jennifer J. Richler. "Effect size estimates: Current use, calculations, and interpretation". In: *Journal of Experimental Psychology: General* 141.1 (2012). Place: US Publisher: American Psychological Association, pp. 2–18. ISSN: 1939-2222(Electronic),0096-3445(Print). DOI: `10.1037/a0024338`.

[R45] David M. Groppe. "Combating the scientific decline effect with confidence (intervals)". en. In: *Psychophysiology* 54.1 (2017), pp. 139–145. ISSN: 1469-8986. DOI: `10.1111/psyp.12616`.

[R46] *Novorapid Consumer Information*. `https://www.novonordisk.ca/content/dam/Canada/AFFILIATE/www-novonordisk-ca/OurProducts/PDF/novorapid-consumer-information.pdf`. Accessed: 2021-05-10.

[R47] Roland Brun, Peter Reichert, and Hans R. Künsch. “Practical identifiability analysis of large environmental simulation models”. In: *Water Resources Research* 37.4 (2001), pp. 1015–1030. DOI: `https://doi.org/10.1029/2000WR900350`.

[R48] Marcela Moscoso-Vásquez, Patricio Colmegna, and Ricardo S. Sánchez-Peña. “Intra-patient dynamic variations in Type 1 Diabetes: A review”. In: *2016 IEEE Conference on Control Applications (CCA)*. 2016, pp. 416–421. DOI: `10.1109/CCA.2016.7587866`.

[R49] C. Toffanin, E.M. Aiello, S. Del Favero, C. Cobelli, and L. Magni. “Multiple models for artificial pancreas predictions identified from free-living condition data: A proof of concept study”. In: *Journal of Process Control* 77 (2019), pp. 29–37. ISSN: 0959-1524. DOI: `https://doi.org/10.1016/j.jprocont.2019.03.007`.

[R50] L. M. Huyett, E. Dassau, H. C. Zisser, and F. J. Doyle. “Glucose Sensor Dynamics and the Artificial Pancreas: The Impact of Lag on Sensor Measurement and Controller Performance”. In: *IEEE Control Systems Magazine* 38.1 (2018), pp. 30–46. DOI: `10.1109/MCS.2017.2766322`.

[R51] Michele Schiavon, Chiara Dalla Man, Yogish C. Kudva, Ananda Basu, and Claudio Cobelli. “Quantitative Estimation of Insulin Sensitivity in Type 1 Diabetic Subjects Wearing a Sensor-Augmented Insulin Pump”. In: *Diabetes Care* 37.5 (2014), pp. 1216–1223. ISSN: 0149-5992. DOI: `10.2337/dc13-1120`.

[R52] Pablo Abuin, Juan E. Sereno, Antonio Ferramosca, and Alejandro H. Gonzalez. “Closed-loop MPC-based artificial pancreas: Handling circadian variability of insulin sensitivity”. In: *2020 Argentine Conference on Automatic Control (AADECA)*. Oct. 2020, pp. 1–6. DOI: `10.23919/AADECA49780.2020.9301636`.

[R53] Navid Resalat, Wade Hilts, Joseph El Youssef, Nichole Tyler, Jessica R. Castle, and Peter G. Jacobs. “Adaptive Control of an Artificial Pancreas Using Model Identification, Adaptive Postprandial Insulin Delivery, and Heart Rate and Accelerometry as Control Inputs”. en. In: *Journal of Diabetes Science and Technology* 13.6 (2019). Publisher: SAGE Publications Inc, pp. 1044–1053. ISSN: 1932-2968. DOI: `10.1177/1932296819881467`. (Visited on 09/06/2021).

[R54] Roberto Visentin, Chiara Dalla Man, Yogish C. Kudva, Ananda Basu, and Claudio Cobelli. “Circadian Variability of Insulin Sensitivity: Physiological Input for In Silico Artificial Pancreas”. In: *Diabetes Technology & Therapeutics* 17.1 (2015). Publisher: Mary Ann Liebert, Inc., publishers, pp. 1–7. ISSN: 1520-9156.

[R55] Sami S. Kanderian, Stuart A. Weinzimer, and Garry M. Steil. “The Identifiable Virtual Patient Model: Comparison of Simulation and Clinical Closed-Loop Study Results”. en. In: *Journal of Diabetes Science and Technology* 6.2 (Mar. 2012), pp. 371–379. ISSN: 1932-2968, 1932-2968. DOI: `10.1177/193229681200600223`. (Visited on 03/18/2022).

[R56] Peter G. Jacobs, Navid Resalat, Joseph El Youssef, Ravi Reddy, Deborah Branigan, Nicholas Preiser, et al. “Incorporating an Exercise Detection, Grading, and Hormone Dosing Algorithm Into the Artificial Pancreas Using Accelerometry and Heart Rate”. en. In: *Journal of Diabetes Science and Technology* 9.6 (Nov. 2015), pp. 1175–1184. ISSN: 1932-2968, 1932-2968. DOI: `10.1177/1932296815609371`. (Visited on 03/18/2022).

[R57] Mudassir Rashid, Sediqeh Samadi, Mert Sevil, Iman Hajizadeh, Paul Kolodziej, Nicole Hobbs, et al. "Simulation software for assessment of nonlinear and adaptive multivariable control algorithms: Glucoseinsulin dynamics in Type 1 diabetes". en. In: *Computers & Chemical Engineering* 130 (Nov. 2019), p. 106565. ISSN: 00981354. DOI: `10.1016/j.compchemeng.2019.106565`. (Visited on 04/08/2022).

[R58] Iman Hajizadeh, Mudassir Rashid, Sediqeh Samadi, Mert Sevil, Nicole Hobbs, Rachel Brandt, et al. "Adaptive personalized multivariable artificial pancreas using plasma insulin estimates". en. In: *Journal of Process Control* 80 (Aug. 2019), pp. 26–40. ISSN: 0959-1524. DOI: `10.1016/j.jprocont.2019.05.003`. (Visited on 04/11/2022).

[R59] Asbjørn Thode Reenberg, Tobias K. S. Ritschel, Emilie B. Lindkvist, Christian Laugesen, Jannet Svensson, Ajenthen G. Ranjan, et al. "Nonlinear Model Predictive Control and System Identification for a Dual-hormone Artificial Pancreas". en. In: *arXiv:2202.13938 [cs, eess, math]* (Feb. 2022).

[R60] I. Sala, J.L. Díez, and J. Bondia. "Generalized extended state observer design for the estimation of the rate of glucose appearance in artificial pancreas". In: *2018 European Control Conference (ECC)*. June 2018, pp. 2393–2398. DOI: `10.23919/ECC.2018.8550123`.

[R61] J.J. Ormsbee, T. Zhou, J.L. Knopp, and J.G. Chase. "Estimating endogenous glucose production during exercise using heart rate: implications for diabetes management". en. In: *IFAC-PapersOnLine* 54.15 (2021), pp. 478–483. ISSN: 24058963. DOI: `10.1016/j.ifacol.2021.10.302`. (Visited on 03/18/2022).

[R62] University Hospitals of Leicester. *Typical Insulin Profiles*. 2017. URL: `https://www.diabetes.org.uk/resources-s3/2017-10/University%5C%2520Hospitals%5C%2520of%5C%2520Leicester%5C%2520-%5C%2520Insulin%5C%2520Profiles.pdf` (visited on 04/22/2022).

[R63] MATLAB. *version 9.8.0 (R2020a)*. Natick, Massachusetts: The MathWorks Inc., 2020.

[R64] István Lovas. "Fixed Point, Iteration-based, Adaptive Controller Tuning, Using a Genetic Algorithm". In: *Acta Polytechnica Hungarica* 19.2 (2022).

[R65] Marc D. Breton and Boris P. Kovatchev. "One Year Real-World Use of the Control-IQ Advanced Hybrid Closed-Loop Technology". In: *Diabetes Technology & Therapeutics* 23.9 (2021). Publisher: Mary Ann Liebert, Inc., publishers, pp. 601–608. ISSN: 1520-9156. DOI: `10.1089/dia.2021.0097`. (Visited on 01/10/2022).

[R66] Maxwell E. Horowitz, William A. Kaye, Gary M. Pepper, Kathryn E. Reynolds, Shital R. Patel, Kort C. Knudson, et al. "An analysis of Medtronic MiniMed 670G insulin pump use in clinical practice and the impact on glycemic control, quality of life, and compliance". en. In: *Diabetes Research and Clinical Practice* 177 (2021), p. 108876. ISSN: 0168-8227. DOI: `10.1016/j.diabres.2021.108876`.

[R67] A.S. Brazeau, H. Mircescu, K. Desjardins, C. Leroux, I. Strychar, J.M. Ekoé, et al. "Carbohydrate counting accuracy and blood glucose variability in adults with type 1 diabetes". en. In: *Diabetes Research and Clinical Practice* 99.1 (Jan. 2013), pp. 19–23. ISSN: 01688227. DOI: `10.1016/j.diabres.2012.10.024`. URL: `https://linkinghub.elsevier.com/retrieve/pii/S0168822712003919` (visited on 01/07/2022).

[R68] Muskaan Gurnani, Vanita Pais, Kristina Cordeiro, Shawna Steele, Shiyi Chen, and Jill K. Hamilton. "One potato, two potato, assessing carbohydrate counting accuracy in adolescents with type 1 diabetes". en. In: *Pediatric Diabetes* 19.7 (2018). _eprint: https://onlinelibrary.wiley.com/doi/pdf/10.1111/pedi.12717, pp. 1302–1308. ISSN: 1399-5448. DOI: `10.1111/pedi.12717`. URL: `https://onlinelibrary.wiley.com/doi/abs/10.1111/pedi.12717` (visited on 01/07/2022).

[R69] Michaela B. Koontz, Leona Cuttler, Mark R. Palmert, MaryAnn O'Riordan, Elaine A. Borawski, Judy McConnell, et al. "Development and Validation of a Questionnaire to Assess Carbohydrate and Insulin-Dosing Knowledge in Youth With Type 1 Diabetes". In: *Diabetes Care* 33.3 (2009), pp. 457–462. ISSN: 0149-5992. DOI: `10.2337/dc09-0390`. URL: `https://doi.org/10.2337/dc09-0390` (visited on 01/07/2022).

[R70] Chiara Roversi, Martina Vettoretti, Simone Del Favero, Andrea Facchinetti, and Giovanni Sparacino. "Modeling Carbohydrate Counting Error in Type 1 Diabetes Management". eng. In: *Diabetes Technology & Therapeutics* 22.10 (Oct. 2020), pp. 749–759. ISSN: 1557-8593. DOI: `10.1089/dia.2019.0502`.

[R71] Seunghyun Lee, Jiwon Kim, Sung Woon Park, Sang-Man Jin, and Sung-Min Park. "Toward a Fully Automated Artificial Pancreas System Using a Bioinspired Reinforcement Learning Design: In Silico Validation". In: *IEEE Journal of Biomedical and Health Informatics* 25.2 (2021). Conference Name: IEEE Journal of Biomedical and Health Informatics, pp. 536–546. ISSN: 2168-2208. DOI: `10.1109/JBHI.2020.3002022`.

[R72] Ricardo Sanz, Pedro García, José-Luis Díez, and Jorge Bondia. "Artificial Pancreas System With Unannounced Meals Based on a Disturbance Observer and Feedforward Compensation". In: *IEEE Transactions on Control Systems Technology* 29.1 (2021). Conference Name: IEEE Transactions on Control Systems Technology, pp. 454–460. ISSN: 1558-0865. DOI: `10.1109/TCST.2020.2975147`.

[R73] Michael A. Tsoukas, Dorsa Majdpour, Jean-François Yale, Anas El Fathi, Natasha Garfield, Joanna Rutkowski, et al. "A fully artificial pancreas versus a hybrid artificial pancreas for type 1 diabetes: a single-centre, open-label, randomised controlled, crossover, non-inferiority trial". English. In: *The Lancet Digital Health* 3.11 (Nov. 2021). Publisher: Elsevier, e723–e732. ISSN: 2589-7500. DOI: `10.1016/S2589-7500(21)00139-4`.

[R74] David A Copp, Ravi Gondhalekar, and Joao P Hespanha. "Simultaneous model predictive control and moving horizon estimation for blood glucose regulation in type 1 diabetes". In: *Optimal Control Applications and Methods* 39.2 (2018), pp. 904–918.

[R75] Martina Vettoretti, Cristina Battocchio, Giovanni Sparacino, and Andrea Facchinetti. "Development of an Error Model for a Factory-Calibrated Continuous Glucose Monitoring Sensor with 10-Day Lifetime". In: *Sensors* 19.23 (2019). ISSN: 1424-8220. DOI: `10.3390/s19235320`. URL: `https://www.mdpi.com/1424-8220/19/23/5320`.

[R76] Abishek Chandrasekhar and Radhakant Padhi. "Optimization Techniques for Online MPC in Android Smartphones for Artificial Pancreas: A Comparison Study". en. In: *IFAC-PapersOnLine*. 7th International Conference on Advances in Control and Optimization of Dynamical Systems ACODS 2022 55.1 (Jan. 2022), pp. 561–566. ISSN: 2405-8963. DOI: `10.1016/j.ifacol.2022.04.092`.

[R77] Lucas de P. Veronese and Renato A. Krohling. “Differential evolution algorithm on the GPU with C-CUDA”. In: *IEEE Congress on Evolutionary Computation*. ISSN: 1941-0026. July 2010, pp. 1–7. DOI: `10.1109/CEC.2010.5586219`.

[R78] Luca Mussi, Fabio Daolio, and Stefano Cagnoni. “Evaluation of parallel particle swarm optimization algorithms within the CUDA architecture”. en. In: *Information Sciences*. Special Issue on Interpretable Fuzzy Systems 181.20 (Oct. 2011), pp. 4642–4657. ISSN: 0020-0255. DOI: `10.1016/j.ins.2010.08.045`. (Visited on 06/17/2022).

[R79] Bence Tamás Tóth and Sándor Szénási. “Tree Growth Simulation based on Ray-Traced Lights Modelling”. en. In: *Acta Polytechnica Hungarica* 17.4 (2020), pp. 221–237. ISSN: 17858860, 20642687. DOI: `10.12700/APH.17.4.2020.4.12`. URL: `http://acta.uni-obuda.hu/Toth_Szenasi_101.pdf` (visited on 07/11/2022).

[R80] Hongyan Guo, Dongpu Cao, Hong Chen, Zhenping Sun, and Yunfeng Hu. “Model predictive path following control for autonomous cars considering a measurable disturbance: Implementation, testing, and verification”. en. In: *Mechanical Systems and Signal Processing* 118 (Mar. 2019), pp. 41–60. ISSN: 0888-3270. DOI: `10.1016/j.ymssp.2018.08.028`.

[R81] Peter Kühl, Moritz Diehl, Tom Kraus, Johannes P. Schlöder, and Hans Georg Bock. “A real-time algorithm for moving horizon state and parameter estimation”. en. In: *Computers & Chemical Engineering* 35.1 (Jan. 2011), pp. 71–83. ISSN: 00981354. DOI: `10.1016/j.compchemeng.2010.07.012`.

[R82] Thibault Duranton. *The counter-intuitive rise of Python in scientific computing*. en. [Accessed Aug. 5, 2022]. July 2020. URL: `https://cerfacs.fr/coop/fortran-vs-python`.

[R83] Siu Kwan Lam, Antoine Pitrou, and Stanley Seibert. “Numba: a LLVM-based Python JIT compiler”. In: *Proceedings of the Second Workshop on the LLVM Compiler Infrastructure in HPC*. LLVM ’15. New York, NY, USA: Association for Computing Machinery, 2015, pp. 1–6. ISBN: 978-1-4503-4005-2. DOI: `10.1145/2833157.2833162`. (Visited on 06/13/2022).

[R84] Charles R. Harris, K. Jarrod Millman, Stéfan J. van der Walt, Ralf Gommers, Pauli Virtanen, David Cournapeau, et al. “Array programming with NumPy”. In: *Nature* 585.7825 (Sept. 2020), pp. 357–362. DOI: `10.1038/s41586-020-2649-2`. URL: `https://doi.org/10.1038/s41586-020-2649-2`.

[R85] Pauli Virtanen, Ralf Gommers, Travis E. Oliphant, Matt Haberland, Tyler Reddy, David Cournapeau, et al. “SciPy 1.0: Fundamental Algorithms for Scientific Computing in Python”. In: *Nature Methods* 17 (2020), pp. 261–272. DOI: `10.1038/s41592-019-0686-2`.

[R86] Google. *Google Colab*. [Accessed Aug. 5, 2022]. URL: `https://research.google.com/colaboratory/faq.html`.

[R87] Gradient. *Gradient - Machine Learning Platform | Paperspace*. en. URL: `https://docs.paperspace.com/gradient/` (visited on 06/15/2022).

[R88] Rainer Storn and Kenneth Price. “Differential Evolution A Simple and Efficient Heuristic for global Optimization over Continuous Spaces”. en. In: *Journal of Global Optimization* 11.4 (Dec. 1997), pp. 341–359. ISSN: 1573-2916. DOI: `10.1023/A:1008202821328`. (Visited on 06/15/2022).

[R89] *Nsight Compute*. en-us. concept. Archive Location: Nsight Compute. URL: `https://docs.nvidia.com/nsight-compute/NsightCompute/index.html` (visited on 06/23/2022).

[R90] Pengcheng Li, Songlin Ni, Li Zhang, Shaoqun Zeng, and Qingming Luo. "Imaging cerebral blood flow through the intact rat skull with temporal laser speckle imaging". In: *Optics Letters* 31.12 (2006), pp. 1824–1826. DOI: `10.1364/ol.31.001824`.

[R91] Michael A Taylor, Tobias Nöbauer, Alejandro Pernia-Andrade, Friederike Schlumm, and Alipasha Vaziri. "Brain-wide 3D light-field imaging of neuronal activity with speckle-enhanced resolution". In: *Optica* 5.4 (2018), pp. 345–353.

[R92] Bernard Choi, Nicole M. Kang, and J.Stuart Nelson. "Laser speckle imaging for monitoring blood flow dynamics in the in vivo rodent dorsal skin fold model". In: *Microvascular Research* 68.2 (2004), pp. 143–146. DOI: `10.1016/j.mvr.2004.04.003`.

[R93] Corey Zheng, Lung Wai Lau, and Jaepyeong Cha. "Dual-display laparoscopic laser speckle contrast imaging for real-time surgical assistance". In: *Biomedical optics express* 9.12 (2018), pp. 5962–5981.

[R94] Haiying Cheng and Timothy Q. Duong. "Simplified laser-speckle-imaging analysis method and its application to retinal blood flow imaging". In: *Optics Letters* 32.15 (2007), pp. 2188–2190. DOI: `10.1364/ol.32.002188`.

[R95] A.F. Fercher and J.D. Briers. "Flow visualization by means of single-exposure speckle photography". In: *Optics Communications* 37.5 (1981), pp. 326–330. DOI: `10.1016/0030-4018(81)90428-4`.

[R96] Ashwin B. Parthasarathy, W. J. Tom, Ashwini Gopal, Xiaojing Zhang, and Andrew K. Dunn. "Robust flow measurement with multi-exposure speckle imaging". In: *Optics Express* 16.3 (2008), pp. 1975–1989. DOI: `10.1364/oe.16.001975`.

[R97] Tanja Dragojevi, Danilo Bronzi, Hari M. Varma, Claudia P. Valdes, Clara Castellvi, Federica Villa, et al. "High-speed multi-exposure laser speckle contrast imaging with a single-photon counting camera". In: *Biomedical Optics Express* 6.8 (2015), pp. 2865–2876. DOI: `10.1364/boe.6.002865`.

[R98] Pavel Zakharov, Andreas Völker, Alfred Buck, Bruno Weber, and Frank Scheffold. "Quantitative modeling of laser speckle imaging". In: *Optics Letters* 31.23 (2006), pp. 3465–3467. DOI: `10.1364/ol.31.003465`.

[R99] Chenge Wang, Zili Cao, Xin Jin, Weihao Lin, Yang Zheng, Bixin Zeng, et al. "Robust quantitative single-exposure laser speckle imaging with true flow speckle contrast in the temporal and spatial domains". In: *Biomedical Optics Express* 10.8 (2019), pp. 4097–4114. DOI: `10.1364/boe.10.004097`.

[R100] Oliver Thompson, Michael Andrews, and Evan Hirst. "Correction for spatial averaging in laser speckle contrast analysis". In: *Biomedical optics express* 2.4 (2011), pp. 1021–1029.

[R101] Haiying Cheng, Qingming Luo, Shaoqun Zeng, Shangbin Chen, Jian Cen, and Hui Gong. "Modified laser speckle imaging method with improved spatial resolution". In: *Journal of biomedical optics* 8.3 (2003), pp. 559–565.

[R102] Dmitry D. Postnov, Jianbo Tang, Sefik Evren Erdener, Kvlcm Klç, and David A. Boas. "Dynamic light scattering imaging". In: *Science Advances* 6.45 (2020), eabc4628. DOI: `10.1126/sciadv.abc4628`.

[R103] R. Bandyopadhyay, A. S. Gittings, S. S. Suh, P. K. Dixon, and D. J. Durian. "Speckle-visibility spectroscopy: A tool to study time-varying dynamics". In: *Review of Scientific Instruments* 76.9 (2005). DOI: `10.1063/1.2037987`.

[R104] Yuemei Zhao, Kang Wang, Weitao Li, Huan Zhang, Zhiyu Qian, and Yangyang Liu. "Laser speckle contrast imaging system using nanosecond pulse laser source". In: *Journal of Biomedical Optics* 25.05 (2020), pp. 1–10. DOI: `10.1117/1.jbo.25.5.056005`.

[R105] Shuai Yuan, Anna Devor, David A Boas, and Andrew K Dunn. "Determination of optimal exposure time for imaging of blood flow changes with laser speckle contrast imaging". In: *Applied optics* 44.10 (2005), pp. 1823–1830.

[R106] David A. Boas and Andrew K. Dunn. "Laser speckle contrast imaging in biomedical optics". In: *Journal of Biomedical Optics* 15.1 (2010), p. 011109. DOI: `10.1117/1.3285504`.

[R107] Joseph W Goodman. "Statistical properties of laser speckle patterns". In: *Laser speckle and related phenomena*. Springer, 1975, pp. 9–75.

[R108] Ronald L. Iman. "Latin Hypercube Sampling". In: *Wiley StatsRef: Statistics Reference Online*. American Cancer Society, 2014. ISBN: 9781118445112. DOI: `10.1002/9781118445112.stat03803`. eprint: `https://onlinelibrary.wiley.com/doi/pdf/10.1002/9781118445112.stat03803`. URL: `https://onlinelibrary.wiley.com/doi/abs/10.1002/9781118445112.stat03803`.

[R109] MASAHIRO Ikeda. "Switching characteristics of laser diode switch". In: *IEEE Journal of Quantum Electronics* 19.2 (1983), pp. 157–164.

[R110] Oliver Thompson, Michael Andrews, and Evan Hirst. "Correction for spatial averaging in laser speckle contrast analysis". In: *Biomed. Opt. Express* 2.4 (Apr. 2011), pp. 1021–1029. DOI: `10.1364/BOE.2.001021`. URL: `http://www.osapublishing.org/boe/abstract.cfm?URI=boe-2-4-1021`.

[R111] Lipei Song and Daniel S. Elson. "Effect of signal intensity and camera quantization on laser speckle contrast analysis". In: *Biomed. Opt. Express* 4.1 (Jan. 2013), pp. 89–104. DOI: `10.1364/BOE.4.000089`. URL: `http://opg.optica.org/boe/abstract.cfm?URI=boe-4-1-89`.

[R112] Hamza Khan and Jozsef K Tar. "On the Implementation of Fixed Point Iteration-based Adaptive Receding Horizon Control for Multiple Degree of Freedom, Higher Order Dynamical Systems". In: *Acta Polytechnica Hungarica* 16.9 (2019), p. 20.

[R113] Abdulrahman J. Babqi and Basem Alamri. "A Comprehensive Comparison between Finite Control Set Model Predictive Control and Classical Proportional-Integral Control for Grid-tied Power Electronics Devices". en. In: *Acta Polytechnica Hungarica* 18.7 (2021), pp. 67–87. ISSN: 17858860, 20642687. DOI: `10.12700/APH.18.7.2021.7.4`. URL: `http://acta.uni-obuda.hu/Babqi_Alamri_114.pdf` (visited on 09/29/2022).

[R114] Raul-Cristian Roman, Radu-Emil Precup, Elena-Lorena Hedrea, Stefan Preitl, Iuliu Alexandru Zamfirache, Claudia-Adina Bojan-Dragos, et al. "Iterative Feedback Tuning Algorithm for Tower Crane Systems". In: *Procedia Computer Science* 199 (2022), pp. 157–165. ISSN: 1877-0509. DOI: `https://doi.org/10.1016/j.procs.2022.01.020`. URL: `https://www.sciencedirect.com/science/article/pii/S1877050922000205`.

[R115] Hemza Redjimi and József K. Tar. "Multiple Components Fixed Point Iteration in the Adaptive Control of Single Variable 2nd Order Systems". In: *Acta Polytechnica Hungarica* 18.9 (2021), pp. 69–86. ISSN: 17858860, 20642687. DOI: `10.12700/APH.18.9.2021.9.5`. URL: `http://acta.uni-obuda.hu/Redjimi_Tar_116.pdf` (visited on 09/29/2022).

[R116] Máté Siket, Imre Jánoki, Kornél Demeter, Miklós Szabó, and Péter Földesy. "Time varied illumination laser speckle contrast imaging". In: *Opt. Lett.* 46.4 (Feb. 2021), pp. 713–716. DOI: `10.1364/OL.413767`. URL: `http://www.osapublishing.org/ol/abstract.cfm?URI=ol-46-4-713`.

[R117] Steven G. Johnson. "The NLopt nonlinear-optimization package". In: (). `https://github.com/stevengj/nlopt`.

[R118] Andreas C Völker, Pavel Zakharov, B Weber, F Buck, and Frank Scheffold. "Laser speckle imaging with an active noise reduction scheme". In: *Optics Express* 13.24 (2005), pp. 9782–9787.

[R119] Tim Stangner, Hanqing Zhang, Tobias Dahlberg, Krister Wiklund, and Magnus Andersson. "Step-by-step guide to reduce spatial coherence of laser light using a rotating ground glass diffuser". In: *Applied optics* 56.19 (2017), pp. 5427–5435.

[R120] M Nadeem Akram, Zhaomin Tong, Guangmin Ouyang, Xuyuan Chen, and Vladimir Kartashov. "Laser speckle reduction due to spatial and angular diversity introduced by fast scanning micromirror". In: *Applied optics* 49.17 (2010), pp. 3297–3304.

[R121] León Schweickhardt, Andreas Tausendfreund, Dirk Stöbener, and Andreas Fischer. "Noise reduction in high-resolution speckle displacement measurements through ensemble averaging". In: *Applied Optics* 60.7 (2021), pp. 1871–1880.

[R122] Hira Nasim and Yasir Jamil. "Recent advancements in spectroscopy using tunable diode lasers". In: *Laser Physics Letters* 10.4 (2013), p. 043001.

[R123] Xuyuan Chen, Øyvind Svensen, and Muhammad Nadeem Akram. "Speckle reduction in laser projection using a dynamic deformable mirror". In: *Optics express* 22.9 (2014), pp. 11152–11166.

[R124] M Elbaum, M Greenebaum, and M King. "A wavelength diversity technique for reduction of speckle size". In: *Optics Communications* 5.3 (1972), pp. 171–174.

[R125] K.M. Ramachandran and C.P. Tsokos. *Mathematical Statistics with Applications*. Elsevier Science, 2009. ISBN: 9780080951706. URL: `https://books.google.hu/books?id=YFyhXk-ONWwC`.

[R126] J.A. Rice. *Mathematical Statistics and Data Analysis*. Advanced series. Cengage Learning, 2006. ISBN: 9780534399429.

[R127] Lipei Song, Zhen Zhou, Xueyan Wang, Xing Zhao, and Daniel S Elson. "Simulation of speckle patterns with pre-defined correlation distributions". In: *Biomedical optics express* 7.3 (2016), pp. 798–809.

[R128] Hendrik Spahr, Clara Pfäffle, Sazan Burhan, Lisa Kutzner, Felix Hilge, Gereon Hüttmann, et al. "Phase-sensitive interferometry of decorrelated speckle patterns". In: *Scientific reports* 9.1 (2019), pp. 1–15.

[R129] Julio C Ramirez-San-Juan, Caitlin Regan, Beatriz Coyotl-Ocelotl, and Bernard Choi. "Spatial versus temporal laser speckle contrast analyses in the presence of static optical scatterers". In: *Journal of biomedical optics* 19.10 (2014), p. 106009.

[R130] Máté Siket, Imre Jánoki, Kornél Demeter, Miklós Szabó, and Péter Földesy. "Time varied illumination laser speckle contrast imaging". In: *Optics Letters* 46.4 (2021), pp. 713–716.

[R131] Dayan Li, Damien P Kelly, and John T Sheridan. "Speckle suppression by doubly scattering systems". In: *Applied optics* 52.35 (2013), pp. 8617–8626.

[R132] Jianjun Qiu, Pengcheng Li, Weihua Luo, Jia Wang, Hongyan Zhang, and Qingming Luo. “Spatiotemporal laser speckle contrast analysis for blood flow imaging with maximized speckle contrast”. In: *Journal of biomedical optics* 15.1 (2010), p. 016003.

[R133] Piotr Mariusz Pieczywek, Justyna Cybulska, Artur Zdunek, and Andrzej Kurenda. “Exponentially smoothed Fujii index for online imaging of biospeckle spatial activity”. In: *Computers and Electronics in Agriculture* 142 (2017), pp. 70–78.

[R134] Pavel Zakharov. “Ergodic and non-ergodic regimes in temporal laser speckle imaging”. In: *Optics letters* 42.12 (2017), pp. 2299–2301.

[R135] Jianjun Qiu, Yangyang Li, Qin Huang, Yang Wang, and Pengcheng Li. “Correcting speckle contrast at small speckle size to enhance signal to noise ratio for laser speckle contrast imaging”. In: *Optics express* 21.23 (2013), pp. 28902–28913.

[R136] Donald D Duncan, Sean J Kirkpatrick, and Ruikang K Wang. “Statistics of local speckle contrast”. In: *JOSA A* 25.1 (2008), pp. 9–15.

[R137] Yong Su, Qingchuan Zhang, and Zeren Gao. “Statistical model for speckle pattern optimization”. In: *Optics express* 25.24 (2017), pp. 30259–30275.

[R138] Péter Földesy, Máté Siket, Imre Jánoki, Kornél Demeter, and Ádám Nagy. “Ensemble averaging laser speckle contrast imaging: statistical model of improvement as function of static scatterers”. In: *Opt. Express* 29.18 (Aug. 2021), pp. 29366–29377. DOI: `10.1364/OE.428394`. URL: `http://www.osapublishing.org/oe/abstract.cfm?URI=oe-29-18-29366`.

[R139] Shai Covo and Amir Elalouf. “A novel single-gamma approximation to the sum of independent gamma variables, and a generalization to infinitely divisible distributions”. In: *Electronic Journal of Statistics* 8.1 (2014), pp. 894–926.

[R140] Peter G Moschopoulos. “The distribution of the sum of independent gamma random variables”. In: *Annals of the Institute of Statistical Mathematics* 37.3 (1985), pp. 541–544.

[R141] Lipei Song and Daniel S Elson. “Effect of signal intensity and camera quantization on laser speckle contrast analysis”. In: *Biomedical optics express* 4.1 (2013), pp. 89–104.

[R142] Dmitry D Postnov, Xiaojun Cheng, Sefik Evren Erdener, and David A Boas. “Choosing a laser for laser speckle contrast imaging”. In: *Scientific reports* 9.1 (2019), pp. 1–6.

[R143] Antonella Mangraviti, Francesco Volpin, Jaepyeong Cha, Samantha I Cunningham, Karan Raje, M Jason Brooke, et al. “Intraoperative laser speckle contrast imaging for real-time visualization of cerebral blood flow in cerebrovascular surgery: results from pre-clinical studies”. In: *Scientific reports* 10.1 (2020), pp. 1–13.

Own Publications Pertaining to Theses

[J1] Levente Kovács, György Eigner, Máté Siket, and László Barkai. “Control of Diabetes Mellitus by Advanced Robust Control Solution”. In: *IEEE Access* 7 (2019). Conference Name: IEEE Access, pp. 125609–125622. ISSN: 2169-3536. DOI: `10.1109/ACCESS.2019.2938267`.

[J2] Iván Sala-Mira, Máté Siket, Levente Kovács, György Eigner, and Jorge Bondia. “Effect of Model, Observer and Their Interaction on State and Disturbance Estimation in Artificial Pancreas: An In-Silico Study”. In: *IEEE Access* 9 (2021). ISSN: 2169-3536. DOI: `10.1109/ACCESS.2021.3120880`.

[J3] Máté Siket, Imre Jánoki, Kornél Demeter, Miklós Szabó, and Péter Földesy. “Time varied illumination laser speckle contrast imaging”. EN. In: *Optics Letters* 46.4 (2021). Publisher: Optica Publishing Group, pp. 713–716. ISSN: 1539-4794. DOI: `10.1364/OL.413767`. URL: `https://opg.optica.org/ol/abstract.cfm?uri=ol-46-4-713`.

[J4] Máté Siket, Imre Jánoki, Ádám Nagy, and Péter Földesy. “Sample-in-the-Loop Laser Speckle Contrast Imaging Based on Optimization”. en. In: *Acta Polytechnica Hungarica* 20.2 (2023).

[J5] Péter Földesy, Máté Siket, Imre Jánoki, Kornél Demeter, and Ádám Nagy. “Ensemble averaging laser speckle contrast imaging: statistical model of improvement as function of static scatterers”. In: *Optics Express* 29.18 (2021). Publisher: Optica Publishing Group, pp. 29366–29377. ISSN: 1094-4087. DOI: `10.1364/OE.428394`.

[J6] Péter Földesy, Máté Siket, Ádám Nagy, and Imre Jánoki. “Correction of overexposure in laser speckle contrast imaging”. EN. In: *Optics Express* 30.12 (2022). Publisher: Optica Publishing Group, pp. 21523–21534. ISSN: 1094-4087. DOI: `10.1364/OE.451611`. URL: `https://opg.optica.org/oe/abstract.cfm?uri=oe-30-12-21523`.

[C1] Levente Kovács, Máté Siket, Imre Rudas, Anikó Szakál, and György Eigner. “Discrete LPV Based Parameter Estimation For TIDM Patients By Using Dual Extended Kalman Filtering Method”. In: *2019 IEEE International Conference on Systems, Man and Cybernetics (SMC)*. ISSN: 2577-1655. Oct. 2019, pp. 1390–1395. DOI: `10.1109/SMC.2019.8914014`.

[C2] I. Sala-Mira, M. Siket, Gy. Eigner, J. Bondia, and L. Kovacs. “Kalman filter and sliding mode observer in artificial pancreas: an in-silico comparison”. en. In: *IFAC-PapersOnLine*. 21st IFAC World Congress 53.2 (Jan. 2020), pp. 16227–16232. ISSN: 2405-8963. DOI: `10.1016/j.ifacol.2020.12.617`.

[C3] Máté Siket, György Eigner, Levente Kovács, and Imre Rudas. “Analysis of the Effect of Variability on the Blood Glucose Prediction Accuracy”. In: *2021 IEEE 21st International Symposium on Computational Intelligence and Informatics (CINTI)*. ISSN: 2471-9269. 2021, pp. 000181–000186. DOI: `10.1109/CINTI53070.2021.9668397`.

[C4] Máté Siket, Rebeka Tóth, Imre Rudas, György Eigner, and Levente Kovács. “Parameter estimation of T1DM models with a particular focus on endogenous glucose production”. In: *2022 IEEE International Conference on Systems, Man, and Cybernetics (SMC)*. ISSN: 2577-1655. 2022, pp. 1891–1896. DOI: `10.1109/SMC53654.2022.9945097`.

[C5] Máté Siket, Kamilla Novák, Levente Kovács, and György Eigner. “Automatically estimated meals in Model Predictive Control-Moving Horizon Estimation control strategy”. In: *2022 13th Asian Control Conference (ASCC)*. ISSN: 2770-8373. May 2022. DOI: `10.23919/ASCC56756.2022.9828202`.

[C6] Máté Siket, Lehel Dénes-Fazakas, Levente Kovács, and György Eigner. “Numba-accelerated parameter estimation for artificial pancreas applications”. In: *2022 IEEE 20th Jubilee International Symposium on Intelligent Systems and Informatics (SISY)*. ISSN: 1949-0488. 2022, pp. 279–284. DOI: `10.1109/SISY56759.2022.10036259`.

Publications not Pertaining to Theses

[N1] Lehel Dénes-Fazakas, Máté Siket, László Szilágyi, György Eigner, and Levente Kovács. “Investigation of reward functions for controlling blood glucose level using reinforcement learning”. In: *IEEE 17th International Symposium on Applied Computational Intelligence and Informatics SACI 2023 : Proceedings*. 2023, pp. 387–392.

[N2] Máté Siket, Tóth Rebeka, László Szász, Kamilla Novák, György Eigner, and Levente Kovács. “An application programming interface for the widely used academic version of the UVA/Padova Type 1 Diabetes Mellitus Metabolic Simulator”. In: *IEEE 21st World Symposium on Applied Machine Intelligence and Informatics SAMI (2023) : Proceedings*. 2023, pp. 287–292. DOI: `10.1109/SAMI58000.2023.10044485`.

[N3] Péter Földesy, Imre Gergely Jánoki, Ádám Nagy, Máté Siket, and Ákos Zarándy. “Temperature measurement with photodiodes: Application to laser diode temperature monitoring”. In: *SENSORS AND ACTUATORS A-PHYSICAL* 337 (2022). ISSN: 0924-4247. DOI: `10.1016/j.sna.2022.113441`. URL: `https://m2.mtmt.hu/api/publication/32736182`.

[N4] Lehel Dénes-Fazakas, Máté Siket, Gábor Kertész, László Szilágyi, Levente Kovács, and György Eigner. “Control of Type 1 Diabetes Mellitus using direct reinforcement learning based controller”. In: *2022 IEEE International Conference on Systems, Man, and Cybernetics (SMC)*. 2022, pp. 1512–1517. DOI: `10.1109/SMC53654.2022.9945084`.

[N5] Erzsébet Nagy, Bence Géza Czakó, Máté Siket, Balázs Gombos, András Füredi, Gergely Szakács, et al. “Tracking parameter changes of an Impulsive Tumor Growth Model”. In: *IEEE 10th Jubilee International Conference on Computational Cybernetics and Cyber-Medical Systems ICCC 2022*. 2022, pp. 179–184. DOI: `10.1109/ICCC202255925.2022.9922736`.

[N6] György Eigner, Máté Siket, Bence Géza Czakó, Dániel András Drexler, Imre Rudas, Ákos Zarándy, et al. “Model Predictive Tumour Volume Control using Nonlinear Optimization”. In: *STUDIES IN SYSTEMS DECISION AND CONTROL* 415 (2022), pp. 235–250. ISSN: 2198-4182. DOI: `10.1007/978-3-031-00978-5_10`.

[N7] Lehel Dénes-Fazakas, Máté Siket, László Szilágyi, Levente Kovács, and György Eigner. “Detection of Physical Activity Using Machine Learning Methods Based on Continuous Blood Glucose Monitoring and Heart Rate Signals”. In: *SENSORS* 2022 (2022). DOI: `10.3390/s22218568`.

[N8] Máté Siket, Kamilla Novák, Hemza Redjimi, József Tar, Levente Kovács, and György Eigner. “Control of Type 1 Diabetes Mellitus using Particle Swarm Optimization driven Receding Horizon Controller”. In: *IFAC PAPERSONLINE* 54 (2021), pp. 293–298. DOI: `10.1016/j.ifacol.2021.10.271`.

[N9] Levente Kovács, György Eigner, Bence Géza Czakó, Máté Siket, Zsuzsanna Almássy, Gyz Kocsis, et al. “Mesterséges hasnyálmirigy A cukorbetegség automatikus kezelése mérnöki megközelítéssel”. In: *DIABETOLOGIA HUNGARICA* 27 (2019), pp. 249–258. ISSN: 1217-372X. DOI: `10.24121/dh.2019.21`.

[N10] József Tar, Bence Varga, Péter Galambos, László Szcs, Máté Siket, Árpád Varga, et al. “Abstraction in teaching ways of control engineering to support the understanding of mathematics behind Industry 4.0 a Hungarian approach”. In: *IFAC PAPERSONLINE* 55 (2022), pp. 230–235. DOI: `10.1016/j.ifacol.2022.09.284`.

[N11] Levente Kovács, György Eigner, Máté Siket, and László Barkai. “Mesterséges hasnyálmirigy: automatizált cukorbeteg-kezelés mérnöki módszerekkel”. In: *DIABETOLOGIA HUNGARICA* 30 (2022), pp. 147–150. ISSN: 1217-372X. DOI: `10.24121/dh.2022.5.15`.

[N12] Levente Kovács, Bence Géza Czakó, Máté Siket, Tamás Ferenci, András Füredi, Balázs Gombos, et al. “Experimental Closed-Loop Control of Breast Cancer in Mice”. In: *COMPLEXITY* 2022 (2022). ISSN: 1076-2787. DOI: `10.1155/2022/9348166`.

[N13] Ákos Zarándy, Péter Földesy, Ádám Nagy, Imre Gergely Jánoki, Dániel Terbe, Máté Siket, et al. “Multi-Level Optimization for Enabling Life Critical Visual Inspections of Infants in Resource Limited Environment”. In: *2020 IEEE International Symposium on Circuits and Systems (ISCAS)*. 2020. DOI: `10.1109/ISCAS45731.2020.9181040`.

[N14] Bence Géza Czakó, Máté Siket, Dániel András Drexler, and Levente Kovács. “Chemotherapy Optimization using Moving Horizon Estimation based Nonlinear Model Predictive Control”. In: *IFAC PAPERSONLINE* 54 (2021), pp. 215–220. DOI: `10.1016/j.ifacol.2021.10.258`.

[N15] Levente Kovács, György Eigner, Bence Géza Czakó, Máté Siket, and József Tar. “An opportunity of using Robust Fixed Point Transformation-based controller design in case of Type 1 Diabetes Mellitus”. In: *2019 First International Conference on Societal Automation (SA)*. 2019, pp. 1–7. DOI: `10.1109/SA47457.2019.8938069`.

[N16] Máté Siket, György Eigner, and Levente Kovács. “Sensitivity and identifiability analysis of a third-order tumor growth model”. In: *2020 IEEE 15th International Conference of System of Systems Engineering (SoSE 2020)*. 2020, pp. 417–421. DOI: `10.1109/SoSE50414.2020.9130530`.

[N17] Ádám Nagy, Péter Földesy, Imre Gergely Jánoki, Dániel Terbe, Máté Siket, Miklós Szabó, et al. “Continuous Camera-Based Premature-Infant Monitoring Algorithms for NICU”. In: *APPLIED SCIENCES-BASEL* 11 (2021), pp. 7215–7239. DOI: `10.3390/app11167215`.

[N18] Máté Siket, György Eigner, Dániel András Drexler, Imre Rudas, and Levente Kovács. “State and Parameter Estimation of a Mathematical Carcinoma Model under Chemotherapeutic Treatment”. In: *APPLIED SCIENCES-BASEL* 10 (2020). DOI: `10.3390/app10249046`.

[N19] György Eigner, Dénes-Fazekas L., László Szilágyi, Máté Siket, and Levente Kovács. “Physical Activity Detection Using Machine Intelligence. ATTD 2021 Invited Speaker Abstracts”. In: *DIABETES TECHNOLOGY AND THERAPEUTICS* 23 (2021), A-102-A–102. ISSN: 1520-9156. DOI: `10.1089/dia.2021.2525.abstracts`.